Dynamical Spectroscopy of Transient He_2 Molecules

Michiel van Rijnbach

van Rijnbach, Michiel

Dynamical Spectroscopy of Transient He_2 Molecules
M. van Rijnbach - Utrecht
Universiteit Utrecht
Faculteit Natuur- en Sterrenkunde
Thesis Universiteit Utrecht - With a summary in Dutch
ISBN 90-9017720-5
Subject heading: atomic physics / laser cooling / photoassociation
Druk: PrintPartners Ipskamp, Amsterdam

Dynamical Spectroscopy of Transient He_2 Molecules

Dynamische Spectroscopie van Vergangelijke He_2 Molekulen

(met een samenvatting in het Nederlands)

PROEFSCHRIFT

TER VERKRIJGING VAN DE GRAAD VAN DOCTOR
AAN DE UNIVERSITEIT UTRECHT OP GEZAG VAN
DE RECTOR MAGNIFICUS, PROF. DR. W.H. GISPEN,
INGEVOLGE HET BESLUIT VAN HET COLLEGE VOOR PROMOTIES
IN HET OPENBAAR TE VERDEDIGEN
OP MAANDAG 19 JANUARI 2004
DES MIDDAGS TE 12.45 UUR

door

Michiel van Rijnbach

geboren op 5 augustus 1973, te Veenendaal

Promotor: Prof. Dr. P. van der Straten

Faculteit Natuur- en Sterrenkunde
Universiteit Utrecht

This work has been performed as part of the research program of the ‘Stichting voor Fundamenteel Onderzoek der Materie’ (FOM) and with the financial support from the ‘Nederlandse Organisatie voor Wetenschappelijk Onderzoek’ (NWO).

Contents

Chapter 1

Introduction

1.1 General introduction

In photoassociation spectroscopy (PAS) free-bound transitions are made from a ground state molecular potential to a ro-vibronic state in an excited state molecular potential by absorption of a photon. The first known photoassociation measurements were done by Scheingraber *et al.* [1] in a magnesium vapor. The main difficulty in studying free-bound transitions at room temperature is the thermal broadening of spectroscopic lines. In order to resolve the ro-vibronic states separately the width of the velocity distribution must be reduced. Due to the introduction of laser cooling and trapping techniques in the late 70s [2] a new temperature regime became accessible for atomic and molecular physics. Since photons carry momentum, absorption and emission of resonant laser light can change atomic velocities. Atoms can be slowed down and also cooled by laser light. Slowing atoms means that their mean velocity is decreased while cooling means that the velocity width is reduced. Raab *et al.* [3] combined laser light with magnetic fields to cool and trap atoms. This so-called magneto-optical trap (MOT) is a widely used apparatus to study cold collisions. Thorsheim *et al.* [4] developed the theory to explain PAS spectra for low temperatures (< 10 mK). Soon the first photoassociation experiments for sodium were performed in a MOT [5] at even lower temperatures (< 1 mK).

In ultra-cold collisions the ground state wave function is slowly oscillating at large internuclear distances. The overlap between the ground state wave function and an excited bound state wave function is largest at the outer turning point of the bound state. Therefore, the excitation by a photon is most likely to occur at this internuclear distance. The resolution with which the molecules can be excited

to bound states is mainly determined by the temperature of the sample. In this way the excited state potentials can be determined with very high precision. The radiative lifetime of the excited state can be extracted from the data of the excited state potential [6, 7]. Since the s wave scattering length corresponds to a node in the ground state wave function and the height of photoassociation resonances is proportional to the overlap between the ground and excited state wave functions, the scattering length can be estimated from intensity profiles of photoassociation resonances [8].

1.2 This thesis

An advantage of studying photoassociation in alkali metals is that a compound of two atoms only contains two valence electrons. The main disadvantage is that the alkali nuclei have nuclear spin and the hyperfine structure makes the potential curve 'landscape' very complex. In this thesis the rare gas element helium is studied using photoassociation spectroscopy. We use the isotope ^{4}He, which has no nuclear spin and therefore has no hyperfine structure.

The rare gas elements all have metastable states with very high internal energies. Because of this high internal energy rare gas metastable atoms can ionize almost all atoms and molecules in close collisions through *Penning ionization*(PI). For helium this metastable state is He(2^3S), which we will call the He* state throughout the rest of this thesis. It is very long-lived (> 8000 s) and has an internal energy of 19.82 eV. The ground state atoms are excited to this state by electron impact. The PI reactions including associative ionization (AI) between two He* atoms are

$$\mathrm{He}(2^3\mathrm{S}) + \mathrm{He}(2^3\mathrm{S}) \longrightarrow \begin{cases} \mathrm{He}^+ + \mathrm{He}(1^1\mathrm{S}) + e^- & \text{(PI)} \\ \mathrm{He}_2^+ + e^- & \text{(AI)} \end{cases}$$

PI occurs with a very high probability (more than 80 $\%$) except when the two spins of the He* atoms are aligned. In this case PI is strongly reduced due to spin conservation rules [9]. This property has enabled two experimental groups to reach Bose-Einstein condensation in ^{4}He [10, 11], because the He* atoms in the magnetic trap could be evaporatively cooled before loosing them through PI. Helium is usually laser cooled on the $2^3\mathrm{S}_1 \rightarrow 2^3\mathrm{P}_2$ transition. The excited state He(2^3P) has a relatively long lifetime of 98 ns. The level scheme for helium is shown in figure 1.1. In a MOT atom pairs can be excited to the He($2^3\mathrm{S}_1$)+He($2^3\mathrm{P}_{0,1,2}$) molecular potentials by scanning a separate probe laser around these transitions.

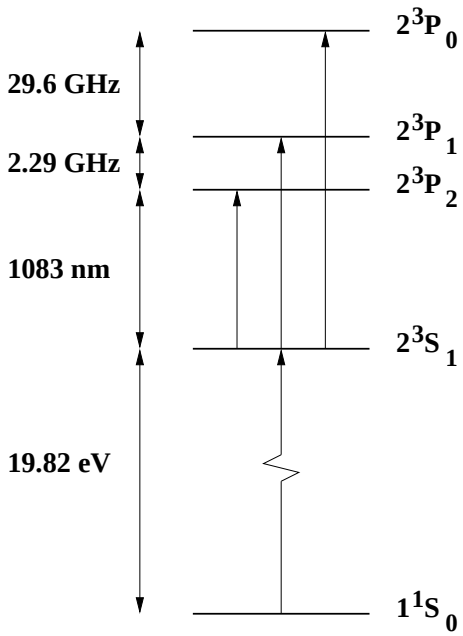

Figure 1.1 The level scheme of helium. In the source the helium atoms are excited to the metastable He(2^3S) state. For laser cooling the $2^3S_1 \rightarrow 2^3P_2$ transition is used and with photoassociation the three transitions He(2^3S_1)+He($2^3P_{0,1,2}$) are probed.

In chapter 2 an atomic beam brightening device, called the collimator, is described. The basic concepts of laser cooling and trapping will be outlined shortly. The collimator has been tested in a another setup than the one used for the photoassociation experiments discussed in chapters 5 and 6. The collimator consists of two pairs of laser beams, which are reflected multiple times between two sets of plane mirrors in order to reduce the transverse velocities of an atomic beam. The atomic beam is created in a DC discharge source at liquid nitrogen temperatures. The mean velocity of the atoms in the atomic beam is about 1000 m/s, which gives a short interaction time for a fixed length of the collimator. For an improved performance of the collimator curved wave fronts are used, which will be explained later. The increase in the He* flux and the velocity dependence will be studied.

In chapter 3 the setup used for photoassociation measurements is described.

The atomic beam is produced in a DC discharge at liquid helium temperatures. The low temperature in the source reduces the mean velocity of the atoms to about 300 m/s. The atoms are slowed down to trapping velocities by a counter-propagating laser beam and subsequently trapped in a MOT. The magnetic field, which is required to compensate the changing Doppler shift in the slowing process, is provided by the MOT coils. The temperature and number of atoms in the MOT are determined by time-of-flight (TOF) measurements and imaging of the MOT cloud. Finally, the laser setup used to study photoassociation in the MOT is described.

A theoretical description of the potentials and the symmetries of the wave functions for the He(2^3S)-He(2^3S) and the He(2^3S) - He(2^3P) systems is given in chapter 4. We describe the wave functions in the Hund's cases (a) and (c) depending on whether the electrostatic interaction or the fine structure interaction is the strongest interaction, respectively. The interaction potentials are calculated including the electrostatic interaction, the fine structure interaction and the rotational energy. Furthermore, the selection rules for molecular dipole transitions are outlined.

In chapter 5 the photoassociation experiments around the 2^3S_1-2^3P_2 asymptote are discussed. The positions of the PAS resonances are calibrated and compared to positions determined from the trap loss measurements at ENS in Paris. Several vibrational series are assigned to potentials using the accumulated phase method [46]. The widths of the resonances are determined and several broadening mechanisms are discussed.

Finally, in chapter 6 PAS is studied at the two other asymptotes, the 2^3S_1-2^3P_1 and the 2^3S_1-2^3P_0 asymptotes. At the former asymptote PAS resonances can be distinguished and the same analysis as in chapter 5 is performed. At the latter asymptote two effects are observed near the atomic resonance and a qualitative discussion is presented.

Chapter 2

The He* collimator

2.1 Introduction

This chapter deals with the collimator used to transversely cool the He* atomic beam. The techniques of laser cooling have made it possible to create slow, cold and parallel atomic beams of high intensity and brightness. Slow means that the mean atomic velocity is low and cold means that the width of the atomic velocity distribution in the longitudinal direction is small. Atomic beams are usually divergent and this is mostly undesired. By cooling the transverse velocity components a divergent beam can be converted into a parallel one. This increases the atomic beam intensity, which is highly desirable for e.g. loading of a magneto-optical trap (MOT) or collision experiments. For thermal atomic helium beams the average velocity of the atoms is usually in the order of 2000 m/s [12, 13]. This means that the interaction time of a laser beam directed perpendicular to the atomic beam with the atoms in the beam is relatively short. During the interaction the transverse velocity components are decreased and therefore atoms will shift out of resonance with this laser beam. This means that simply expanding the laser beam for a longer interaction time will not be sufficient. This problem can be circumvented by using curved wave fronts. In curved wave fronts the changing Doppler shift caused by the changing atomic velocities is compensated by changing the direction of the wave vector of the laser light along the interaction path. This can be achieved by lenses or plane mirrors under small angles (in the order of a few mrads). We adopt the system introduced by Hoogerland [17] and also described in ref. [2].

The organization of this chapter is as follows. In section 2.2 the necessary theory of laser cooling and trapping is discussed. The liquid nitrogen cooled He*

source is described in section 2.3 and the collimator is discussed in section 2.4. Finally, the results achieved with the collimator are outlined in section 2.5.

2.2 Laser cooling

Although laser cooling and trapping is discussed extensively in the literature [2], it is convenient here to define and outline the most important features. Some formulas that are used in the rest of this thesis will be derived in a straightforward way.

Since photons carry momentum, absorption or emission of photons can change the momentum of an atom. This idea existed for a long time, but it was not until the late 70s, that various groups started experimenting with light pressure on atoms. The first theoretical model for interaction of light with atoms dealt with two-level atoms in a monochromatic light field. There are a variety of optical forces that play a role in the description of multilevel atoms in polarization gradients and magnetic fields [14, 15] or polychromatic light fields [19]. In this thesis the description of a two-level atom in a monochromatic light field will be sufficient.

A two-level atom has a single ground and excited state. Photons with the right frequency can excite these atoms from the ground to the excited state and the atoms will decay to the ground state by spontaneous emission if we consider low intensity light fields. An absorption of a photon with wave vector $\mathbf{k}$ transfers a momentum of $\hbar\mathbf{k}$ to the atom. Spontaneously emitted photons are emitted in random directions, so the momentum transfers average out to zero after many spontaneous emissions. Therefore, only the momentum of the atom in the direction of the wave vector of the absorbed light has changed after many absorption-spontaneous emission cycles. In this case the force, which is called the radiation force or the scattering force, can easily be calculated. If Γ is the spontaneous decay rate of the excited state and ρ_{ee} is the probability for the atom to be in the excited state, the radiation force is given by [2]

$$\mathbf{F}_{rad} = \hbar\mathbf{k}\Gamma\rho_{ee} \,, \tag{2.1}$$

where

$$\rho_{ee} = \frac{s_0/2}{1 + s_0 + 4(\delta/\Gamma)^2} \,, \tag{2.2}$$

with s_0 the on-resonance saturation parameter and δ the detuning from atomic

resonance. On resonance the force is maximum and if $s_0 \gg 1$ equal to

$$\mathbf{F}_{max} = \frac{\hbar \mathbf{k} \Gamma}{2} \, . \tag{2.3}$$

In the case the atom is moving, the resonance frequency is shifted by the Doppler effect. If an atom is moving in two counter-propagating laser beams, which have a negative detuning from atomic resonance, it will shift more into resonance with the laser beam opposing its velocity. In this so called *optical molasses* the velocity of the atom will be damped. The Doppler shift $\delta = -\mathbf{k} \cdot \mathbf{v}$ is opposite for the two beams and the radiation force for each beam is given by

$$\mathbf{F}_{\pm} = \pm \frac{\hbar \mathbf{k} \Gamma}{2} \frac{s_0}{1 + 2s_0 + 4(\delta_l \mp kv)^2/\Gamma^2} \, . \tag{2.4}$$

In this equation δ_l is the laser detuning from atomic resonance and v is the atomic velocity. The factor 2 in front of s_0 in the denominator accounts for the saturation of the two laser beams. The radiation force $\mathbf{F}_{mol}$ in the optical molasses is the sum of these two forces and is given by

$$\mathbf{F}_{mol} = \mathbf{F}_{+} + \mathbf{F}_{-} \approx -\beta \mathbf{v} \, , \tag{2.5}$$

with

$$\beta = -\frac{8\hbar k^2 s_0 (\delta_l/\Gamma)}{(1 + 2s_0 + 4(\delta_l/\Gamma)^2)^2} \, . \tag{2.6}$$

It is clear that the atomic velocity will be damped for a negative laser detuning, which means that the laser frequency is smaller than the atomic transition frequency.

In atomic beam slowing a resonant laser beam counter-propagates an atomic beam. However, as the atoms slow down the Doppler shift decreases and the atoms shift out of resonance. To overcome this problem several techniques have been developed, but the most widely used is Zeeman compensated slowing. In this technique the decreasing Doppler shift is compensated by decreasing the atomic resonance frequency with a magnetic field. The Zeeman effect causes the atoms to stay in resonance with the light along the slowing path. It can be shown that in that case the magnetic field $B(z)$ must vary as a square root of the position z,

$$B(z) = B_0 \sqrt{1 - z/z_0} \, , \tag{2.7}$$

where $B_0 = \hbar k v_0 / \mu_B$ with v_0 the start velocity of the atom at the entrance of the Zeeman slower and μ_B is the Bohr magneton. Furthermore, the length of

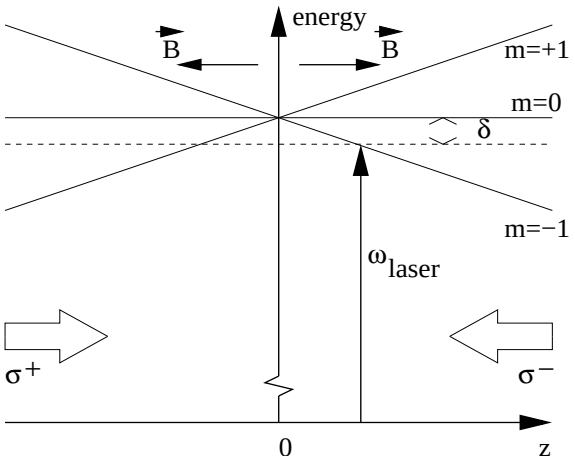

Figure 2.1 Trapping scheme in one dimension. The two laser beams are circularly polarized with opposite helicities with respect to the z axis. In this way atoms to the right of $z = 0$ are more resonant with the laser beam coming from the right and the opposite is true for atoms to the left of $z = 0$. The direction of the magnetic fi eld is indicated.

the magnet is $z_0 = Mv_0^2/F_{const}$ where M is the atomic mass and F_{const} is the constant force exerted on the atoms, which has to be smaller than or equal to the maximum force of equation 2.3.

The last subject of this section is the magneto-optical trap (MOT). A one dimensional model will be discussed and it is assumed, that the atomic transition is from a $J = 0$ ground state to a $J = 1$ excited state, where J is the total angular momentum. The situation is depicted in figure 2.1. The atom is placed in a magnetic field $B(z) = \alpha z$ with α a positive constant. For $z > 0$ the $M_J = -1$ magnetic sublevel is shifted into resonance with the laser beam, that points towards $z = 0$, due to the Zeeman effect. The helicity of the light must be σ^- in order to drive the atom to the center of the trap. For $z < 0$ the helicity of the laser beam that will push the atom towards $z = 0$ (figure 2.1) must be σ^+ because this laser beam is now more resonant with the $M_J = +1$ magnetic sublevel. In this way the atoms will be confined both in velocity (optical molasses) and in position. Because of the Zeeman shift the radiation force also becomes position-dependent

and can be approximated as

$$\mathbf{F} \approx -\beta\mathbf{v} - \kappa\mathbf{r} \ , \tag{2.8}$$

with β given by equation 2.6 and the spring constant κ is

$$\kappa = -\frac{8k\mu_B\alpha s_0(\delta_l/\Gamma)}{(1+2s_0+4(\delta_l/\Gamma)^2)^2} \ . \tag{2.9}$$

This model can be generalized to three dimensions. The light field then consists of three mutually perpendicular pairs of counter-propagating laser beams and the inhomogeneous magnetic field is created by two coils in an anti-Helmholtz configuration. The zero point of the magnetic field (right between the two coils) needs to coincide with the region where the six laser beams overlap. The atoms are trapped and cooled in this combination of light and magnetic fields, which is called the magneto-optical trap [3].

2.3 The He* source

The atomic beam line described in this chapter is different from the one used in the remainder of this thesis. The setup in this chapter is not used for the photoassociation experiments, but for atomic beam brightening experiments. The He* source is based on the same principle as the source described in the next chapter, but here the source is cooled with liquid nitrogen instead of liquid helium. The source is developed according to the idea of ref. [18], where a source for metastable neon is described.

The source is schematically shown in figure 2.2. A high voltage (-580 Volts) is kept between a tungsten needle inside a glass tube and a grounded aluminum nozzle plate. The discharge current is 3 mA. The needle is kept in the center of the glass tube by use of ceramic spacers. The ceramic spacers also introduce pump resistance in order to create the appropriate pressure at the front of the glass tube. Helium gas in the ground state ($^1S_0$) flows from outside the glass tube, where it has good thermal contact with a reservoir filled with liquid nitrogen (77 K), into the glass tube through a hole at the tip of it. At the back end of the glass tube the gas is pumped away by a foreline pump. The discharge runs between the needle through the aluminum nozzle (Ø 0.5 mm) to a skimmer (Ø 0.5 mm). The nozzle and the skimmer define the atomic beam and reduce the gas load in the rest of the setup. The pressure in the source chamber, where the discharge runs, is about 1 mbar. The pressure in the chamber between the nozzle and the skimmer

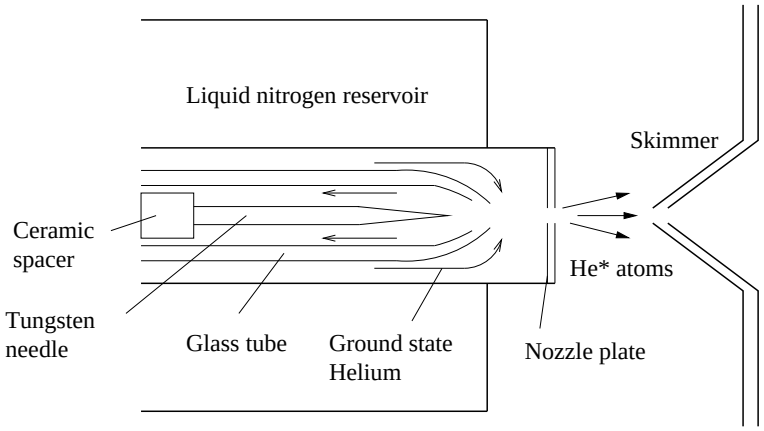

Figure 2.2 The liquid nitrogen cooled He* source. The He* atoms are created in the discharge running between a tungsten needle and a grounded nozzle plate and effuse through the nozzle and the skimmer. The tungsten needle is kept on a voltage of -580 Volts and the discharge current is 3 mA.

is $2 \cdot 10^{-6}$ mbar. After the skimmer the atoms enter the collimator chamber where they are transversely cooled by laser beams. The vacuum in the chamber between the nozzle and the skimmer and in the collimator chamber is sustained by turbo molecular pumps backed by foreline pumps.

In the DC discharge helium atoms are excited to the 2^3S and the 2^1S states by electron impact. The fraction of He(2^3S) can be measured by deflection of the He(2^3S) atoms out of the atomic beam with a laser beam resonant with the $2^3\text{S} \rightarrow 2^3\text{P}$ transition. A channeltron with a 5 mm by 40 μm vertical slit in front of it is used as a detector. The channeltron is positioned 4.2 m behind the collimator and it can only detect He(2^3S) atoms, He(2^1S) atoms and UV photons in the atomic beam. The ground state atoms in the atomic beam do not have internal energy and can not be detected by the channeltron. The He(2^3S) fraction of the detected flux varies between 40% and 50%. We did not distinguish between the He(2^1S) and UV photons in the atomic beam, but this can be done with a time-of-flight (TOF) technique using a mechanical chopper, which is placed in the atomic beam to separate in time the atomic velocity distribution and the photon peak.

We determined the velocity distribution of the He* atoms by deflection with a

laser beam. The channeltron detector is placed in the center of the atomic beam. A laser beam, which is directed perpendicularly to the atomic beam and resonant with the 2^3S$\rightarrow 2^3$P transition, deflects the He(2^3S) atoms out of the atomic beam. The laser beam is chopped at a frequency of 100 Hz with a duty cycle of 5 %. The deflected atoms appear as a dip in the channeltron signal in this TOF measurement. The best fit to the TOF data is a supersonic distribution given in ref. [20]. The supersonic velocity distribution can be converted to a time distribution and is given by

$$f(t)dt = \frac{c}{t^4} e^{-(\frac{L/t-\bar{v}}{w})^2} dt \, , \tag{2.10}$$

with c a constant and L=2.15 m the distance between the position where the atoms are deflected and the channeltron detector. The fit parameters are $\bar{v}$ for the mean atomic velocity and w, the width of the distribution. The fit yields $\bar{v} = 975$ m/s and $w = 420$ m/s. The mean velocity corresponds to a temperature of 180 K, which is considerably higher than 77 K, which is the temperature of liquid nitrogen. This can be due to heating in the discharge and insufficient thermal contact with the liquid nitrogen reservoir. The TOF measurement has been inverted in order to be able to fit the distribution of equation 2.10. The data and the fit are shown in figure 2.3. The He* flux is 10^{14} sr^{-1} s^{-1}.

2.4 The collimator

The collimator, which is used to transversely cool the atomic beam is part of a long atomic beam brightening setup. Since all components of the setup were not in use simultaneously, they will briefly be mentioned. The setup is shown in figure 2.4. After the collimator chamber the atomic beam enters the Zeeman magnet, which consists of two solenoids with a zero field point in between them. In order to maintain a low pressure in the whole setup a turbo molecular pump is connected to the stainless steel cross piece between the solenoids. The turbo molecular pump is backed by a foreline pump. The atoms pass through a magneto-optical compressor (MOC), which transversely cools and compresses them by means of a quadrupole magnetic field and two pairs of counter-propagating laser beams perpendicular to the atomic beam. After the MOC a mirror with a 1 mm hole is installed in the vacuum. With this mirror the slowing laser beam can be aligned to counter-propagate the atomic beam. The MOC can compress the atomic beam and direct it through the hole where the atoms can be detected by the channeltron mentioned in the previous section.

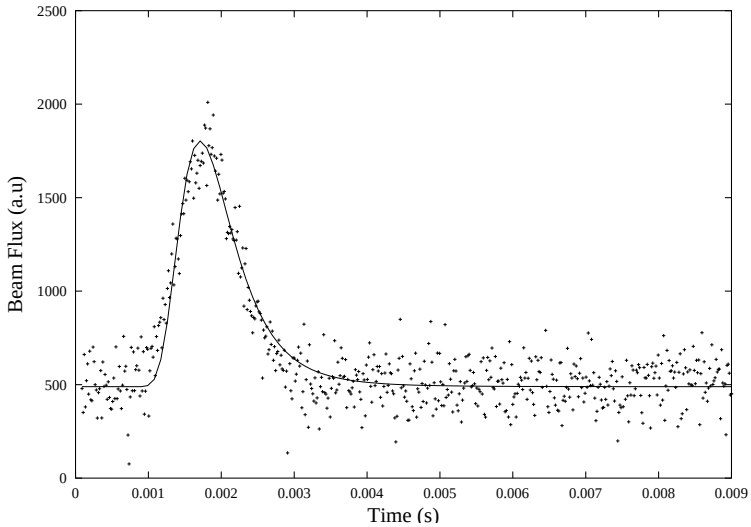

Figure 2.3 Time-of-flight measurement of the He* beam. The solid line is the fit of a supersonic time distribution to the data.

2.4.1 Construction

The collimator consists of four plane mirrors positioned as shown in figure 2.5. The mirrors are each 20 cm long and 3.8 cm wide. The separation between two mirrors opposite to each other is 6 cm. Laser light can be coupled into the collimator at either side of the collimator. In each pair the mirrors have a small angle γ between them as indicated in the two dimensional picture in figure 2.6. After each reflection the angle between the wave vector of a laser beam and the y axis (see figure 2.6) changes with an amount γ. This provides the desired curved wave fronts. If the angle γ is chosen carefully, the Doppler shift the atoms experience does not change throughout the collimator, because both the transverse velocity of the atoms and the direction of the wave vector change. The angle γ for which this occurs is estimated in section 2.4.3. The angle is realized by putting thin aluminum foils on one side of each mirror.

The mirrors also have a small angle ϵ with each other in the x direction (perpendicular to the paper in figure 2.6) but this is undesirable, because the position of the reflections on the mirrors will change in the x direction after each reflection

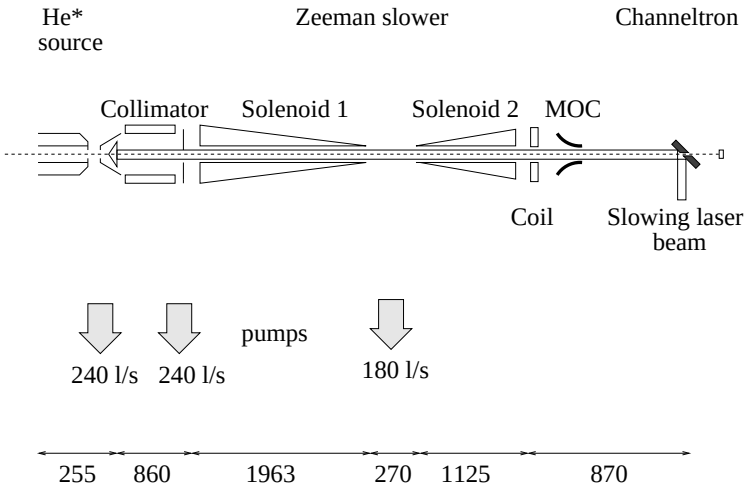

Figure 2.4 The setup in which the collimator is used. From left to right is the He* source, the collimator, the Zeeman slower, the magneto-optical compressor and the mirror with a hole in it to direct the slowing laser beam into the Zeeman magnet.

and the overlap of the laser light with the atomic beam decreases eventually. This angle should be made as small as possible. Each mirror is fixed at four points in a stainless steel frame and the frame itself is adjustable by two knobs outside the vacuum chamber. In this way the axis of the collimator can be aligned with the center of the atomic beam in order not to change the direction of the atomic beam.

2.4.2 Laser light

The laser light is provided by a diode laser (Spectra Diode Lab, SDL-6702-H1) fed by a home-built supply. By changing the current through the diode or the temperature of the diode the frequency of the light can be tuned. The atomic transition on which the atoms are cooled is the $2^3S_1 \rightarrow 2^3P_2$ transition at a wavelength of 1083 nm. The laser light in the collimator must be locked approximately 120 MHz below resonance. It proved difficult to lock the laser at this large detuning using saturated absorption spectroscopy. Therefore, another technique to lock the collimator laser is applied. We beat the collimator laser light with light from a second, identical laser diode, which is locked on resonance by using saturated ab-

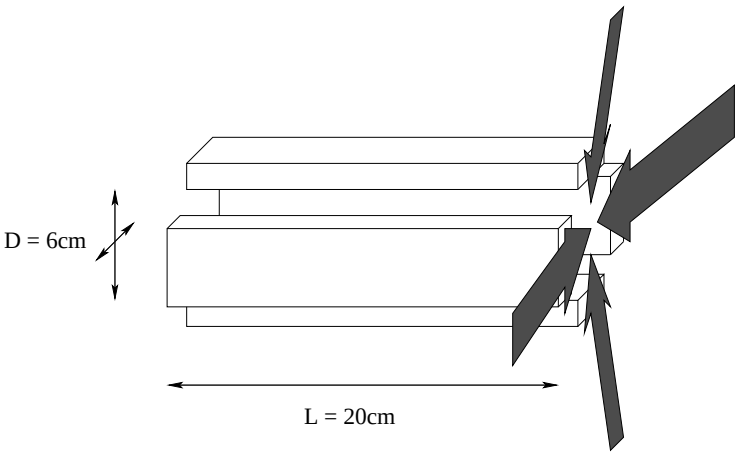

Figure 2.5 The configuration of the mirrors in the collimator. The laser beams are coupled in at the side furthest away from the atom source.

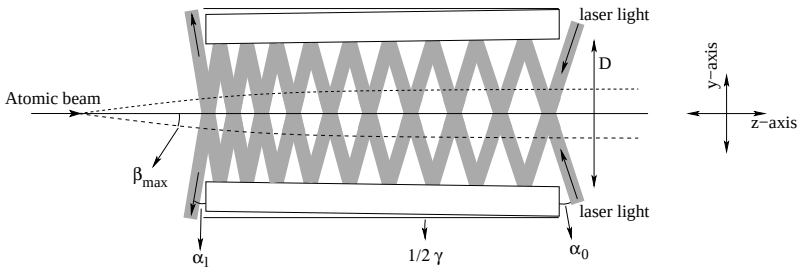

Figure 2.6 Two dimensional cross section of the collimator. The atoms are traveling in the positive z-direction. Each mirror has an angle $\gamma/2$ with the z axis.

sorption spectroscopy. This laser is used for deflection of He* atoms out of the atomic beam for TOF measurements. Both lasers can provide 40 mW power and the linewidths are both 3 MHz. The laser beam profiles are rectangular with an approximately 5 mm width and a 10 mm height. The light is linearly polarized.

The locking is performed as follows. A glass plate splits off a few percent of

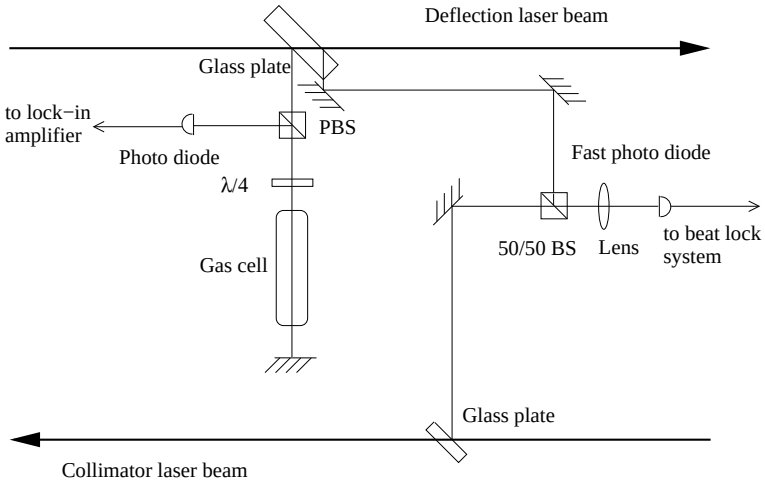

Figure 2.7 Laser stabilization setup for both the collimator laser and the deflection laser. On the left the saturated absorption setup and on the right the beat lock system are shown. In the figure PBS stands for polarizing beam splitter, BS for beam splitter, $\lambda/4$ for a $\lambda/4$ retardation plate.

the direct collimator beam. This light is focused onto a fast photo diode (Hamamatsu G3476-01) together with a few percent of the deflection laser beam. A home-built unit divides the frequency of the beat signal from the photo diode by a factor of 2048 and this signal is sent into a phase sensitive detector together with a reference signal of a fixed frequency from a waveform generator. If the frequency of the beat signal and the frequency of the reference signal are different, the phase detector feeds a voltage, which is proportional to the phase difference between the beat signal and the reference signal, to the power supply of the collimator laser to adjust the frequency. In this way a phase-locked loop (PLL) is created and the collimator frequency can be locked on a detuning ranging from 50 MHz to about 1 GHz below resonance with an accuracy of a few MHz. The time constant of the PLL is 1 second.

For the saturated absorption spectroscopy setup 2% of the direct deflection laser beam is split off and directed through a glass cell which contains helium gas at a pressure of a fraction of a mbar. In this glass cell He* atoms are created in a RF discharge at an RF frequency of 23 MHz. The laser beam is retro-reflected

and directed onto a photo diode. The laser frequency is modulated around the $2^3S_1 \rightarrow 2^3P_2$ resonance at a 1 kHz rate with an amplitude of a few MHz and the Doppler-free Lamb dip in the absorption signal is used to lock the laser frequency. The photo diode signal is fed to a lock-in amplifier together with a reference signal of the same frequency. The output of the lock-in amplifier is integrated over 100 ms with an integrator and is fed to the modulation input of the laser power supply in order to keep the laser frequency on atomic resonance. In figure 2.7 the setup for locking both lasers is shown.

The collimator laser beam is split into four laser beams by three 50/50 beam splitters. These four beams are directed into the collimator as is schematically shown in figure 2.5. It is necessary that both beams of one pair of laser beams have the same intensity, otherwise the atoms will experience a net force in one direction and will be deflected instead of being collimated. In the xz plane the laser beams have a saturation parameter s_0 of 125 and in the yz plane a s_0 of 150. The laser beams are 5 mm wide and 10 mm high and this limits the angle α_0 (indicated in figure 2.6). The coating on the mirrors did not reach the end of the mirrors, so that the minimal angle α_0, that could be achieved, is 0.133 rad. If $n(z)$ is the number of reflections a laser beam has made when arriving at the position z in the collimator, then the angle $\alpha(z)$ between this laser beam and the y axis (or x axis) at that position is given by

$$\alpha(z) = \alpha_0 - n(z)\gamma \; . \tag{2.11}$$

The number of reflections is higher when light is coupled in at the back of the collimator (as shown in figure 2.6) than in the case light is coupled in at the front. From figure 2.6 it can be seen, that the distance z traveled in the collimator can be expressed as

$$z = D\tan(\alpha_0) + D\tan(\alpha_0 - \gamma) + ... + D\tan(\alpha_0 - n(z)\gamma) \; , \tag{2.12}$$

where D is the distance between two mirrors. If α_0 is a small angle and $\gamma \ll \alpha_0$, the sum in equation 2.12 gives

$$n(z) = \frac{\alpha_0}{\gamma} - \frac{1}{\gamma}\sqrt{\alpha_0^2 - 2\gamma\frac{z}{D}} \; . \tag{2.13}$$

Substitution of equation 2.13 into equation 2.11 gives

$$\alpha(z) = \sqrt{\alpha_0^2 - 2\gamma\frac{z}{D}} \; . \tag{2.14}$$

This indicates, that there is a minimum angle $\alpha_0 = \sqrt{2\gamma z/D}$ below which the laser beam will leave the collimator at the same end it was coupled in. This means that the value $\alpha_0 = 0.133$ dictated by the geometry of the collimator and the dimensions of the laser beam must be larger than this value.

2.4.3 Atom trajectories

If the light force on an atom (equation 2.1) is to be constant through the collimator, the Doppler shift $\delta_D = -\mathbf{k} \cdot \mathbf{v}$ experienced by the atoms needs to be constant. Since the transverse atom velocity $v_\perp$ decreases through the collimator, the direction of the wave vector $\mathbf{k}$ of the light must change in such a way that this condition is met. This requires the curved wave front. In a perfect collimator all atoms are traveling parallel to the axis of the collimator at the end of the collimator. There is a maximum angle $\beta_{\max}$ between the atom's velocity and the axis of the collimator for which the light is resonant with the atom throughout the collimator. This angle, which is indicated in figure 2.6, must be equal to the angle difference $\alpha(0) - \alpha(L)$ of the wave vector $\mathbf{k}$ between the entrance and the exit of the collimator. The equality gives

$$\beta_{\max} = \alpha_0 - \sqrt{\alpha_0^2 - 2\gamma \frac{L}{D}} \,, \tag{2.15}$$

and using equation 2.13 we get

$$\beta_{\max} = N_{\text{total}} \gamma \,. \tag{2.16}$$

The capture angle $\beta_{\max}$ can be estimated by assuming that the initial transverse velocity component $v_\perp = v \sin \beta_{\max}$ is damped to zero in the time t the atom spends in the collimator. This gives

$$v_\perp = \frac{F}{M} t \,, \tag{2.17}$$

where F is the light force exerted on the atom and M is the mass of the atom.

There are positions in the collimator where no light is present, because of the limited dimensions of the laser beam. At these positions the atoms experience no radiation force and we assume that the average force F exerted on the atom is half of the maximum radiation pressure $F_{\max} = \hbar k \Gamma / 2$. This gives using $t = L/(v \cos \beta_{\max})$:

$$\beta_{\max} = \frac{1}{2} \sin^{-1} \frac{\hbar k \Gamma L}{2 M v^2} \,. \tag{2.18}$$

horizontal		vertical	
γ	ϵ	γ	ϵ
1.39 mrad	39 μrad	1.38 mrad	13 μrad

Table **2.1** In this table the angles γ and ϵ for both the horizontal and the vertical direction in the collimator are shown.

Substitution of the appropriate values gives $\beta_{\max} = 0.055$ rad and, using equation 2.15, the angle γ is found to be 1.74 mrad. Finally, equation 2.16 gives the total number of reflections: $N_{\text{total}} = 31$. The same procedure outlined above can be used to calculate the total number of reflections in the case the laser light is coupled in at the front of the collimator. Then the laser beam just reflects 20 times. Obviously, this way the collimator is less efficient.

2.5 Results

In this section experiments with the collimator are discussed. In table 2.1 the angles between both pairs of mirrors are shown. As mentioned before the angle ϵ should be made as small as possible. In figure 2.6 this is the angle between the mirrors and the xz-plane where the x direction is perpendicular to the paper (for the other mirror pair it is the yz-plane). Due to this angle the position of the reflections on the mirrors will not stay in the center of the mirrors. This diminishes the overlap between the atomic beam and the laser beams and should be avoided. It should also be noted that both the angle γ for the horizontal direction and the vertical direction are smaller than the value estimated in the previous section. Since it is very difficult to adjust the angles and the angle γ has to be equal or smaller than the value estimated in the previous section, we used the collimator with the angles as stated in table 2.1.

As a first experiment the He* flux is optimized on the channeltron detector. The axis of the collimator must coincide with the atomic beam axis for optimal performance. The operation of the collimator should be optimal at the same laser detuning in two dimensions. The optimal laser detuning is found to be -113 MHz from the $2^3S_1 \rightarrow 2^3P_2$ resonance. The distance between the end of the collimator and the detector is about 4.2 m. The maximum flux gain is found to be equal to 2. Since the He* fraction of the beam flux is 50 %, this means that the increase of the He* component is a factor of 3. Next, a horizontal scan through the beam profile

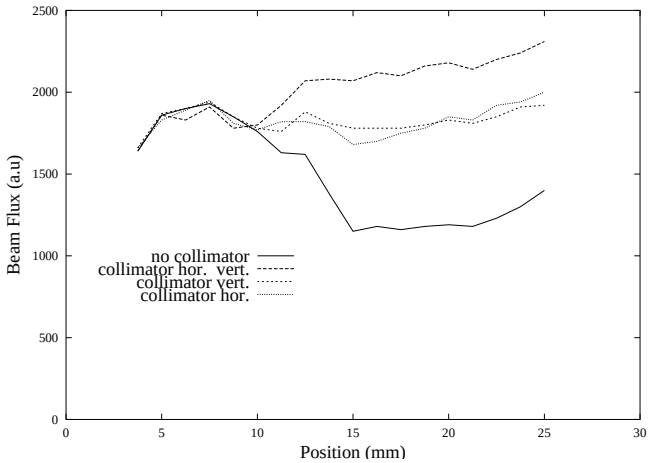

Figure 2.8 Scan through the atomic beam without collimation, collimation in the horizontal dimension, collimation in the vertical dimension and in both dimensions. The center of the atomic beam is at the position of about 15 mm.

is made without collimation, with collimation in either one or the other dimension and collimation in two dimensions. The results are shown in figure 2.8. As can be seen in this figure, there is no signal increase on one side of the atomic beam. There is no clear explanation for this. It is possible that the collimator still deflects the He* atoms out of the atomic beam. However, the position at which the signal increases could not be changed, only the amount of increase by slightly adjusting the position of the collimator. It is also possible, that the He* atoms are blocked on one side by the electrical wires of the magneto-optical compressor. In that case, only reflected photons are detected, since the inside of the Zeeman magnet is highly reflective.

In a second experiment we measure the detuning dependence of the He* signal normalized by the He* signal without collimation, so the signal is equal to 1 at large detunings where no collimation occurs. The photon and He(2^1S) signals are subtracted. The laser frequency can be determined with the beat signal of the deflection laser and the collimator laser. The deflection laser is used to monitor the amount of He* in the atomic beam by deflection of the He* after each measurement. The results are shown in figure 2.9. There is a clear increase around

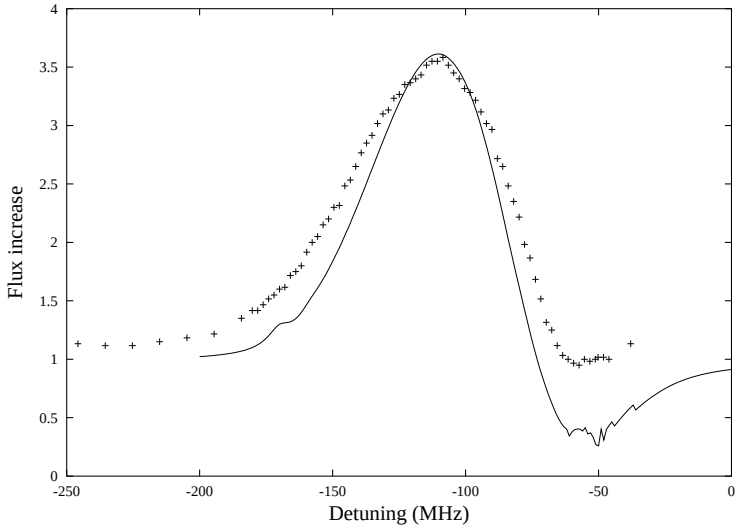

Figure 2.9 Detuning dependence of the He* signal increase by the collimator (points) and a calculation (drawn line).

a laser detuning of -110 MHz. At larger detunings the normalized signal slowly decays to 1 as expected. At small detunings there is a small dip in the signal because for these detunings the laser beam with a wave vector in the same direction as the transverse velocity component of an atom becomes resonant and the atoms are deflected away from the collimator axis. In figure 2.9 also the results of a numerical simulation are shown, which exhibits the same features as the measurements. In particular the laser detuning for optimal collimation agrees very well with the measurements. The measurements are not performed for smaller detunings because the beat lock system is very unstable for detunings smaller than 40 MHz.

Finally, we study the effect of collimation on the velocity distribution of the atomic beam. As mentioned in section 2.3 the uncollimated atomic beam has a mean velocity of 975 m/s and a velocity width of 420 m/s. The time-of-flight (TOF) measurements as described in section 2.3 are repeated with the collimator operating in one or two dimensions at different detunings. In figure 2.10 the TOF spectrum without collimation and with collimation in two dimensions at a

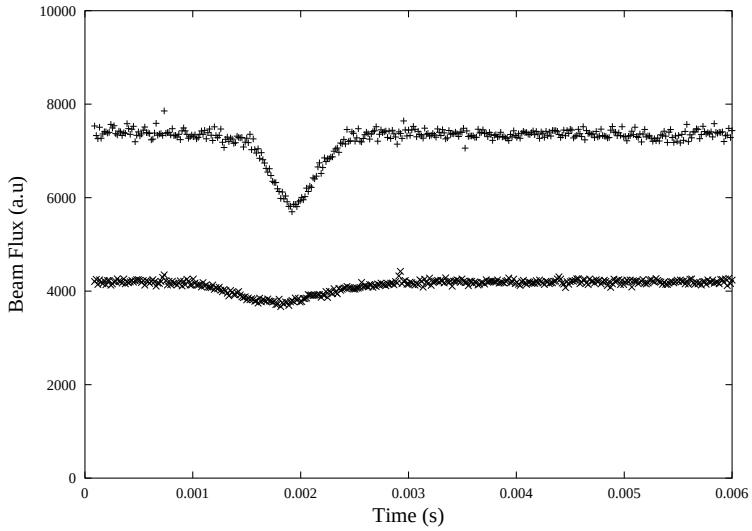

Figure 2.10 The lower curve in this figure is a TOF measurement without collimation and the upper curve for collimation in two dimensions at a laser detuning of -113 MHz.

detuning of -113 MHz are shown. Clearly, the signal is larger with collimation, since a parallel atomic beam gives a higher intensity at the position of the channeltron than a divergent atomic beam. The dip in the signal is also deeper in this case, since the fraction of He* flux that can be deflected out of the atomic beam is larger. It can also be seen that the width of the time distribution becomes smaller with collimation. The measurements are performed for detunings in the range -100 MHz to -150 MHz. The distribution of equation 2.10 is fitted to each TOF spectrum to obtain the mean velocities and velocity widths.

First, the dependence of the mean velocity on the collimator laser detuning is examined. The mean velocities obtained from the fits are shown in figure 2.11 for each detuning with the collimator working in the horizontal direction, vertical direction and both directions. Figure 2.11 shows that the collimator works as a velocity selector. This can be explained as follows. If we assume that the atom trajectories are parallel to the atomic beam axis at the end of the collimator, the resonance condition for the collimator laser at that position is

$$\omega_0 - \omega_l = kv \sin \alpha_0 \ , \tag{2.19}$$

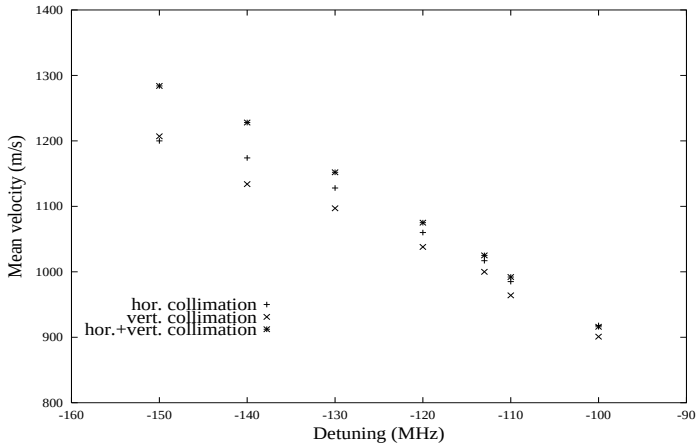

Figure 2.11 Mean velocity of the collimated velocity distributions as a function of the laser detuning for three collimation configurations.

where ω_0 is the atomic resonance frequency and ω_l the laser frequency. Since α_0 is a constant, the collimator laser interacts with faster atoms at a higher detuning. If a linear fit is made to the data in figure 2.11 it can be seen from equation 2.19 that the tangent of the straight line is $(k \sin \alpha_0)^{-1}$. The three fits give $\alpha_0 = 0.155$ rad for collimation in the horizontal direction, $\alpha_0 = 0.165$ rad in the vertical direction and $\alpha_0 = 0.137$ rad for the collimator working in both dimensions. These angles are all somewhat larger than the estimated value of $\alpha_0 = 0.133$ rad. However, the estimated value is a lower limit for the angle α_0.

Next, we study the width of the velocity distribution with collimation as a function of the collimator laser detuning. The velocity widths are found from the fits of the TOF spectra. The results are shown in figure 2.12. Clearly, the width is not constant as a function of the laser detuning. From equation 2.19 it can be seen, that at large detunings the laser light interacts with fast atoms and at small detunings it interacts with slow atoms. This means that the interaction time is longer for small detunings. If the detuning goes to zero the width converges to a certain limit and it can be seen from figure 2.12 that this limit is about 160 m/s. This value corresponds to the velocity class of atoms that is resonant with the

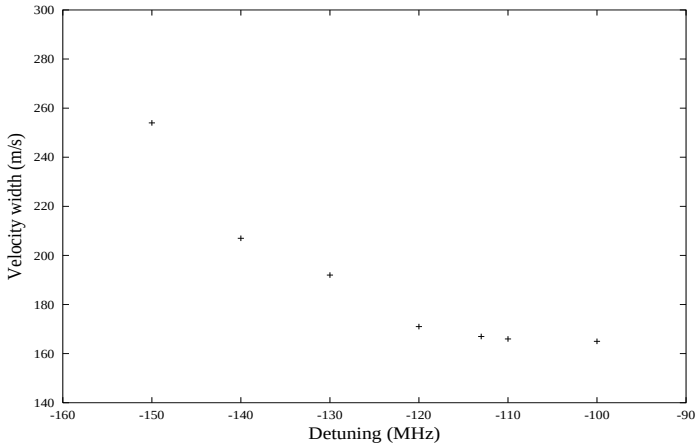

Figure 2.12 Width of the collimated velocity distributions as a function of the laser detuning.

light. Since the linewidth is power broadened, this condition is given by

$$k\Delta v \sin\alpha_0 = \sqrt{1+s_0}\,\Gamma\,, \tag{2.20}$$

with s_0 the on-resonance saturation parameter, Γ the linewidth and Δv the velocity class that is affected by the light. If we average the saturation parameters of the laser beams for both dimensions, we find $\Delta v = 152$ m/s, which agrees very well with the limit of 160 m/s resulting from the measurements.

2.6 Conclusions

We have built a collimator to transversely cool the He* atomic beam. The collimator reduces the divergence of the atomic beam. At a position of 4.2 m from the end of the collimator the He* flux increases by a factor of 3. This increase is small in comparison with the increase of a factor 25 measured with the He* collimator described in ref. [27]. In this reference the collimator laser has much more power, so the laser light stays resonant with more atoms in the collimator due to power broadening. Furthermore, two of the four mirrors in their setup are outside of the vacuum, which means that the mirrors can be adjusted during the measurements to maximize the He* flux.

The detuning dependence of the flux increase is in good agreement with the results of a numerical simulation and shows that the collimator performs optimal at a laser detuning of -113 MHz. We also showed that the collimator works as a velocity selector. Both the mean velocity and the width of the velocity distribution as a function of the laser detuning can be explained with simple calculations.

Chapter 3

The Photoassociation spectroscopy setup

3.1 Introduction

Photoassociation has been studied at room temperature before atoms could be cooled down to milliKelvin and even lower temperatures. The first photoassociation measurements were done by Scheingraber *et al.* [1]. They studied laser induced fluorescence in a magnesium vapor. The advantage of studying photoassociation in a magneto-optical trap (MOT) is the much narrower resonance peaks due to the very small thermal broadening. In this way it is possible to resolve different vibrational levels and even rotational levels in the excited molecular state.

In this chapter the experimental setup for photoassociation measurements is described. The setup is different from other He* MOT setups, since the atom source used is cooled by liquid helium. In this way a much shorter Zeeman slowing section is required and consequently, the setup is also much shorter. An extensive description of the setup used for the experiments is given in [21, 22]. In section 3.2 the He* source is described and in section 3.3 the slowing process is discussed. Section 3.4 deals with the MOT and its characteristics and in section 3.5 the probe laser setup used for the photoassociation measurements is described.

3.2 The liquid helium cooled He* source

The source used to load atoms in the MOT is of the same type as the one described in chapter 2 (figure 2.2). The main difference is that the source described in the present chapter is cooled with liquid helium instead of liquid nitrogen. The discharge in the source runs between a tungsten needle at -700 Volts and a grounded

nozzle plate. The discharge current is 0.05 mA, which means that only 35 mW is dissipated. The pressure at the front of the glass tube is only 10^{-2} mbar. This is in contrast with conventional sources, where the pressure is in the order of several tens of mbars [12, 13]. The pressure behind the nozzle is in the order of 10^{-5} mbar.

Ground state helium atoms He($^1S_0$) flow from outside the glass tube, where they have good thermal contact with the reservoir filled with liquid helium, through a hole at the tip of the glass tube. At the back end of the glass tube the gas is pumped away by a foreline pump. In the discharge He(2^3S) atoms, He(2^1S) atoms and UV photons are created by electron impact. These are the constituents of the beam that are detected by a channeltron detector positioned 60 cm from the source exit. The ground state atoms present in the beam can not be detected. The fraction of photons is about 25 % of the detected signal and can be determined by separating the photons from the metastable atoms in a time-of-flight (TOF) measurement. The amount of He(2^1S) atoms is 5–8% This is measured by deflecting the He(2^3S) atoms out of the atomic beam with light resonant with the $2^3S_1 \rightarrow 2^3P_2$ transition and subtracting the photon contribution. This means that 65–70% of the detected source flux is in the He(2^3S) state. This is about 20 % higher than the He(2^3S) fraction in the atomic beam discussed in the previous chapter.

The He(2^3S) flux is 10^{12}sr^{-1}s^{-1} instead of 10^{14}sr^{-1}s^{-1} for the liquid nitrogen cooled source of the previous chapter. An explanation is the hundred times higher pressure inside the liquid nitrogen cooled source, which causes a higher beam flux. When the pressure in the liquid helium cooled source is increased, the equilibrium temperature of the He gas in the source increases. The high gas load can not efficiently be cooled by the liquid helium. This causes the mean velocity of the atomic beam to be higher and as a result less atoms can be slowed down to the trapping velocity of the MOT. At the operational pressure (10^{-2} mbar) the mean velocity of the atoms is lower, only 300 m/s (see figure 3.1), because the source can be cooled to temperatures of 10–15 K.

3.3 Slowing

As mentioned in the previous section the mean velocity of the metastable atoms is 300 m/s. This is lower than the mean velocity of 975 m/s for the liquid nitrogen cooled source of chapter 2 and much lower than the mean velocity of about 2000 m/s for conventional sources [13]. Therefore, a Zeeman slower to slow the atoms

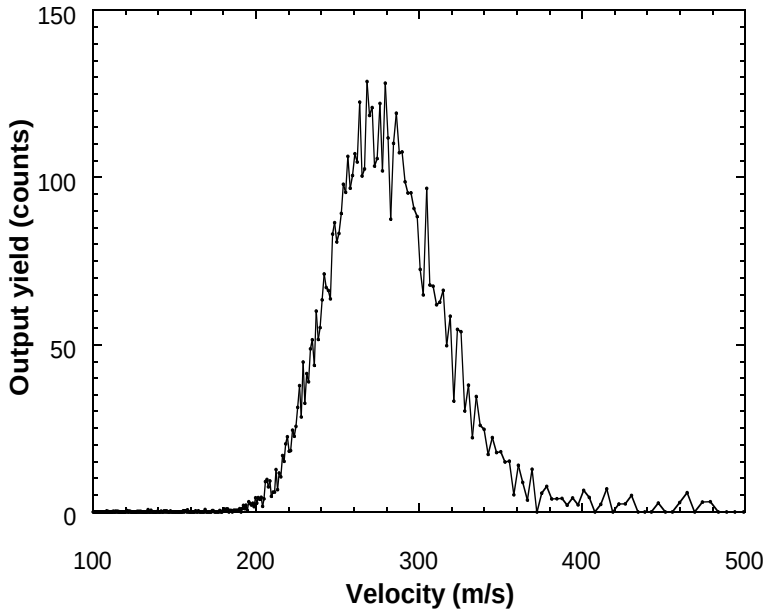

Figure 3.1 The velocity distribution of the source flux (He($2\,^1$S) and He(2^3S) atoms). This distribution is calculated from the time-of-flight spectrum using the photon peak for the calibration of the time zero.

down to the trapping velocity of the MOT can be made much shorter. Since the coils used for our MOT are very large (about 200 mm radius), the metastables can be slowed down in the magnetic field of the MOT. In the plane exactly between the MOT coils and parallel to them the magnetic field of the MOT decreases from its maximum value of about 120 Gauss to 0 Gauss at the center of the MOT. Although the magnetic field strength should vary as a square root with the position for optimal slowing [2], slowing can also be achieved in this field configuration.

To verify the efficiency of the slowing process in the magnetic field of the MOT a computer calculation with the slowing laser parameters used in the experiments is performed. The on-resonance saturation parameter of the slowing laser is $s_0 = 400$ and the detuning from atomic resonance -54 MHz. The results are shown in figure 3.2. A large part of the velocity distribution is slowed down to a velocity of about 8 m/s. This peak near 8 m/s has a very narrow width which means that the slowed atoms are also very cold. These atoms can easily be trapped

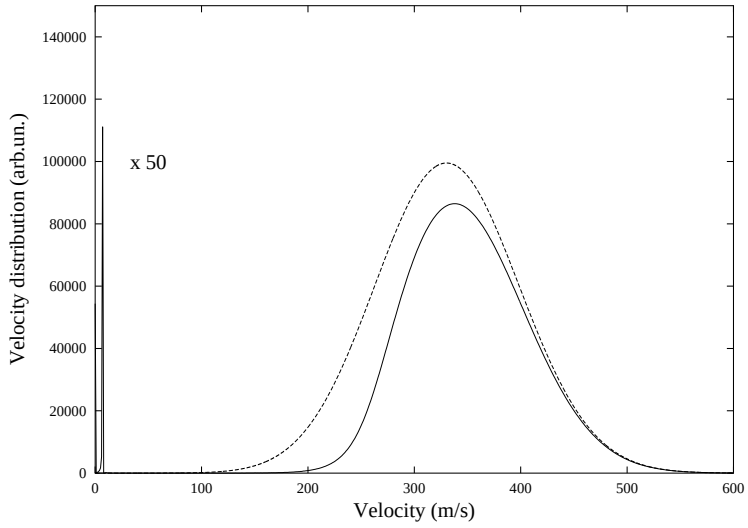

Figure 3.2 Computer calculation of the slowing process in the MOT magnetic field. The dashed curve is the unslowed velocity distribution with a mean velocity of 300 m/s and a velocity width of 100 m/s. The solid curve is the slowed distribution using a saturation parameter of $s_0 = 400$ and a detuning of -54 MHz for the slowing laser. As can be seen from the figure a large part of the velocity distribution can be cooled and slowed towards a velocity of about 8 m/s, which is far below the capture velocity of the MOT. The slowed peak is divided by a factor 50, because the peak is much higher than the unslowed distribution.

in the MOT.

Without the need of a Zeeman slower the setup is much shorter. For a given capture cross section of the MOT the solid angle increases, which results in a higher loading rate of the MOT. Another advantage of this setup is that the slowing takes place only in the last 200 mm before the atoms are captured in the MOT. Hence the divergence of the atomic beam caused by the increase of the ratio of the transverse velocity and the longitudinal velocity is strongly reduced. A disadvantage of this setup is that varying the MOT parameters by changing the magnetic field simultaneously changes the slowing process. A schematic view of the experimental setup is shown in figure 3.3.

Although the source can be connected directly to the MOT vacuum chamber a

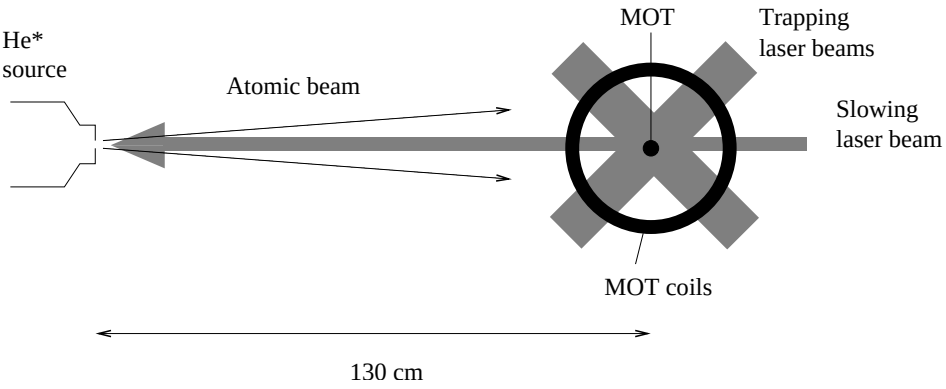

Figure 3.3 Top view of the experimental setup.

differential pumping section is included in the setup to reduce the gas load to the MOT vacuum chamber. In this way a pressure of $1 \cdot 10^{-9}$ mbar is reached in the MOT vacuum chamber. The setup is being pumped by magnetically suspended turbo molecular pumps (Balzers, types TCM 180 and TCM 520). The slowing laser light is provided by a diode laser (Spectra Diode Lab, SDL-6702-H1), which is fed by a home-built supply. The laser light is linearly polarized and has a linewidth of 3 MHz. The laser beam profile is shaped to a 9x25 mm^2 rectangular beam by a cylindrical telescope. The on-resonance saturation parameter for the expanded laser beam is $s_0 = 400$. Before the laser beam enters the setup the polarization is made circular by a quarter wave plate. The laser light slows the atoms down at the $2^3\mathrm{S}_1 \rightarrow 2^3\mathrm{P}_2$ transition at 1083 nm. The frequency of the laser is locked using saturated absorption spectroscopy as described for one of the lasers in section 2.4.2. The laser can be locked at a detuning by applying a homogeneous magnetic field to the glass cell in the saturated absorption spectroscopy setup. The detuning of the slowing laser is chosen so that the ionization signal of the MOT is optimal, which means that the loading rate of the MOT is highest. This optimal detuning is found to be -54 MHz from atomic resonance.

3.4 The magneto-optical trap

The principles of the MOT are described in section 2.2. Here only a description of the physical setup and its characteristics are given.

3.4.1 Construction

The MOT vacuum chamber is being pumped by a turbo molecular pump (Balzers, TPU 180HM). The background pressure in the vacuum chamber is usually $1 \cdot 10^{-9}$ mbar (without atomic beam) but pressures as low as $6 \cdot 10^{-10}$ mbar have been reached. This pressure is low enough that the main trap loss mechanism from our trap is intra-MOT collisions and not collisions with background particles [22].

The coils providing the magnetic field both have 588 windings and have an inner radius of 180 mm and an outer radius of 235 mm. They are connected in an anti-Helmholtz configuration. With a current of 10 A through the coils the magnetic field gradient in the z direction at the center of the trap is 15 G/cm. The coils are water cooled in order to avoid damage to the isolation of the wires.

The trapping laser light is provided by a laser of the same type as the other diode lasers used in this thesis (Spectra Diode Lab, SDL-6702-H1). The trapping laser beam passes through an optical isolator to avoid optical feedback, because the laser beam is retro-reflected to produce the counter-propagating laser beams after it has passed the vacuum chamber in three linearly independent directions. The optical isolator prevents the laser beam to shine back into the laser cavity, because optical feedback can cause unstable laser operation. The recycling scheme is possible in our case, since the density of the MOT is not so high that the intensity of the trapping light is significantly decreased during its passage through the MOT. If the MOT were opaque the recycling scheme would lead to unbalanced radiation forces and consequently to an unstable MOT cloud. The laser beam is made circularly polarized by a quarter wave plate and expanded by a spherical telescope to an almost spherical laser beam with a 10 mm radius. The saturation parameter of the laser light after the telescope is s_0 =180. The laser frequency is locked using saturated absorption spectroscopy. The MOT operates at a detuning of -14 MHz from atomic resonance.

As described in chapter 1 metastable helium atoms have a large internal energy (19.8 eV) and can ionize almost any other atom or molecule in a close collision. This is called Penning Ionization (PI). The PI reactions including Associative Ionization (AI) in which the molecular ion He_2^+ is produced are given in chapter 1. In reference [22] it is shown that the dominant ion production comes from collisions between two atoms in the MOT. The ions are detected by a micro-channel plate detector (MCP) situated 70 mm from the position of the MOT and oriented perpendicular to the plane parallel to the MOT coils. The MCP has an 18 mm diameter and the voltage on the front plate is -2000 Volts. A grid in front of the MCP can be used to either attract or repel the positive ions. The MCP pulses are

amplified and a discriminator disregards pulses with a pulse height smaller than a certain threshold to diminish the amount of noise.

3.4.2 Results

The MOT characteristics are determined by using time-of-flight (TOF) measurements and imaging of the MOT fluorescence with a CCD camera. Since He* atoms have a large internal energy they can easily be detected by the MCP detector. The detection efficiency of neutrals by the MCP detector is about 60 %. Both the MOT laser and the slowing laser are detuned far to the red of the laser cooling transition for 250 ms. The He* atoms fly apart ballistically and the atoms in the solid angle of the MCP are detected. After this period the laser frequencies are switched back and the MOT can reload for 4.25 s. This sequence is repeated 50 times in order to get better statistics in the metastable signal. The slowing laser frequency also needs to be modulated, since it is detuned only 54 MHz below the cooling transition and the laser beam intersects with the MOT region. The slowing laser beam can exert light pressure on the atoms and distort the ballistic flight paths. If we do not modulate the slowing laser, the He* TOF signal changes. We assume that the detected TOF spectrum corresponds to a Maxwell-Boltzmann distribution. Simulations have shown that gravity plays no role at our MOT temperature, because we have calculated that only 3.8 % less atoms reach the detector than the number of atoms expected based on the solid angle and no gravity.

The Maxwell-Boltzmann distribution is converted into a time distribution $f(t)$ to fit the data. The TOF data and a fit to the data are shown in figure 3.4. The MOT temperature extracted from the fit is $T = 1.9 \pm 0.1$ mK. This corresponds to a mean velocity of the atoms in the MOT of 2.8 m/s. The number of atoms in the MOT can be estimated by the number of detected atoms divided by the detection efficiency and the solid angle spanned by the MCP. This amounts to $1.3 \cdot 10^5$ atoms in the MOT.

Making a CCD image of a He* MOT is not straightforward. The fluorescent light from the atoms in the MOT has a wavelength of 1083 nm and most CCD cameras are not sensitive to this wavelength. A way to solve this is by exciting the 2^3P atoms in the MOT to the 3^3D state with light at 587.6 nm. This wavelength is in the visible regime and can be provided by a dye laser. This technique has been used by Kumakura and Morita [25]. The dye laser beam overlaps with the MOT cloud and is retro-reflected. In this way the dye laser will not blow away atoms out of the MOT when it is on resonance with the $2^3\text{P} \rightarrow 3^3\text{D}$ transition, but only change its shape. The linewidth for the $2^3\text{P} \rightarrow 3^3\text{D}$ transition is $\Gamma = 71.4$ MHz,

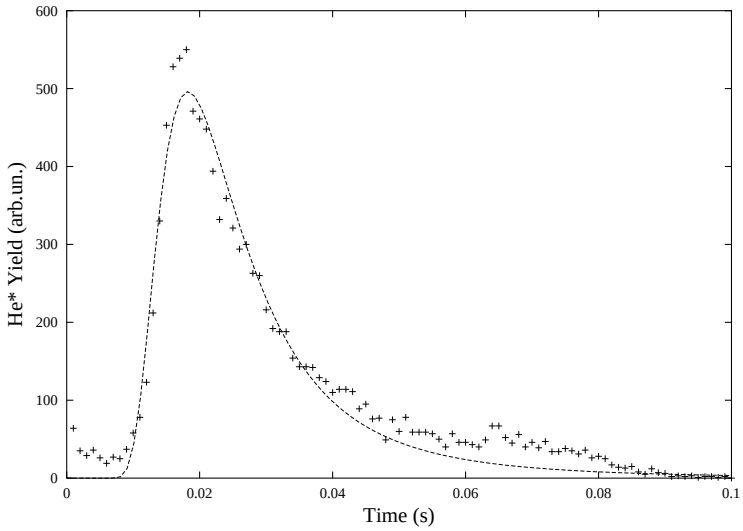

Figure 3.4 Time-of-flight spectrum of the MOT. The solid line is a fit to the data. The fit function is a Maxwell-Boltzmann distribution converted into a time distribution.

so the maximum force is more than 13 times larger than the maximum force for the 2^3S$\rightarrow 2^3$P transition. The saturation parameter for the dye laser is chosen to be small ($s_0 = 1$) in order not to disturb the MOT appreciably.

The MOT is visible as an orange cloud and the fluorescence is imaged onto a 752x582 pixels CCD camera via a lens inside the vacuum. A CCD image of the MOT is shown in figure 3.5 (a) and a horizontal cut through it in figure 3.5 (b). For a low density MOT the density profile can be shown to be Gaussian [26]. The standard deviation of the Gaussian distribution is conveniently called the width in what follows. We define r_x to be the width of the MOT in the direction of the dye laser beam and r_y the width in the direction perpendicular to this, but in the plane parallel to the two MOT coils. The width of the MOT perpendicular to this plane is called r_z. The dye laser beam elongates the MOT in the x direction and since the magnetic field in the z direction is twice as strong as the magnetic field in either the x or y direction the half width r_y is $\sqrt{2}$ times larger than r_z. Taking all this into account we found $r_x = 0.43$ mm, $r_y = 0.26$ mm and $r_z = 0.18$ mm. Assuming that r_x is equal to r_y if the dye laser beam is turned off, the total

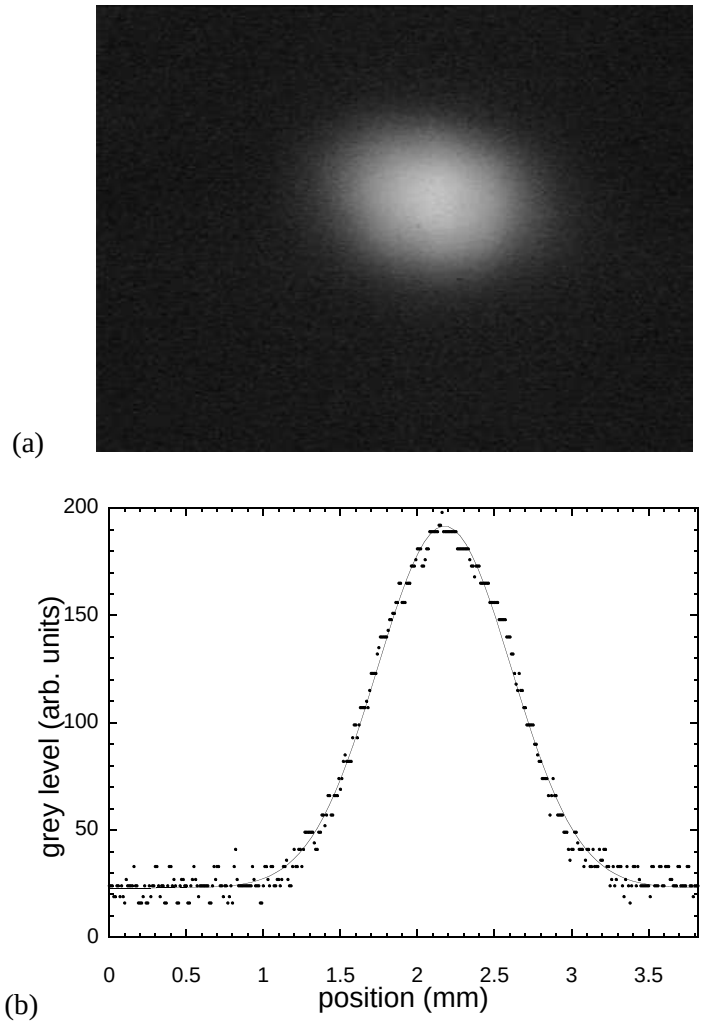

Figure 3.5 (a) CCD image of the MOT. (b) Horizontal cut through figure (a). The dots show the intensity of the fluorescence in arbitrary units and the solid line is a Gaussian fit to the dots.

volume of the MOT is $5.3 \cdot 10^{-5}\text{cm}^3$.

The total amount of fluorescence f detected is 2.5 nW. The number of atoms

in the MOT can be derived from the fluorescence by using

$$N = \frac{f}{\eta_d \eta_e h\nu_l \rho_e \Gamma} , \tag{3.1}$$

with $\eta_d = 0.016$ the geometrical detection efficiency, $\eta_e = 0.25$ is the detection efficiency accounting for losses from optical elements, $h\nu_l = 3.377 \cdot 10^{-19}$ J is the energy of the $2^3\mathrm{P} \leftrightarrow 3^3\mathrm{D}$ photon and $\rho_e = 0.05$ is the excited state fraction. The last parameter has been evaluated by numerically solving the optical Bloch equations for a three-level system. The number of atoms is $1.7 \cdot 10^5$, which is consistent with the number of atoms estimated from the TOF measurement. The central density of the MOT is about $3 \cdot 10^9$ cm^{-3}.

The relation between the MOT temperature T and the mean square radius $\langle r^2 \rangle$ of the MOT is given by [26]

$$\frac{1}{2} k_B T = \frac{1}{2} \kappa \langle r^2 \rangle , \tag{3.2}$$

with k_B Boltzmann's constant. The spring constant κ can be estimated to be $\kappa = 1.02 \cdot 10^{-20}$ kg s^{-2} by using equation 2.9 with $s_0 = 70$ and $\delta_l = -8.6\Gamma$. The MOT temperature is then $T = 0.5$ mK which is almost four times lower than the temperature observed in the TOF measurement. The calculated temperature is only a rough estimate, since equation 3.2 is only valid for two-level atoms, which is clearly not the case for He*.

3.5 The probe laser setup

Once a sample of cold atoms is created with the setup described in the previous sections an additional laser is used for the photoassociation experiments. This laser is called the probe laser. It is scanned in frequency and the ionization signal caused by Penning collisions inside the MOT can be studied as a function of the probe laser frequency.

The probe laser is of the same type as all the other diode lasers mentioned in this thesis. An overview of the probe laser setup is shown in figure 3.6. The probe laser beam is directed onto the MOT cloud, because the maximum number of atom pairs can be excited by the light when the overlap between the MOT cloud and the probe laser beam is optimized. If a higher laser intensity is needed at the position of the MOT the laser beam can be focused by a lens. In the high intensity experiments we actually used a telescope composed of two lenses with a focal

length of 300 mm. In this way the position of the focus of the laser beam can be varied over a large range. For low probe laser intensities a $\lambda/2$ retardation plate is used to reduce the polarization component transmitted by a polarizing beam splitter cube. The transmitted laser beam is used as the probe laser beam.

The atoms in the MOT will be blown away when the probe laser frequency is near the $2^3S_1 \rightarrow 2^3P_{0,1,2}$ transitions. Although the laser beam is not retro-reflected, an optical isolator is placed right behind the probe laser in order to reduce frequency instabilities due to reflections back into the laser diode (figure 3.6). Two beam splitters split off 5 % of the light from the main laser beam. One

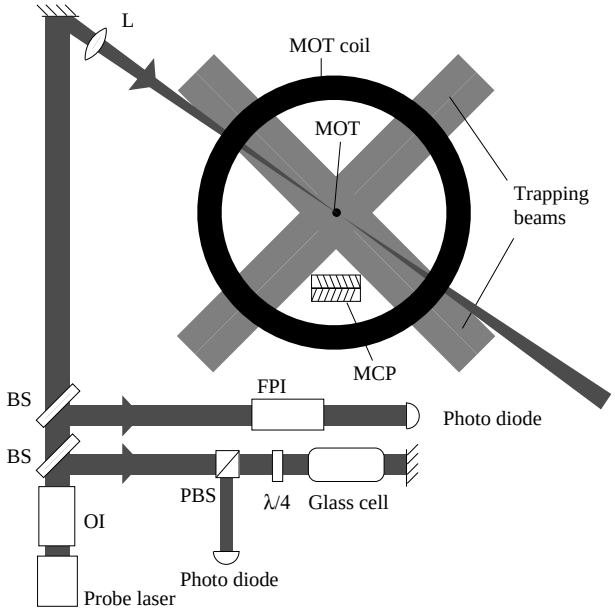

Figure 3.6 Top view of the probe laser setup. In the figure OI stands for optical isolator, BS for a 5 % beam splitter, PBS for polarizing beam splitter, $\lambda/4$ for quarter wave plate, FPI for Fabry-Pérot interferometer, MCP for microchannel plates and L for lens.

beam runs through a Fabry-Pérot interferometer (FPI) with a free spectral range of about 2 GHz and is detected by a photo diode. This is used for the relative frequency reference. The other laser beam runs through a saturated absorption spectroscopy setup and is used for the absolute frequency reference. A sinusoidal

voltage with a frequency of 2.3 kHz applied to the probe laser modulates the laser frequency. The signal from the photo diode in the saturated absorption spectroscopy setup is fed to a lock-in amplifier together with a reference signal of the same frequency. The output of the lock-in amplifier and the FPI signal are both digitized with an ADC module in a computer and recorded simultaneously with the MOT ionization signal.

The probe laser frequency is scanned with a sawtooth modulation over a period of typically 100 s. The frequency tuning of the diode laser is 290 MHz/Volt. The frequency is usually scanned over several GHz around the $2^3S_1 \rightarrow 2^3P_{0,1,2}$ atomic transitions. The FPI peaks are used as relative frequency markers and the Lamb dip in the output of the lock-in amplifier as an absolute frequency marker. This allows us to calibrate the frequency scale.

3.6 Conclusions

We have built a MOT for metastable helium, which is loaded from a liquid helium cooled DC discharge source. The atoms leave the source with a mean velocity of 300 m/s and are slowed down by a counter-propagating laser beam. The required Zeeman shift to keep the atoms in resonance with the laser light is provided by the MOT magnetic field. We trap a few times 10^5 atoms in the MOT at a density of $3 \cdot 10^9$ cm^{-3}. The volume of the MOT cloud is about $5 \cdot 10^{-5}$ cm^3. With TOF techniques the temperature of the atoms in the trap is determined to be 1.9 mK.

Chapter 4

Molecular symmetries of the He(2^3S)+He(2^3S,2^3P) system

4.1 Introduction

A molecular Hamiltonian is invariant under certain symmetry transformations, which allows a classification of the molecular eigenstates. Angular momenta play an important role in identifying the symmetry of a molecular state. The most simple molecules are homo-nuclear diatomic molecules, which means that the molecule consists of two atoms with identical nuclei. This is the case for the He(2^3S)+He(2^3S,2^3P) collision systems. In this thesis we will mainly study the long range behavior of these collision systems that are often referred to as quasi-molecules. The purpose of this chapter is to provide a theoretical background to understand the terminology used in the next chapters. In section 4.2 the Hund's cases and some symmetry operations are discussed. In section 4.3 Hund's case (a) wave functions for the He-He system are constructed and in section 4.4 the connection with Hund's case (c) wave functions is made. Section 4.5 deals with the molecular potentials and the rotational corrections. Finally, in section 4.6 the selection rules for dipole transitions are outlined.

4.2 Hund's cases and symmetry rules

The Hund's cases are discussed in section 4.2.2 and the symmetry rules are derived in section 4.2.3. Before this it is convenient to define which angular momenta are involved in diatomic molecules.

4.2.1 Angular momenta

Suppose, the molecule consists of two atoms a and b. Atom a has an electronic orbital angular momenta $\mathbf{l}_a$, and an electronic spin angular momentum $\mathbf{s}_a$, which add up to a total electronic angular momentum $\mathbf{j}_a = \mathbf{l}_a + \mathbf{s}_a$. The projections of $\mathbf{l}_a$, $\mathbf{s}_a$ and $\mathbf{j}_a$ on the internuclear axis are m_a^l, m_a^s and m_a^j. Similar angular momenta can be defined for atom b with the indices a replaced by b. The total electronic orbital angular momentum is $\mathbf{L} = \mathbf{l}_a + \mathbf{l}_b$ and the total electronic spin angular momentum is $\mathbf{S} = \mathbf{s}_a + \mathbf{s}_b$. These add up to the total electronic angular momentum $\mathbf{j} = \mathbf{L} + \mathbf{S}$. The nuclear spin angular momentum $\mathbf{I}$ does not play a role here, since we are dealing with ^{4}He with $I = 0$ (I is the quantum number associated with the operator $\mathbf{I}$). The nuclei can rotate around the center of mass of the molecule and this introduces the rotational angular momentum $\mathbf{l}$, which is perpendicular to the internuclear axis. Finally, the total molecular angular momentum is denoted by $\mathbf{J} = \mathbf{j} + \mathbf{l}$. Since $\mathbf{l}$ is perpendicular to the internuclear axis, $\mathbf{J}$ and $\mathbf{j}$ must have the same projection on the internuclear axis: $M^j = m_a^j + m_b^j$.

4.2.2 Hund's cases

When symmetry operations in molecules are discussed, it is convenient to define two different coordinate frames: the space-fixed frame and the molecule-fixed frame [28]. The space-fixed frame with the axes X, Y and Z is transformed to the molecule-fixed frame with the axes x, y and z by the rotation

$$\mathbf{R}(\phi, \theta, \chi) = \exp(-i\phi J_Z)\exp(-i\theta J_Y)\exp(-i\chi J_Z) \,, \tag{4.1}$$

where ϕ, θ and χ are the Euler angles, as indicated in figure 4.1, and J_Y and J_Z are the Y and Z components of the total molecular angular momentum. The molecular axis (internuclear axis) is chosen to be the z axis. In this thesis the symmetries of the molecules will be described in the molecule-fixed frame. In section 4.5.3 rotational corrections to the molecular energies are discussed.

The molecular Hamiltonian consists of various interaction terms, but here only the most important are taken into account. At long internuclear distances (> 500 a_0) the fine structure interaction is larger than the electrostatic interaction. At these internuclear distances the so called Hund's case (c) applies. The fine structure interaction gives rise to couplings between molecular states with different $\mathbf{L}$ and $\mathbf{S}$. It can be shown that the electronic Hamiltonian commutes with the operator j_z [29]. This means, that an eigenstate of j_z is also an eigenstate of the Hamiltonian and hence M^j is a good quantum number. We consider the reflection

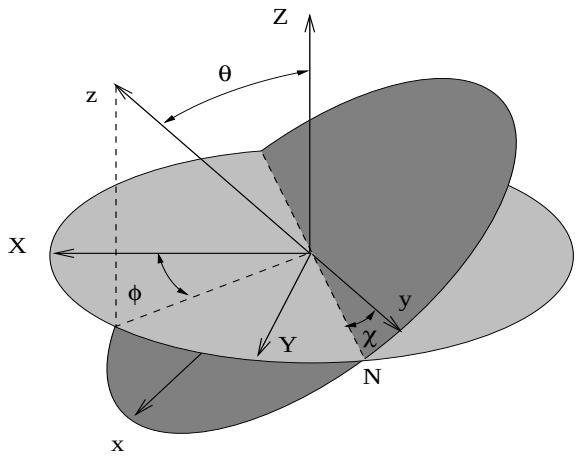

Figure 4.1 The space-fixed frame XYZ and the body-fixed frame xyz related to each other through the Euler angles ϕ, θ and χ. The line N in the figure indicates the intersection of the XY plane and the xy plane. The Y axis transforms into N after the rotation over ϕ around Z.

of this eigenstate through a plane containing the internuclear axis z. The reflection operator is denoted by $\sigma_v(xz)$. The eigenstate with quantum number M^j is transformed into the state with quantum number $-M^j$, because **j** is an axial vector and hence changes sign under this transformation. Since $\sigma_v(xz)$ commutes with the Hamiltonian, these states are degenerate. If $M^j = 0$ the eigenstate is converted into the same eigenstate with a multiplication factor and since $(\sigma_v(xz))^2$ brings the molecule back into its original state, this multiplication factor must be either +1 or -1. The molecular states are indicated with $\Omega = |M^j|$ and it can take the values 0,1,2 etc. The $\Omega = 0$ states have the $\pm$ symmetry under the reflection operation. It should be noted that this $\pm$ symmetry is assigned to the non-rotating part of the wave function. When rotation is taken into account, the reflection symmetry of the wave function changes.

Furthermore, homo-nuclear systems have an additional symmetry under the inversion i_e of the electron's coordinates (not the spins) through the midpoint of the internuclear axis (center of mass). When this operation is carried out twice, the molecule returns to its original state. Hence its eigenvalues are ± 1. Consequently, certain states have a positive symmetry under this inversion and these are

called gerade states. Other states have a negative symmetry and are called ungerade states. Summarizing, the Hund's case (c) states are indicated with the term symbols $^{2S+1}\Omega^{\pm}_{g/u}$ where $2S+1$ is the spin multiplicity, $\pm$ indicates the reflection symmetry and g/u stands for gerade/ungerade.

At short internuclear distances (in the region between 10 – 100 a_0) the electrostatic splitting due to Coulomb interactions is dominant. Here the fine structure interaction is negligible compared to the electrostatic splitting and the Hamiltonian commutes with j_z, L_z, $\mathbf{S}^2$ and S_z [29]. In this case, which is called the Hund's case (a), M^j, $M^L = m^l_a + m^l_b$, S and $\Sigma = m^s_a + m^s_b$ are all good quantum numbers. States with M^L and $-M^L$ are degenerate, except for $M^L = 0$ states, which have the $\pm$ reflection symmetry under $\sigma_v(xz)$. It should be noted that the $\pm$ symmetry is assigned to the spatial part of the wave function. The rotational part and the spin part can change the symmetry of the wave function under the reflection operation. Gerade and ungerade symmetry also applies to Hund's case (a). The term symbols for the molecular states are $^{2S+1}\Lambda^{\pm}_{g/u}$ with $\Lambda = |M^L|$. In the term symbol Λ can be denoted by Σ, Π, Δ and so on, corresponding to $\Lambda = 0, 1, 2$.

4.2.3 Symmetry rules

We choose a basis set $|l_a\ m^l_a; l_b\ m^l_b\rangle$ composed of the two atomic states $|l_a\ m^l_a\rangle$ and $|l_b\ m^l_b\rangle$. We ignore the spin part in this section, because it is not relevant for the derivation of the following symmetry rules. As mentioned before the diatomic molecule is symmetric under reflection in a plane containing the molecular axis z. The reflection symmetry is only relevant for Σ states ($M^L = 0$) as pointed out in the previous section and this is the case when $m^l_a = -m^l_b$ or when $m^l_a = m^l_b = 0$. Since reflection transforms states with $m^l_{a,b}$ into ones with $-m^l_{a,b}$, the $\Sigma^{\pm}$ states are linear combinations of products of the atomic wave functions:

$$|\psi_{mol}(\Sigma^{\pm})\rangle = |l_a\ +m; l_b\ -m\rangle \pm |l_a\ -m; l_b\ +m\rangle\ , \tag{4.2}$$

with $|m| = |m_a| = |m_b|$. In the He(2^3S)+He(2^3S) complex both atoms have $l = 0$ and for He(2^3S)+ He(2^3P) one atom has $l = 0$ and the other $l = 1$. The Σ states can only be formed with $m^l_a = m^l_b = 0$ and the symmetry can be determined as follows.

From group theory it is known that the reflection operator $\sigma_v(xz)$ performs the same operation as an inversion i_t of all spatial coordinates with respect to the origin (midpoint of the internuclear axis) followed by a rotation $C_2(y)$ of 180 °

about the y axis (axis perpendicular to the internuclear axis) [28]. Inversion i_t (the parity operator) of the atomic state $|l_a\ m_a\rangle$ gives

$$i_t|l_a\ m_a^l\rangle = (-1)^{\sum_i l_i}|l_a\ m_a^l\rangle\ , \tag{4.3}$$

where the sum is over the orbital angular momenta of the electrons at atom a. The factor $(-1)^{\sum_i l_i}$ is the atomic parity π_a. Applying the rotation $C_2(y)$ to $|l_a\ m_a\rangle$ yields

$$C_2(y)|l_a\ m_a^l\rangle = (-1)^{l_a - m_a^l}|l_a\ -m_a^l\rangle\ . \tag{4.4}$$

We can write down the same equations for atom b and for the reflection operation on the molecular state $|l_a\ m_a^l; l_b\ m_b^l\rangle$ we get

$$\sigma_v(xz)|l_a\ m_a^l; l_b\ m_b^l\rangle = \pi_a\pi_b(-1)^{l_a+l_b-m_a^l-m_b^l}|l_a\ -m_a^l; l_b\ -m_b^l\rangle\ . \tag{4.5}$$

Since $m_a^l = m_b^l = 0$ the symmetry is given by $\pi_a\pi_b(-1)^{l_a+l_b}$ and this is always +1 for both He(2^3S)+He(2^3S) and He(2^3S)+He(2^3P). Hence, for $M^L = 0$ only Σ^+ states can be constructed.

Next, we discuss the inversion i_e of the electronic coordinates with respect to the origin (the center of mass of the nuclei). The gerade/ungerade symmetry (see previous subsection) only exists for homo-nuclear diatomic molecules. It is easy to see, that this operation is identical to the parity operator, i_t, followed by the inversion of the nuclei with respect to the origin, i_N. The first operation multiplies the molecular basis functions with $\pi_a\pi_b$. Applying i_e to the basis functions yields

$$i_e|l_a\ m_a^l; l_b\ m_b^l\rangle = \pi_a\pi_b|l_b\ m_b^l; l_a\ m_a^l\rangle\ , \tag{4.6}$$

where the labels a and b are interchanged. Obviously, the basis functions are not eigenstates of the operator i_e and linear combinations must be formed to achieve this.

4.3 Construction of molecular wave functions for helium

Helium has two electrons and consequently, a helium molecule has four electrons. Helium has two electrons and in the metastable state it has no filled shell, so both electrons are valence electrons. Consequently, a helium molecule has four valence electrons. For helium it is more complicated to construct wave functions with the right symmetries than for alkali dimers, which only have two valence electrons. The Pauli principle states that the wave function must change sign

when two electrons are interchanged. When two electrons are interchanged in He(2^3S)+He(2^3S,2^3P) molecules the atomic spin states can change to singlet spin states which completely changes the collision system. Nevertheless, the exchange of two electrons from atom a to atom b, and vice versa, should leave the wave function unchanged, since an electron pair is a boson. According to [30] it is not allowed to separate the orbital and the spin part for molecules with more than two electrons, but we still use it here since we are only interested in the symmetry properties of the electronic wave functions. First we will discuss the spin states for molecular helium.

4.3.1 Spin states in molecular helium

Both helium atoms have $s = 1$ and $m^s = -1, 0, 1$. These quantum numbers are defined in section 4.2.1. The total spin can take the values $S = 0, 1, 2$ with $S = s_a + s_b$. The $|S\ \Sigma\rangle = |2\ 2\rangle$ spin state can be constructed easily: all four electrons must have spin up. If we define $\Uparrow$ for $m^s = +1$, $\Leftrightarrow$ for $m^s = 0$ and $\Downarrow$ for $m^s = -1$, this state can be written as $|S\ \Sigma\rangle = \Uparrow\Uparrow$. The spin states $|2\ \Sigma\rangle$ with $\Sigma = 1, 0, -1$ and -2 can be found by applying the $S_- = s_{a-} + s_{b-}$ operator. The s_- operators are given by

$$s_-|s\ \ m^s\rangle = [(s + m^s)(s - m^s + 1)]^{1/2}\,|s\ \ m^s - 1\rangle\ . \tag{4.7}$$

The eigenstate $|S = 2\ \Sigma = 1\rangle$ is found to be $|2\ 1\rangle = \Uparrow\Leftrightarrow + \Leftrightarrow\Uparrow$. The state $|1\ 1\rangle$ must be a linear combination of $\Uparrow\Leftrightarrow$ and $\Leftrightarrow\Uparrow$ which is orthogonal to the $|2\ 1\rangle$ state. Hence, the $|1\ 1\rangle$ state must be $|1\ 1\rangle = \Uparrow\Leftrightarrow - \Leftrightarrow\Uparrow$. The other states in the $S = 1$ multiplet are found by applying the S_- operator. Finally, the $|0\ 0\rangle$ state must be orthogonal to both the $|2\ 0\rangle$ and $|1\ 0\rangle$ states. Summarizing, using this procedure one can construct 5 quintet states, 3 triplet states and 1 singlet state and they are given by

$$\begin{array}{lll} & |0\ 0\rangle = \Downarrow\Uparrow - \Leftrightarrow\Leftrightarrow + \Uparrow\Downarrow & \\ |1\ -1\rangle = \Leftrightarrow\Downarrow - \Downarrow\Leftrightarrow & |1\ 0\rangle = \Uparrow\Downarrow - \Downarrow\Uparrow & |1\ +1\rangle = \Uparrow\Leftrightarrow - \Leftrightarrow\Uparrow \\ |2\ -2\rangle = \Downarrow\Downarrow & |2\ -1\rangle = \Leftrightarrow\Downarrow + \Downarrow\Leftrightarrow & |2\ 0\rangle = \Uparrow\Downarrow + 2 \Leftrightarrow\Leftrightarrow + \Downarrow\Uparrow \\ |2\ +1\rangle = \Uparrow\Leftrightarrow + \Leftrightarrow\Uparrow & |2\ +2\rangle = \Uparrow\Uparrow\ . & \end{array} \tag{4.8}$$

It should be noted that the spin functions are not normalized here. It can be seen that the quintet states and the singlet state are symmetric for the exchange of an electron pair and the triplet state is antisymmetric. Since the total wave function must be symmetric for the exchange of an electron pair, this means that

the accompanying spatial wave functions must be symmetric and antisymmetric, respectively.

4.3.2 He(2^3S)+He(2^3S) wave functions

To construct wave functions for the He(2^3S)+He(2^3S) states, Slater determinants can be used. In the He(2^3S) state one electron is in the $1s$ state and the other in the $2s$ state. They can have spin up or spin down. The atoms are identical, so $2^4 = 16$ different Slater determinants can be formed. This number corresponds to the 16 spin states that can be formed by four electrons. Only a subspace of 9 states, which are linear combinations of the Slater determinants, belong to the ^{3}S-^{3}S asymptote (the others belong to the ^{1}S-^{3}S or ^{1}S-^{1}S asymptote). The linear combinations of the Slater determinants must be constructed such that the one-electron spins form the spin states as described in section 4.3.1. For example, the Slater determinant with all spins up can be written as

$$\phi(1,2,3,4) = \sum_{i=1}^{24}(-1)^{N(P_i)} P_i \psi_{1s}^a(1)\alpha(1)\psi_{2s}^a(2)\alpha(2)\psi_{1s}^b(3)\alpha(3)\psi_{2s}^b(4)\alpha(4) \; , \tag{4.9}$$

with 1,2,3 and 4 denoting the electron's coordinates and $\alpha(i)$ is the one electron spinor for $m^s = +1/2$. The permutation operator P_i rearranges the order of the four electrons and $N(P_i)$ is the number of permutations required to change the sequence (1,2,3,4) into the new sequence. As can be seen from equation 4.8 this single determinant belongs to the wave function with the $|2\,2\rangle$ spin state and no other determinants are possible. If we define a two-electron wave function as

$$\Upsilon_{1s2s}^{a,b}(i,j) = \psi_{1s}^{a,b}(i)\psi_{2s}^{a,b}(j) - \psi_{1s}^{a,b}(j)\psi_{2s}^{a,b}(i) \; , \tag{4.10}$$

then, after rearrangement of the 24 terms in equation 4.9, $\phi(1,2,3,4)$ can be rewritten as

$$\begin{aligned}\phi(1,2,3,4) = \{&\Upsilon_{1s2s}^a(1,2)\Upsilon_{1s2s}^b(3,4) + \Upsilon_{1s2s}^a(1,3)\Upsilon_{1s2s}^b(2,4) + \\ &\Upsilon_{1s2s}^a(1,4)\Upsilon_{1s2s}^b(2,3) + \Upsilon_{1s2s}^a(2,3)\Upsilon_{1s2s}^b(1,4) + \Upsilon_{1s2s}^a(2,4)\Upsilon_{1s2s}^b(1,3) + \\ &\Upsilon_{1s2s}^a(3,4)\Upsilon_{1s2s}^b(1,2)\}\alpha(1)\alpha(2)\alpha(3)\alpha(4) \; .\end{aligned} \tag{4.11}$$

Now we can define the four-electron wave function

$$\Theta_{1s2s,1s2s}^{\alpha}((i,j),(k,l)) = \Upsilon_{1s2s}^a(i,j)\Upsilon_{1s2s}^b(k,l) + \alpha\Upsilon_{1s2s}^a(k,l)\Upsilon_{1s2s}^b(i,j) \; , \tag{4.12}$$

where the wave function $\Theta^{\alpha}_{m,n}$ is the linear combination of one electron pair at nucleus a while the other pair is at nucleus b and vice versa. The indices m and n denote the atomic states. The index α (not to be confused with the one electron spinor) indicates the symmetry of this wave function when the electron pairs are interchanged. An electron pair is a boson so the spatial wave function must be symmetric, if the spin wave function is symmetric. Equation 4.11 can be reduced to

$$\begin{aligned}\phi(1,2,3,4) &= \{\Theta^{+}_{1s2s,1s2s}((1,2),(3,4)) + \Theta^{+}_{1s2s,1s2s}((1,3),(2,4)) + \\ &\quad \Theta^{+}_{1s2s,1s2s}((1,4),(2,3))\}\alpha(1)\alpha(2)\alpha(3)\alpha(4)\ . \end{aligned} \tag{4.13}$$

If one electron pair is indicated by p and the other by q, the wave function can be further simplified to

$$\phi(p,q) = \Theta^{+}_{1s2s,1s2s}(p,q) \Uparrow (p) \Uparrow (q) \tag{4.14}$$

where the four electron wave function is generalized as

$$\Theta^{\alpha}_{m,n}(p,q) = \Upsilon^{a}_{m}(p)\Upsilon^{b}_{n}(q) + \alpha\Upsilon^{a}_{m}(q)\Upsilon^{b}_{n}(p)\ , \tag{4.15}$$

with m, n the atomic states. All electrons are in the s state so $\Lambda = 0$. As was mentioned in section 4.2.3, all Σ states have positive reflection symmetry. Equation 4.6 can be used to determine whether this is a gerade or ungerade state. Since $\pi_a\pi_b = 1$ and equation 4.15 gives a factor α when the electrons of the two atoms are interchanged (note that $m = n$), this must be the $\Sigma = 2$ component of the ${}^5\Sigma^{+}_{g}$ state.

The same considerations can be applied to all the He(2^3S)+He(2^3S) states and we obtain

$${}^5\Sigma^{+}_{g} : \Theta^{+}_{1s2s,1s2s}|2\ \Sigma\rangle \quad {}^3\Sigma^{+}_{u} : \Theta^{-}_{1s2s,1s2s}|1\ \Sigma\rangle \quad {}^1\Sigma^{+}_{g} : \Theta^{+}_{1s2s,1s2s}|0\ \Sigma\rangle$$

The wave functions are written in a similar fashion as done by Linder *et al.* [31] for the alkalis and the spin functions are given by equation 4.8.

4.3.3 He(2^3S)+He(2^3P) wave functions

In a similar way the wave functions for the He(2^3S)+He(2^3P) asymptote can be constructed. In the Slater determinants the one-electron wave functions for each electron at either nucleus can be $\psi_{1s}(i)$, $\psi_{2s}(i)$, $\psi_{2p_{-1}}(i)$, $\psi_{2p_0}(i)$ and $\psi_{2p_{+1}}(i)$

combined with spin up or down. The index i =1,2,3 or 4 denotes the electron's coordinate. If atom a is in the $1s2s$ state and atom b in the $1s2p$ state, the number of possible states for the total wave function is 2x2x2x6=48. Here 2 accounts for the two possible s states ($m^l = 0$ and $m^s = \pm 1/2$) and 6 is the number of possible p states ($m^l = -1, 0, +1$ and $m^s = \pm 1/2$). With atom a in the $1s2p$ state and atom b in the $1s2s$ state the same number of states can be formed, resulting in a total of 96 states. Of these states 3x3x6=54 connect to the ^{3}S-^{3}P asymptote (the first two numbers are the number of spin states and 6 is the number of p states at either nucleus a or b), 3x1x6=18 to the ^{3}S-^{1}P asymptote, 1x3x6=18 to the ^{1}S-^{3}P asymptote and 1x1x6 to the ^{1}S-^{1}P asymptote. For the ^{3}S-^{3}P asymptote 6 states belong to a singlet spin, 18 to 6 triplet states and 30 to 6 quintet states. Finally, 1/3 of the states are Σ states and 2/3 are Π states and both can have either gerade or ungerade symmetry.

Generally, one can show for the part of the wave function that depends on Λ, S and Σ that

$$\begin{aligned} |\Lambda S\Sigma\rangle &= \{\Upsilon^a_m(p)\Upsilon^b_n(q) + (-1)^S\Upsilon^a_m(q)\Upsilon^b_n(p) + \\ &\quad \pi_a\pi_b(-1)^{\sigma+S}(\Upsilon^a_n(p)\Upsilon^b_m(q) + (-1)^S\Upsilon^a_n(q)\Upsilon^b_m(p))\}|S\Sigma\rangle \\ &= \{\Theta^\alpha_{m,n}(p,q) + \pi_a\pi_b(-1)^{\sigma+S}\Theta^\alpha_{n,m}(p,q)\}|S\Sigma\rangle\ , \end{aligned} \tag{4.16}$$

where σ denotes the gerade/ungerade symmetry of the state. If $\sigma = 0(1)$ the state is gerade (ungerade). Here, the definition of $\Theta^\alpha_{m,n}(p,q)$ is given by equation 4.15. Furthermore, $\alpha = (-1)^S$ and this can be derived by applying the permutation of two electron pairs to the wave function and using the symmetry properties of the Clebsch-Gordan coefficients. The multiplication factor for the second term in the right-hand side of equation 4.16 can be found by the inversion operation (equation 4.6). Equation 4.16 can be used to derive that

$$\begin{aligned} {}^5\Sigma^+_g &: (\Theta^+_{1s2s,1s2p_0} - \Theta^+_{1s2p_0,1s2s})|2\ \Sigma\rangle \\ {}^5\Sigma^+_u &: (\Theta^+_{1s2s,1s2p_0} + \Theta^+_{1s2p_0,1s2s})|2\ \Sigma\rangle \\ {}^3\Sigma^+_u &: (\Theta^-_{1s2s,1s2p_0} - \Theta^-_{1s2p_0,1s2s})|1\ \Sigma\rangle \\ {}^3\Sigma^+_g &: (\Theta^-_{1s2s,1s2p_0} + \Theta^-_{1s2p_0,1s2s})|1\ \Sigma\rangle \\ {}^1\Sigma^+_g &: (\Theta^+_{1s2s,1s2p_0} - \Theta^+_{1s2p_0,1s2s})|0\ \Sigma\rangle \\ {}^1\Sigma^+_u &: (\Theta^+_{1s2s,1s2p_0} + \Theta^+_{1s2p_0,1s2s})|0\ \Sigma\rangle \\ {}^5\Pi_g &: (\Theta^+_{1s2s,1s2p_{\pm1}} - \Theta^+_{1s2p_{\pm1},1s2s})|2\ \Sigma\rangle \\ {}^5\Pi_u &: (\Theta^+_{1s2s,1s2p_{\pm1}} + \Theta^+_{1s2p_{\pm1},1s2s})|2\ \Sigma\rangle \end{aligned}$$

$$
\begin{aligned}
^3\Pi_u &: (\Theta^-_{1s2s,1s2p_{\pm1}} - \Theta^-_{1s2p_{\pm1},1s2s})|1\ \Sigma\rangle \\
^3\Pi_g &: (\Theta^-_{1s2s,1s2p_{\pm1}} + \Theta^-_{1s2p_{\pm1},1s2s})|1\ \Sigma\rangle \\
^1\Pi_g &: (\Theta^+_{1s2s,1s2p_{\pm1}} - \Theta^+_{1s2p_{\pm1},1s2s})|0\ \Sigma\rangle \\
^1\Pi_u &: (\Theta^+_{1s2s,1s2p_{\pm1}} + \Theta^+_{1s2p_{\pm1},1s2s})|0\ \Sigma\rangle
\end{aligned}
$$

4.4 Connection between Hund's case (a) and (c)

The molecular basis set introduced in section 4.2.3 together with the spin part form a basis set for the non-rotating molecule, composed of atomic states. This basis set is valid at short internuclear distances. At large internuclear distances new basis functions are needed because the fine structure interaction is not diagonal in the above mentioned basis set. The new basis functions are also composed of atomic states, but with the quantum numbers j_a, j_b, m_a^j and m_b^j. They are given by

$$|\psi_{mol}\rangle = |j_a m_a^j\ ; j_b m_b^j\rangle\ . \tag{4.17}$$

The new basis set can be expanded into the old basis set using Clebsch-Gordan coefficients. The molecular state $|j_a m_a^j\ ; j_b m_b^j\rangle$ can be written as

$$
\begin{aligned}
|j_a m_a^j\ ; j_b m_b^j\rangle = \sum_{m_a^l, m_a^s, m_b^l, m_b^s} \Big(&\langle l_a m_a^l\ ; s_a m_a^s | j_a m_a^j\rangle \langle l_b m_b^l\ ; s_b m_b^s | j_b m_b^j\rangle \\
&\times |l_a m_a^l\ ; s_a m_a^s\rangle |l_b m_b^l\ ; s_b m_b^s\rangle \Big)\ .
\end{aligned} \tag{4.18}
$$

The basis functions $|j_a m_a^j; j_b m_b^j\rangle$ can be separated with respect to their value of the quantum number $\Omega = |M^j|$ as shown below:

$\Omega = 0$	$\|(2s)10;(2p)00\rangle$	$\|(2s)10;(2p)10\rangle$	$\|(2s)1+1;(2p)1-1\rangle$
	$\|(2s)1-1;(2p)1+1\rangle$	$\|(2s)10;(2p)20\rangle$	$\|(2s)1+1;(2p)2-1\rangle$
	$\|(2s)1+1;(2p)1-1\rangle$		
$\Omega = 1$	$\|(2s)1+1;(2p)00\rangle$	$\|(2s)10;(2p)1+1\rangle$	$\|(2s)1+1;(2p)10\rangle$
	$\|(2s)10;(2p)2+1\rangle$	$\|(2s)1+1;(2p)20\rangle$	$\|(2s)1-1;(2p)2+2\rangle$
$\Omega = 2$	$\|(2s)1+1;(2p)1+1\rangle$	$\|(2s)1+1;(2p)2+1\rangle$	$\|(2s)10;(2p)2+2\rangle$
$\Omega = 3$	$\|(2s)1+1;(2p)2+2\rangle$		

The electron's state in parentheses indicates that for the wave functions in the equation above the $2p$ electron is at nucleus b. The wave functions with the $2p$ electron at nucleus a also have to be included in the basis. The basis functions are

not eigenfunctions of the Hamiltonian and do not have the required symmetries. Linear combinations of the wave functions with the $2p$ electron at nucleus a and b provide the gerade or ungerade symmetry. For $\Omega = 0$ each gerade or ungerade state also has a definite reflection symmetry. For $\Omega \neq 0$ the states are doubly degenerate. Therefore, the total number of states is 2x7 ($0_{g,u}$) + 2x2x6 ($1_{g,u}$) + 3 ($2_{g,u}$) + 1 ($3_{g,u}$)=54 which is the same as the number of Hund's case (a) states we found in section 4.3.3. Clearly, the number of states connected to the He(2^3S)+He(2^3P) asymptote has to be the same in the two representations.

The total electronic angular momentum for the 2^3S atom is 1 and the 2^3P atom can have a total electronic angular momentum of 0, 1 and 2. The fine structure interaction causes that states with different total electronic angular momenta for the 2^3P atom have different asymptotic energies. Hence we have three different asymptotes namely the He(2^3S_1)+He($2^3P_{0,1,2}$) asymptotes where the total electronic angular momentum for each atom is indicated with a subscript on the term symbol. For the He(2^3S_1)+He(2^3P_0) system with atom a in the 2^3S_1 state and atom b in the 2^3P_0 state the multiplicity with $j_a = 1$ and $j_b = 0$ is $(2j_a + 1)(2j_b + 1) = 3$. Clearly, the same holds when atom a is in the 2^3P_0 state and atom b is in the 2^3S_1 state. In total we have 2x3=6 states connecting to the He(2^3S_1)+He(2^3P_0) asymptote. The same can be done for the He(2^3S_1)+He(2^3P_1) and the He(2^3S_1)+He(2^3P_2) asymptotes and this yields 18 and 30 states, respectively.

4.5 Molecular potential energies

The interaction Hamiltonian, which includes the most important interactions between two helium atoms is given by

$$H^{int} = H^{BO} + H^{fs} + H^{l} \,, \tag{4.19}$$

where H^{BO} is the electrostatic (Born-Oppenheimer) interaction potential, H^{fs} is the fine structure interaction and H^{l} is the rotational interaction. In the rest of this chapter atomic units will be used.

4.5.1 The Born-Oppenheimer interaction potential

For the calculation of the Born-Oppenheimer potentials we assume that the two $1s$ electrons do not contribute to the interaction between the two atoms, since they are in the innermost shell and can not easily be polarized. The Born-Oppenheimer

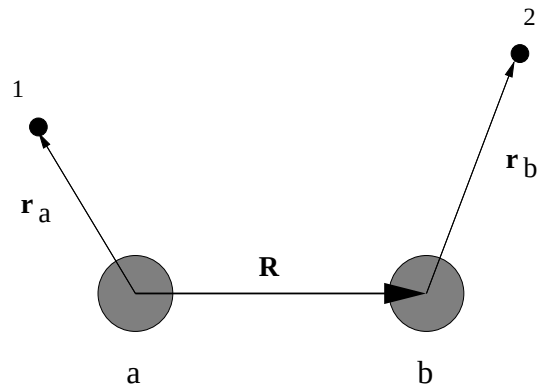

Figure 4.2 Schematic picture of a diatomic molecule with two electrons. The vector R is the internuclear displacement. The vector $\mathbf{r}_a$ is the position vector of electron 1 with respect to nucleus a and $\mathbf{r}_b$ is the position vector of electron 2 with respect to nucleus b.

interaction potential is then given by

$$H^{BO} = \frac{1}{|\mathbf{R}|} + \frac{1}{|\mathbf{R} + \mathbf{r}_b - \mathbf{r}_a|} - \frac{1}{|\mathbf{R} + \mathbf{r}_b|} - \frac{1}{|\mathbf{R} - \mathbf{r}_a|} \,. \tag{4.20}$$

Here $\mathbf{R}$ is a vector from nucleus a to b, $\mathbf{r}_a$ is the position of electron 1 with respect to nucleus a and $\mathbf{r}_b$ is the position of electron 2 with respect to nucleus b. A schematic picture of the molecule is shown in figure 4.2. The first two terms in equation 4.20 represent the Coulomb repulsions between the two nuclei and the two electrons, respectively. The third term is the Coulomb attraction between nucleus a and the electron at nucleus b and the last term is the Coulomb attraction between nucleus b and the electron at nucleus a. The interaction potential in equation 4.20 can be expanded in a Taylor series [32] and the lowest order term is the dipole-dipole interaction, V^{d-d}, which is given by

$$V^{d-d}(R) = \frac{(\mathbf{r}_a \cdot \mathbf{r}_b) - 3(\mathbf{r}_a \cdot \hat{\mathbf{z}})(\mathbf{r}_b \cdot \hat{\mathbf{z}})}{R^3} \,, \tag{4.21}$$

with $\hat{\mathbf{z}} = \mathbf{R}/R$ the unit vector along the internuclear axis. The potential represents the interaction energy of two dipoles $\mathbf{d}_a = -\mathbf{r}_a$ and $\mathbf{d}_b = -\mathbf{r}_b$ located at $z = 0$ and $z = R$, respectively.

The He(2^3S)+ He(2^3S) electrostatic potentials are not of much interest for the photoassociation process, since the potentials are essentially flat at the internuclear distances where photoassociation takes place. It can be shown that the expectation value of V^{d-d} in equation 4.21 is zero, when wave functions as in equation 4.16 are used with the $1s2s$ state for both m and n. The lowest order interaction, which becomes non-zero, is the second order dipole-dipole interaction, which means that the interaction becomes

$$V^{SS}(R) = -C_6/R^6 \; . \tag{4.22}$$

This interaction is called the van der Waals interaction. At large internuclear distances the interaction energy is very small. The C_6 dispersion coefficient has been calculated accurately [20].

The He(2^3S)+ He(2^3P) electrostatic potentials are important in the photoassociation process. The expectation value of equation 4.21 is non-zero when wave functions as in equation 4.16 are used, with $m = 1s2s$ and $n = 1s2p$ and vice versa. Using $\pi_a\pi_b = -1$ and equations 4.16 and 4.21 one can show [33] that

$$V^{SP}(R) = (-1)^{S+\sigma+1}V_\Lambda(R) \; , \tag{4.23}$$

where

$$\begin{aligned} V_\Lambda(R) &= \langle\psi^a_{2s}(1)\psi^b_{2p\Lambda}(2)|V^{d-d}(R)|\psi^a_{2p\Lambda}(1)\psi^b_{2s}(2)\rangle \\ &= \begin{cases} C_3/3R^3 & \text{if } \Lambda = \pm 1 \\ -2C_3/3R^3 & \text{if } \Lambda = 0 \end{cases} \end{aligned} \tag{4.24}$$

with $C_3 = d^2$ and $d = \langle\psi_{2s}|r|\psi_{2p}\rangle$ the transition dipole moment for the $2s \rightarrow 2p$ transition in helium. From equations 4.23 and 4.24 it can be verified that the $^1\Sigma^+_g$, $^3\Sigma^+_u$, $^5\Sigma^+_g$, $^1\Pi_u$, $^3\Pi_g$ and $^5\Pi_u$ potentials are repulsive at short internuclear distances and the $^1\Sigma^+_u$, $^3\Sigma^+_g$, $^5\Sigma^+_u$, $^1\Pi_g$, $^3\Pi_u$ and $^5\Pi_g$ potentials are attractive. The dispersion coefficient C_3 is related to the spontaneous decay rate Γ by [2]

$$\Gamma = \frac{4\omega^3 C_3}{9c^3} \; , \tag{4.25}$$

where ω is the transition frequency. The dispersion coefficient is given by Venturi *et al.* [52] and has the value 19.2307 a.u. From equation 4.25 we find that the spontaneous decay rate is 1.626 MHz.

4.5.2 The fine structure interaction

At large internuclear distances ($> 500\ a_0$) the fine structure interaction within the atoms is more dominant than the electrostatic interaction. The fine structure interaction for metastable rare gases is much more complicated than for e.g. the alkalis, because for the metastable rare gases the core is not closed and for the alkalis it is. For helium the fine structure splittings do not satisfy the Landé intervals. The most dominant fine structure interactions are given by

$$H^{fs} = H^{SO} + H^{SS} + H^{SOO} \ . \tag{4.26}$$

In equation 4.26 the first term is the spin-orbit interaction, the second term is the spin-spin interaction and the last term is the spin-other orbit interaction [32].

The spin-orbit interaction is given by

$$H^{SO} = \sum_i \xi(r_i)\ \mathbf{l}_i \cdot \mathbf{s}_i \ , \tag{4.27}$$

where the summation runs over all four electrons in the two atoms, but only the $2p$ electron contributes. Note, that here $\mathbf{l}_i$ and $\mathbf{s}_i$ are single electron angular momenta instead of the two electron angular momenta defined in section 4.2.1. The quantity $\xi(r_i)$ is defined as

$$\xi(r_i) = \frac{1}{2r_i}\frac{dV}{dr_i} \tag{4.28}$$

in atomic units and $V(r_i)$ represents the Coulomb interaction between the electron and the nucleus. The spin-spin interaction is given by

$$H^{SS} = 2\alpha^2 \sum_{i<j} \left[\frac{\mathbf{s}_i \cdot \mathbf{s}_j}{r_{ij}^3} - 3\frac{(\mathbf{s}_i \cdot \mathbf{r}_{ij})(\mathbf{s}_j \cdot \mathbf{r}_{ij})}{r_{ij}^5} \right] \ , \tag{4.29}$$

where α is the fine structure constant and r_{ij} is the distance between two electrons. The summation is over all pairs of electrons, but it is clear that the spin-spin interaction between two electrons of one atom is the dominant interaction. For helium this interaction is larger than the spin-orbit term. The spin-other orbit interaction,

$$H^{SOO} = \sum_{i<j} \xi'(r_{ij})\ \mathbf{l}_i \cdot \mathbf{s}_j \ , \tag{4.30}$$

is the interaction between the orbital angular momentum of one electron with the spin angular momentum of another electron. The $2p$ electron is the only electron with non-zero orbital angular momentum, so the summation in equation 4.30

reduces to one term. The quantity $\xi'(r_{ij})$ is given by equation 4.28 with V the Coulomb repulsion of the two electrons instead of the Coulomb attraction between an electron and a nucleus. For helium this interaction inverts the 2^3P multiplet. This means for the energy E of each state that $E(2^3\mathrm{P}_0) > E(2^3\mathrm{P}_1) > E(2^3\mathrm{P}_2)$.

The total fine structure interaction of equation 4.26 yields the following fine structure splittings [34, 35]:

$$\begin{aligned} \Delta_1 &= 2.291 \text{ GHz} \qquad \text{between } 2^3\mathrm{P}_2 \text{ and } 2^3\mathrm{P}_1 \\ \Delta_0 &= \Delta_1 + 29.617 \text{ GHz} \text{ between } 2^3\mathrm{P}_2 \text{ and } 2^3\mathrm{P}_0 \,. \end{aligned} \tag{4.31}$$

The molecular potentials including fine structure can be calculated by using the fine structure splittings. In the basis set $|j_a m_a^j; j_b m_b^j\rangle$ the matrix elements $\langle H^{BO} + H^{fs}\rangle$ become

$$\begin{aligned} \langle H^{BO} + H^{fs}\rangle &= \langle j_a' \; m_a' \; ; j_b' \; m_b' | H^{BO} | j_a \; m_a \; ; j_b \; m_b\rangle + \\ & \quad \Delta_{j_b} \; \delta_{j_b' j_b} \delta_{m_b' m_b} \delta_{j_a' j_a} \delta_{m_a' m_a} \,, \end{aligned} \tag{4.32}$$

where we assumed that the $2p$ electron is at nucleus b. The $2^3\mathrm{P}_2$ energy is set to zero and $\Delta_{0,1}$ are given by equation 4.31. The first term on the right hand side of equation 4.32 can be evaluated in the basis set $|l_a m_a^l \; ; s_a m_a^s\rangle |l_b m_b^l \; ; s_b m_b^s\rangle$ by using equations 4.18 and 4.20. In this way the fine structure interaction of equation 4.26 is taken into account in an exact way. The matrix given by equation 4.32 is diagonalized at each internuclear distance and the eigenenergies connected to the He($2^3\mathrm{S}_1$)+He($2^3\mathrm{P}_2$) asymptote are shown in figure 4.3.

4.5.3 The rotational interaction

The rotational interaction is given by

$$H^l = \frac{1}{2\mu R^2} \mathbf{l}^2 \,, \tag{4.33}$$

where $\mathbf{l}$ is the rotational angular momentum introduced in section 4.2.1, μ is the reduced mass of the two atoms and R is the internuclear distance. As shown in section 4.2.1 $\mathbf{l}$ can be written as $\mathbf{l} = \mathbf{J} - \mathbf{j}$ or $\mathbf{l} = \mathbf{J} - \mathbf{L} - \mathbf{S}$ and the rotational Hamiltonian of equation 4.33 becomes

$$H^l = \frac{1}{2\mu R^2} \left(\mathbf{J}^2 + \mathbf{j}^2 - J_+ j_- - J_- j_+ - 2 J_z j_z \right) \tag{4.34}$$

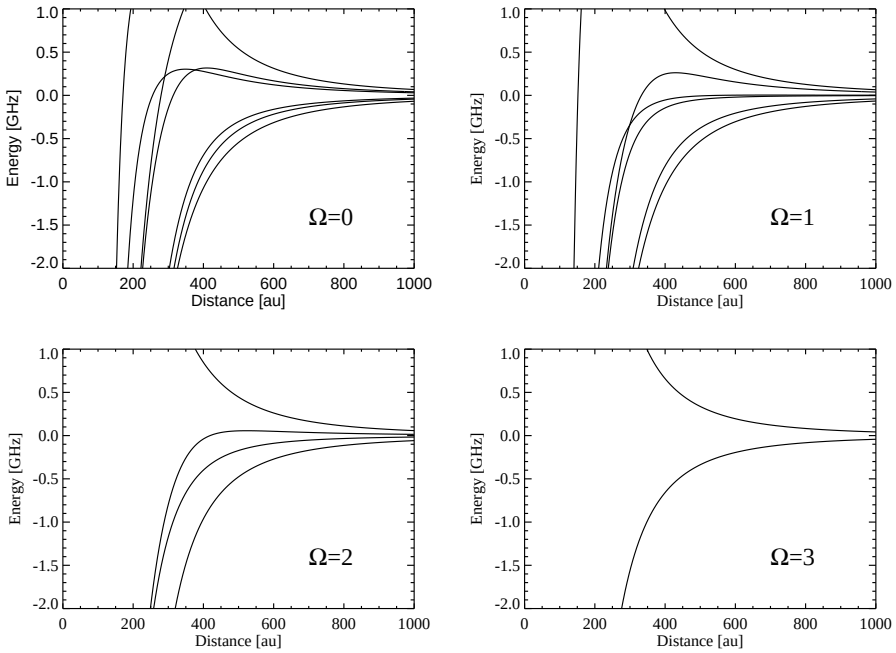

Figure 4.3 Hund's case (c) potentials connecting to the He(2^3S_1)+He(2^3P_2) asymptote. The four figures show the potentials for the four different Ω values. The distances are in atomic units.

or

$$H^l = \frac{1}{2\mu R^2}\{(\mathbf{J}^2 - J_z^2) + (\mathbf{L}^2 - L_z^2) + (\mathbf{S}^2 - S_z^2) + (L_+S_- - L_-S_+) - (J_+L_- - J_-L_+) - (J_+S_- - J_-S_+)\} \ . \quad (4.35)$$

The last two terms of equation 4.35 couple the rotational and the electronic degrees of freedom. These terms are called the Coriolis coupling terms.

It should be noted that the molecule-fixed components of the total angular momentum obey *anomalous* commutation relations [28]. If the normal commutation rules are to hold the $J_\pm$ operators can be redefined as $J_\mp$. If the basis states are $|jM^j; JM^J\rangle$ with M^j and M^J the projections of **j** and **J** on the molecular axis respectively (see section 4.2.1), the matrix elements of $\mathbf{l}^2$ (see equation 4.34) are

given by

$$\begin{aligned}\langle\, \mathbf{l}^2 \,\rangle = &\left(J(J+1)+j(j+1)-2\Omega^2\right)\delta_{M^{j\prime}M^j}\delta_{M^{J\prime}M^J} - \\ &\sqrt{J(J+1)-M^jM^{j\prime}}\sqrt{j(j+1)-M^JM^{J\prime}}\delta_{M^{j\prime}M^j-1}\delta_{M^{J\prime}M^J-1} - \\ &\sqrt{J(J+1)-M^jM^{j\prime}}\sqrt{j(j+1)-M^JM^{J\prime}}\delta_{M^{j\prime}M^j+1}\delta_{M^{J\prime}M^J+1}\ ,\end{aligned} \tag{4.36}$$

where we used $\Omega = |M^j|$ and $M^j = M^J$, since the projection of $\mathbf{l}$ on the molecular axis is always zero. It is clear that rotation couples molecular states with different Ω. This can cause avoided crossings in the adiabatic potentials between states with different Ω.

It can be seen that $M^{j\prime} = M^{J\prime}$, which would not have been the case if $J_\pm$ was not replaced by $J_\mp$. In a first approximation we set j (and therefore Ω) equal to zero and the rotational Hamiltonian becomes diagonal with rotational energies

$$E^{rot} = \frac{1}{2\mu R^2}J(J+1)\ . \tag{4.37}$$

A second approximation can be made by neglecting the last two terms in equation 4.36 and the rotational Hamiltonian is again diagonal with rotational energies

$$E^{rot} = \frac{1}{2\mu R^2}\left(J(J+1)+j(j+1)-2\Omega^2\right)\ . \tag{4.38}$$

In our calculations the basis set is composed of the angular momenta of the separate atoms (j_a, j_b, m_a^j and m_b^j), so j is not a good quantum number. The projection on the molecular axis $m_a^j + m_b^j$ is still conserved. Even though j is not a good quantum number the expectation value of $\mathbf{j}^2$ can be evaluated in this basis set. In figure 4.4 the potentials for the 0_u^- state connected to the He(2^3S_1)+ He(2^3P_1) are shown for the first and second approximation for J values ranging from 0 to 3. The potential curve without rotation is also shown but coincides with the first approximation for $J = 0$. For states with $\Omega \neq 0$ the allowed values for J are given by the restriction that J always has to be larger than one of its components so $J \geq \Omega$. For states with $\Omega = 0$ selection rules can be derived using the fact that the ^{4}He nuclei are bosons. Hougen [29] showed that the permutation P of the two nuclei in the space-fixed frame is equal to the rotation of the electronic coordinates in the molecular wave function. This operation is denoted by $C_2^e(y)$ where the subscript e indicates that only electronic coordinates are transformed.

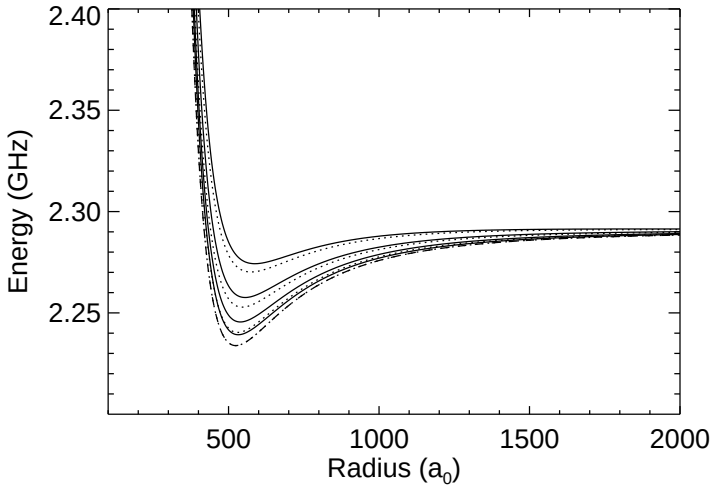

Figure 4.4 Rotational potential curves for the 0_u^- long range state connected to the He(2^3S_1)+He(2^3P_1) asymptote. The dotted curves are the potentials in the first approximation and the solid curves are the potentials in the second approximation where $J = 0, 1, 2, 3$ from bottom to top. The lowest curve is the first approximation for $J = 0$ coinciding with a dashed curve which represents the potential without rotation.

This is a different operator than the rotation of all coordinates (nuclei included), $C_2(y)$, mentioned in section 4.2.3. Since $C_2^e(y) = i_e\sigma_v(xz)$ we have

$$P|\psi_{total}(\Omega = 0\ J)\rangle = (-1)^{\sigma+s+J}|\psi_{total}(\Omega = 0\ J)\rangle\ . \tag{4.39}$$

where $|\psi_{total}(\Omega = 0\ J)\rangle$ is the total wave function including the nuclei and $s = 1$ for 0^- states and $s = 0$ for all other states (s should not be confused with the spin quantum number). The factor on the right hand side of equation 4.39 must be 1, so $\sigma + s + J$ must be even.

Furthermore, since the two He(2^3S) atoms are bosons, it can be shown that for gerade symmetries only even partial waves and for ungerade symmetries only odd partial waves contribute to the He(2^3S)+He(2^3S) collisions. The wave function for a free state (the energy of the state is higher than the dissociation limit) can be expanded in partial waves. If $|\psi_{mol}\rangle$ is the properly symmetrized part of the

wave function depending on the molecular quantum numbers, the scattering wave function $|\psi_{scat}\rangle$ can be written as

$$|\psi_{scat}\rangle = \sum_{lm_l} |\psi_{mol}\rangle |(k)lm_l\rangle Y^*_{lm_l}(\hat{\mathbf{k}}) \ , \tag{4.40}$$

where l is the nuclear rotational quantum number and m_l is the projection of l on the space-fixed axis. The wave vector $\mathbf{k}$ indicates the direction and magnitude of the relative motion of the two atoms.

The permutation of the two atoms is equal to the exchange of the two electron pairs followed by the exchange of the two nuclei. The exchange of the two electron pairs yields a factor $+1$, since an electron pair is a boson. The exchange of the nuclei is equal to the inversion of the nuclei with respect to the center of mass followed by the exchange of the nuclear spins. The last operation yields a factor $+1$, since ^{4}He has zero nuclear spin. Therefore, the permutation of the two atoms is equal to the nuclear inversion i_N. Since $i_N = i_t i_e$ and the parity operator i_t acting on the wave function in equation 4.40 yields $\pi_a \pi_b (-1)^l$ [36], we find that $(-1)^{\sigma+l} = 1$ for He(2^3S)+He(2^3S) collisions. Therefore, for gerade symmetries only even partial waves and for ungerade symmetries only odd partial waves contribute to the collision.

4.6 Molecular dipole transitions

In photoassociation the molecular complex in the ground state is excited to a bound excited state by absorption of a photon. We refer to the ground state by the He(2^3S)+He(2^3S) complex and the excited state by the He(2^3S)+He(2^3P) complex. In the dipole approximation the coupling to the excited state by light is given by the interaction

$$V^{rad} = -E\hat{\mathbf{e}} \cdot (\mathbf{r}_a + \mathbf{r}_b) \ , \tag{4.41}$$

where $E\hat{\mathbf{e}}$ is the electric field vector and $-\mathbf{r}_{a,b}$ is the dipole operator for the electron at nucleus a, b respectively. Since the laser light drives the $2s \rightarrow 2p$ atomic transition, the two $1s$ electrons are not considered here. Denoting $|\psi\rangle$ the ground state wave function and $|\psi'\rangle$ the excited state wave function, the coupling matrix element is $\langle\psi'|V^{rad}|\psi\rangle$. The selection rules given in [37] can be summarized as follows:

$$\begin{aligned} &\Delta J = 0, \pm 1 \ (J = 0 \nrightarrow J' = 0), \ \Delta p = 1, \ \Delta S = 0, \ \Delta\Sigma = 0, \\ &\Delta\Lambda = 0, \pm 1, \ \Delta\Omega = 0, \pm 1 \ , \Delta\sigma = 1, \Delta s = 0 \ . \end{aligned} \tag{4.42}$$

The photon carries one unit of angular momentum and this is coupled to the total angular momentum, which yields $|J-1| \leq J' \leq J+1$. Therefore, the transition $J = 0 \rightarrow J' = 0$ is not allowed. The selection rule $\Delta p = 1$ means that the parity of the wave function changes in a dipole transition. The parity of the wave function is $(-1)^p = \pi_a \pi_b$. Since the dipole operator of equation 4.41 is anti-symmetric, the $\langle \psi' | V^{rad} | \psi \rangle$ matrix elements are non-zero only when $|\psi\rangle$ and $|\psi'\rangle$ have opposite parities.

The other selection rules can be derived by using equations 4.16 and 4.41. For the ground state we have $m = n = 1s2s, 1s2s$ in equation 4.16 and for the excited state we have $m' = 1s2s$ and $n' = 1s2p_\Lambda$ where Λ is the projection of $\mathbf{L}$ on the internuclear axis. The dipole operator does not operate on the spin quantum numbers, so the selection rules $\Delta S = 0$ and $\Delta\Sigma = 0$ are readily found. The product $\hat{\mathbf{e}} \cdot \mathbf{r}_a$ can be evaluated in spherical components [32] which gives

$$\hat{\mathbf{e}} \cdot \mathbf{r}_a = \left(\frac{4\pi}{3}\right)^{1/2} r_a \sum_{q=0,\pm 1} e_q Y_{1,q}(\theta_a, \phi_a) \,, \tag{4.43}$$

where $Y_{1,q}(\theta_a, \phi_a)$ are the spherical harmonics with $l = 1$ and $m = q$. In equation 4.43 $e_{\pm 1}$ are the two circular components of the polarization vector and e_0 is the component of the polarization vector parallel to the internuclear axis. For the electron at nucleus b a similar expression as equation 4.43 can be made. Using the properties of the spherical harmonics the angular part of $\langle \psi' | V^{rad} | \psi \rangle$ yields the selection rule $\Delta\Lambda = 0, \pm 1$. This result, together with the selection rule $\Delta\Sigma = 0$, yields the selection rule $\Delta\Omega = 0, \pm 1$.

Evaluating the radial part of $\langle \psi' | V^{rad} | \psi \rangle$ for the electron at nucleus a and using equations 4.16 and 4.41 yields

$$\langle \psi' | r_a | \psi \rangle = \frac{d}{2\sqrt{2}} \left[(-1)^{S+S'} + \pi'_a \pi'_b (-1)^{\sigma'+S'} \right] \,, \tag{4.44}$$

with $d = \langle \psi_{2s} | r | \psi_{2p} \rangle$ the transition dipole moment for the $2s \rightarrow 2p$ transition in helium. It should be noted, that the wave functions in equation 4.16 needed to be normalized before they were substituted into equation 4.44. If we perform the same operation for the electron at nucleus b, we find that

$$\langle \psi' | r_b | \psi \rangle = \frac{d}{2\sqrt{2}} \left[1 + \pi'_a \pi'_b (-1)^{\sigma'+S} \right] \,, \tag{4.45}$$

If we use that $S = S'$ and $\pi_a \pi_b (-1)^{\sigma+S} = 1$ for the ground state (see equation

4.16), we have

$$\langle \psi' | r_a + r_b | \psi \rangle = \frac{d}{\sqrt{2}} \left[1 + (-1)^{\Delta p + \Delta \sigma} \right] \ , \tag{4.46}$$

with Δp the change in parity. Since the parity changes sign in a dipole transition, the inversion symmetry (denoted by $(-1)^\sigma$) must change sign, which means that only transitions between gerade and ungerade states are allowed. From equation 4.46 it can be seen that the maximum molecular dipole moment is $\sqrt{2}$ times the atomic dipole moment.

Finally, since the reflection symmetry of the states in equation 4.16 is given by $\pi_a \pi_b (-1)^{l_a + l_b}$ (see section 4.2.3), the reflection symmetry does not change in the dipole transition, which means $\Delta s = 0$. This can be seen from the fact that both the parity $\pi_a \pi_b$ and the factor $(-1)^{l_a + l_b}$ change sign in a dipole transition.

Chapter 5

Photoassociation spectroscopy of He(2^3S_1)+He(2^3P_2)

5.1 Introduction

Photoassociation spectroscopy (PAS) of cold atoms can be used to determine long range potentials between two atoms with high precision, since the initial kinetic energy of the collision partners is very low. The radiative lifetime of the excited state can be determined from the information on the excited state potential [6, 7] and the s wave scattering length can be determined from intensity profiles of photoassociation resonances [8]. Photoassociation spectroscopy has been applied to several alkali metal elements [38–40]. For the metastable rare gases only results for helium have been reported [41, 43].

In section 5.2 the mechanism and the different detection methods are explained. In section 5.3 the experiments performed around the 2^3S_1-2^3P_2 asymptote are discussed. In section 5.4 the accumulated phase analysis is applied to the trap loss measurements performed at ENS in Paris and to our ionization measurements. In section 5.5 the line profiles of the PAS resonances are analyzed and in section 5.6 we give our conclusions.

5.2 The PAS mechanism

The mechanism of PAS is schematically shown in figure 5.1. Two free He(2^3S_1) atoms approach each other at long range and the relative kinetic energy distribution has a width ΔE corresponding to the temperature of the atoms in the MOT. Laser light with a detuning Δ from the atomic resonance $2^3S_1 \rightarrow 2^3P_2$ is resonant

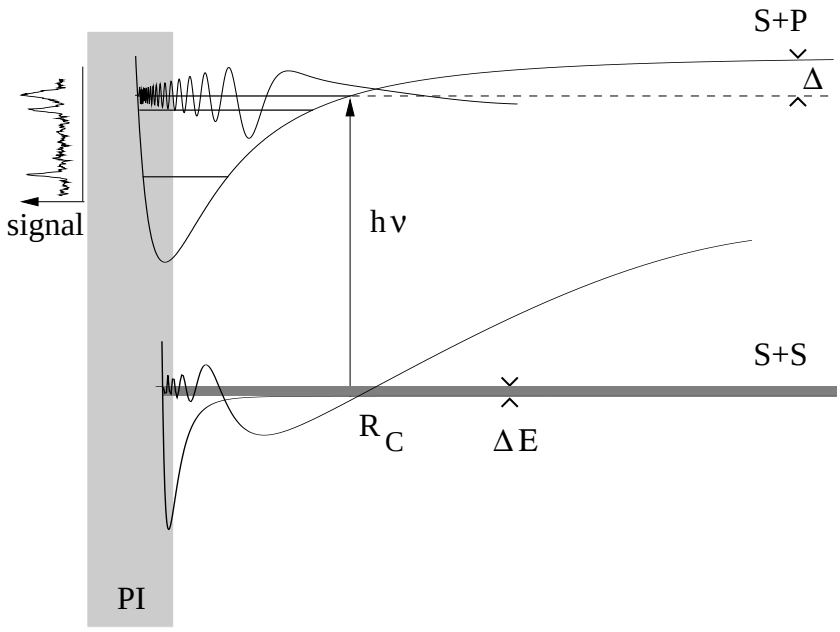

Figure 5.1 Schematic picture of the PAS process. The ground state potential is denoted with S+S and the excited state potential with S+P. The initial kinetic energy spread ΔE is represented by the dark shaded area. The light shaded area indicates the internuclear distances at which Penning ionization (PI) may occur. The detuning Δ from atomic resonance dictates the Condon radius R_C at which the system can be excited to the S+P potential by absorption of a photon with energy $h\nu$. A typical ground state wave function and an excited state wave function are shown. The peaks in the ion spectrum on the left coincides with the vibrational levels shown.

with the collision system at an internuclear distance R_C (the Condon radius) and the atoms can be excited from the S+S potential, which is considered the ground state, to the S+P potential.

The system can be either resonantly excited to a bound state (ro-vibrational level in the excited state potential) or off-resonantly, which is called an optical collision. At small internuclear distances the system can ionize due to Penning ionization (PI) depending on the total spin. In the singlet and triplet states the

collision system ionizes with a high probability (> 80 %), whereas in the quintet state ionization is forbidden due to spin conservation rules. In optical collisions the amplitude of the wave function is reduced at short range because of PI and the outgoing wave function is not interfering destructively with the incoming wave function. Even though optical collisions are not resonant excitations, there is considerable overlap between the ground state wave function and the excited state wave function. If the probe laser frequency is scanned from below atomic resonance towards atomic resonance, the Condon radius moves to larger internuclear distances and more partial waves contribute to the collision. This means that more atoms are accelerated towards each other and ionize at short internuclear distance. Therefore the background ionization signal increases when the laser frequency is scanned from below atomic resonance towards atomic resonance.

The PAS resonances can be detected in different ways. In our experiments the detection of ions is used. Ion detection has been applied to several alkali metal systems but the ionization mechanism is very different from the ionization mechanism in metastable rare gases. The metastable rare gases can ionize in the ground state and the singly-excited state through PI. In alkali metal systems the quasi-molecule is either excited to a doubly-excited state (P+P potential) by absorption of two photons and auto-ionizes at short internuclear distances or is directly photo-ionized from the singly-excited state (S+P potential) by absorption of a photon of sufficient energy at short internuclear distances. The disadvantage of measuring ions for metastable rare gases in a MOT is the huge background signal induced by the trapping laser. This is circumvented in our experiments by switching the trap on and off and only measuring the ions in the trap-off period. The trap-off period should be short enough, so that the atoms in the MOT do not fly apart.

A second detection method is measuring the fluorescence of the MOT as a function of the probe laser frequency. When the collision system is excited to a ro-vibrational state, the atoms are accelerated towards each other and can ionize at short internuclear distances or the molecule can decay to the ground state by spontaneous emission of a photon. In PI, which is only present in metastable rare gas elements, none of the products (He($^1S_0$), He^+ or He_2^+) is contained in the MOT. Spontaneous emission occurs for both alkali metals and metastable rare gas elements. The molecule decays to the S+S potential, whereby the atoms keep the kinetic energy gained in the excited state according to the Franck-Condon principle. If the kinetic energy is higher than the trap depth, the atoms are lost from the trap. This mechanism is called radiative escape (RE) [42]. Both PI

and RE lead to trap loss and this can be observed by a decrease in the MOT fluorescence. Especially for alkali metal elements the ionization measurements are favorable over trap loss measurements due to the absence of a background signal which provides a very good signal to noise ratio.

In the Leduc group at ENS in Paris photoassociation is studied in a magnetic trap at temperatures just above the transition to Bose-Einstein condensation (typically 5 μK) [43]. Since a particle detector is not installed in their setup and atoms trapped in a magnetic trap do not fluoresce, they apply absorption imaging of the trapped cloud. The probe laser illuminates the cloud for a few ms and after this period the cloud is released and imaged onto a CCD camera using destructive absorption imaging. The number of atoms in the trap, the density and the temperature are derived from these measurements. For each different frequency of the probe laser pulse the magnetic trap has to be loaded and imaged, which takes tens of seconds, so this is a very time consuming experiment. The advantage of measurements in a magnetic trap at these temperatures is the extremely narrow widths of the PAS resonances. These widths are only determined by ionization, the probe laser linewidth and the molecular linewidths. In our case the widths of the PAS resonances are primarily determined by ionization and the temperature of the MOT cloud.

5.3 Measurements around the $2^3\mathbf{S}_1$-$2^3\mathbf{P}_2$ asymptote

This section deals with the PAS experiments performed around the 2^3S_1-2^3P_2 asymptote. In section 5.3.1 the experiments are discussed, and in section 5.3.2 the results are shown. In section 5.3.3 the frequency calibration is discussed and in section 5.4 the analysis is done.

5.3.1 Experiments

The experiments are performed in a MOT containing about 10^5 atoms at a temperature of 1.9 mK. The trap is loaded from a DC discharge source cooled with liquid helium. The slowing laser beam is counter-propagating the atomic beam and the atoms are slowed down from an average velocity of about 300 m/s to a velocity below the capture velocity of the MOT. The required Zeeman shift during the slowing process is provided by the MOT magnetic field. Both the slowing laser and the trapping laser are locked just below the $2^3S_1 \rightarrow 2^3P_2$ atomic transition using saturated absorption spectroscopy as described in section 3.3. The

slowing laser and the trapping laser operate at a detuning of -54 MHz and -14 MHz, respectively.

The probe laser setup is shown in figure 3.6 in chapter 3. The probe laser frequency is scanned from below to above the $2^3S_1 \rightarrow 2^3P_2$ atomic transition within a period of typically 100 s. The maximum frequency range that can be covered is about 25 GHz. The lens in figure 3.6 is actually a telescope consisting of two lenses with focal lengths of +300 mm. The intensity of the probe laser can be varied by changing the distance between the two lenses or by rotating a $\lambda/2$ plate in front of a polarizing beam splitter cube, thereby changing the intensity of the transmitted laser beam. Part of the probe laser beam is going through a Fabry-Pérot interferometer (FPI) and the FPI peaks are used for the relative frequency calibration. Another part of the probe laser beam passes through an RF discharge cell and the Lamb dip is used for the absolute frequency calibration.

The MOT laser frequency is periodically switched from the trapping frequency to 350 MHz below the atomic resonance at a rate of 25 kHz, which means that the period that the laser is far detuned (trap-off period) is 20 μs. The period that the laser is at trapping frequency (trap-on period) is also 20 μs. The trap-off period is much shorter than one ms, which is the time scale on which the expansion of the MOT is considerable. On the other hand, it is much longer than the radiative lifetime of the He(2^3P) state (98 ns) in order to make sure that all the He(2^3P) atoms decayed to the He(2^3S) state. This reduces the background ionization signal induced by the MOT laser, since the ionization rate for the S+P system is two orders of magnitude larger than the ionization rate for the S+S system. Consequently, this increases the signal to noise ratio. With this modulation the MOT laser is still locked using saturated absorption spectroscopy. The probe is either on continuously or can be switched with an acousto-optical modulator (AOM). In the latter case the first order Bragg reflection is used as the probe laser beam and is shifted +80 MHz in frequency. When the AOM is used the probe laser is off during the trap-on period and the MOT cloud is not disturbed significantly by the probe laser beam.

5.3.2 Results

A measurement of the ion rate as a function of the probe laser frequency is shown in figure 5.2. The probe laser beam is focused with the telescope and the saturation parameter is a few times 10^4. The ion rate is recorded simultaneously with the FPI signal and the signal of the saturation spectroscopy setup. The position of the Lamb dip defines atomic resonance. For figure 5.2 twenty spectra are measured,

shifted according to the Lamb dip positions and averaged to increase the signal to noise ratio. The ion spectrum shown in figure 5.2 has the smallest signal to noise ratio we have ever measured. Usually the signal to noise ratio we measured is significantly larger. This varies from day to day and depends on the MOT alignment, vibrations in the setup and the temperature in the lab.

In figure 5.2 several peaks can be observed, which can be identified as vibrational states in the excited state potentials. Far below atomic resonance (in this case more than 4 GHz, but the detuning range depends on the probe laser intensity) the background ion signal consists of ions created in S+S collisions, but also in S+P collisions, since in the trap-off period the MOT laser is detuned only 350 MHz below atomic resonance and still induces S+P collisions. When the probe laser is closer to resonance (a detuning of -4 GHz to -1 GHz) the background ionization signal increases. This is attributed to optical collisions induced by the probe laser. The mechanism of optical collisions is described in section 5.2. Even closer to resonance (a detuning of -1 GHz to 0 GHz) the radiation force caused by the probe laser begins to remove atoms from the MOT and eventually completely empties it. As can be seen from equation 2.1, the detuning range over which the probe laser causes trap loss induced by the radiation force depends on the intensity of the probe laser beam. In order to observe PAS resonances close to the atomic resonance the probe laser intensity is reduced. In figure 5.3 a long range scan with high probe laser intensity and a short range scan with low probe laser intensity are shown.

5.3.3 Frequency calibration

One important aspect in the analysis of photoassociation spectra is the calibration of the frequency scale. We use a near-confocal FPI for the relative frequency scale and a saturation spectroscopy setup to determine the atomic resonance. The FPI is home-built and the resonator is not perfectly confocal. The distance between the mirrors, d, and the radii of curvature of the mirrors, R_i with $i = 1, 2$, are approximately 75 mm. The mode frequencies in a Fabry-Pérot interferometer with $d \neq R_i$ are given by [44]

$$\nu = \frac{c}{2d}\left[q + \frac{1}{\pi}(m + n + 1)\arccos\sqrt{g_1 g_2}\right] , \tag{5.1}$$

where

$$g_i = 1 - \frac{d}{R_i} \qquad \text{with } i = 1, 2 , \tag{5.2}$$

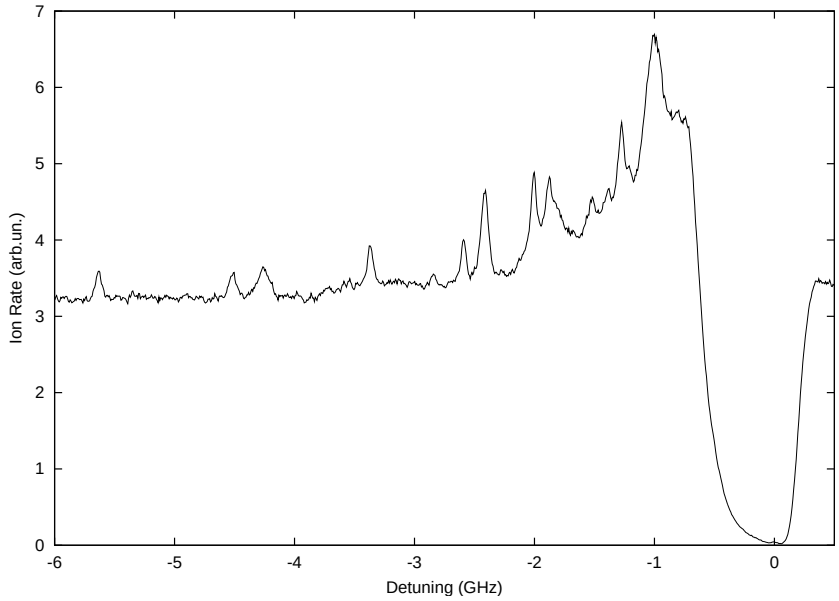

Figure 5.2 Ion spectrum as a function of the probe laser detuning from the $2^3\mathrm{S}_1 \rightarrow 2^3\mathrm{P}_2$ atomic transition. The saturation parameter is a few times 10^4. Clear peaks are observed below resonance, which can be identified as vibrational states in the excited state potentials. The detuning is in GHz and the ion rate in arbitrary units.

and c is the speed of light. The longitudinal modes are given by $q = 1, 2$ etc. and the transverse modes by $m = n = 0, 1, 2$ etc. Even transverse modes are defined as $m + n = 2p$ and odd transverse modes as $m + n = 2p + 1$, where p is an integer. The stability parameters $g_{1,2}$ in equation 5.2 determine whether the resonator is stable, which means that the light ray remains in the resonator even after an infinite number of round trips. The resonator is stable when $0 \leq g_1 g_2 \leq 1$.

For a perfect confocal FPI $d = R_1 = R_2$ and from equation 5.2 we have $g_1 = g_2 = 0$. Then $\arccos\sqrt{g_1 g_2} = \pi/2$ and it can be seen from equation 5.1 that the odd modes are exactly in between the even modes for a perfect confocal FPI. For a near-confocal FPI we have $g_1 g_2 \ll 1$, but not equal to zero. Then $\arccos\sqrt{g_1 g_2} \approx \pi/2$ and the odd modes are almost exactly in between the even modes. In this case the free spectral range (FSR) is defined as the frequency separation between two adjacent longitudinal modes with $m = n = 0$ (modes

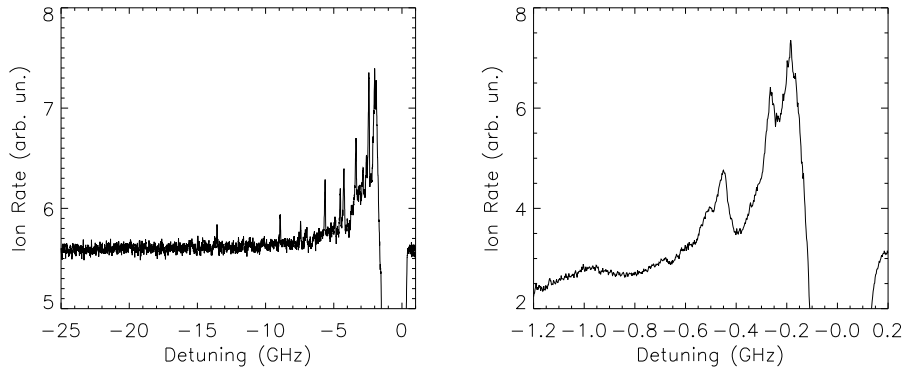

Figure 5.3 Ion spectra as a function of the probe laser detuning from the $2^3S_1 \rightarrow 2^3P_2$ atomic transition. In the left figure the scan is over about 25 GHz and a saturation parameter of $3 \cdot 10^5$ is used. In the right figure the scan is over only about 1 GHz and a saturation parameter of $1 \cdot 10^2$ is used.

with $m = n = 0$ are called TEM_{00} modes). This means that the FSR for our FPI is $c/2d \approx 2$ GHz. It is desirable to have the TEM_{00} mode as the only mode in the resonator, since the modes are evenly spaced with a frequency separation of $c/2d$. This requires beam shaping, because the focus of the laser beam needs to be exactly in the center of the resonator and the wave fronts at the mirrors must be identical to the curvature of the mirrors [44]. This has not been done at the time the measurements were taken, which means that higher order transverse modes are observed in the Fabry-Pérot spectrum.

If Φ is the phase increment after a round trip in a FPI, then the transmitted intensity I_T as a function of Φ is given by

$$I_T = \frac{I_0}{1 + F \sin^2 \Phi/2} \, , \tag{5.3}$$

where I_0 is the intensity of the incoming laser beam and the parameter F is defined as $F = 4R/(1-R)^2$ with R the reflectivity of the mirrors. The phase Φ is related to the laser frequency ν according to $\Phi = 4\pi d\nu/c$, since the optical path of a round trip in a FPI is $2d$ in the approximation that the laser beam enters the FPI

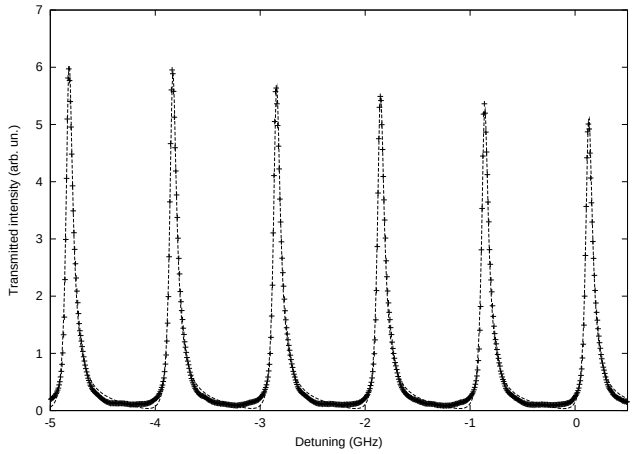

Figure 5.4 Fabry-Pérot signal for a scan over approximately 5 GHz. The plus signs are the measured data and the dashed line is a fit to the data. The detuning is given in GHz with respect to the 2^3S_1-2^3P_2 atomic resonance.

on axis.

The relative frequency scale is determined by fitting to the Fabry-Pérot spectrum two intensity profiles as in equation 5.3 shifted over approximately half the FSR with respect to each other. One of the profiles represents the even modes and the other the odd modes. Since the peaks in the measured intensity spectrum are asymmetric, the profiles as in equation 5.3 are multiplied with a Fourier series to account for the asymmetry. The scan rate of the probe laser frequency is assumed to be almost constant with a small non-linearity coefficient, depending on the linearity of the voltage ramp applied to the laser supply and the scan rate of the laser. Furthermore, the amplitude of the intensity profiles is assumed to be linearly dependent on the laser frequency, which is a reasonable assumption, since the current through the laser diode is varied in order to change the laser frequency and both the laser frequency and laser intensity depend linearly on the current. In figure 5.4 a measured Fabry-Pérot signal is shown together with a fit of the function as described above.

The scan rate is calibrated by using the fine splitting of the 2^3S_1-2^3P_1 and the 2^3S_1-2^3P_2 atomic resonances. A scan over these resonances is made and the scan rate is found from fitting the FPI signal. A fit of the derivative of a Lorentzian

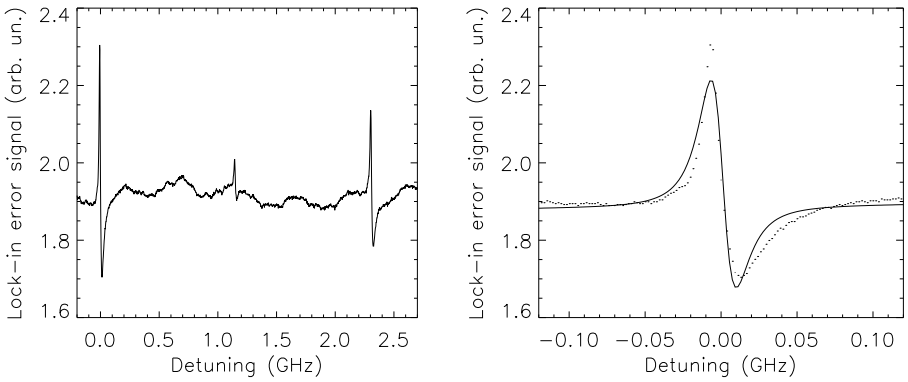

Figure 5.5 The lock-in error signal as a function of the detuning from the 2^3S_1-2^3P_2 atomic resonance. The figure on the left shows both Lamb dips corresponding to the 2^3S_1-2^3P_2 and the 2^3S_1-2^3P_1 atomic resonances. The cross-over peak, which is exactly between the two Lamb dips, is also clearly visible. On the right a fit of the derivative of a Lorentzian is shown.

to the saturation spectroscopy signal yields the frequency positions of the Lamb dips. From this and the fine structure splitting, which is 2.291 GHz (see equation 4.31), the FSR is found to be about 1.98 GHz. Note, that the frequency difference between two peaks in the FPI spectrum is approximately half this value. In figure 5.5 the saturation spectroscopy signal is shown as well as a fit to one of the Lamb dips. Although the fit is not perfect, the atomic resonance can be determined with sub-MHz accuracy. The spectra for each data file are shifted, so that the Lamb dips are all at zero detuning. Finally, the spectra are averaged to improve the signal to noise ratio.

As will be discussed in section 5.5 ionization and thermal broadening are expected to be the dominant line broadening mechanisms. The first mechanism introduces a Lorentzian line profile while the second causes an asymmetric line profile due to the kinetic energy distribution in the ground state. However, the measured line profiles do not have a typical Lorentzian shape or an asymmetric shape. In order to determine the positions of the peaks in the ionization spectra we have fitted Gaussian distributions to the peak profiles. In some cases two or three Gaussian distributions are fitted to peaks, that have shoulders on the sides and

peak no.	$-\Delta$ (GHz)	$-\Delta$ (GHz)	peak no.	$-\Delta$ (GHz)	$-\Delta$ (GHz)
1	13.57 ± 0.07	13.60	21	2.87 ± 0.005	-
2	(11.70 ± 0.10)	-	22	2.60 ± 0.006	2.59
3	(11.10 ± 0.19)	-	23	2.42 ± 0.002	2.42
4	(10.13 ± 0.12)	-	24	(2.28 ± 0.016)	-
5	(9.00 ± 0.16)	-	25	2.01 ± 0.003	2.00
6	8.94 ± 0.03	8.95	26	1.88 ± 0.007	1.88
7	7.44 ± 0.03	7.45	27	(1.83 ± 0.008)	-
8	7.01 ± 0.03	-	28	1.54 ± 0.007	-
9	(6.44 ± 0.06)	-	29	(1.39 ± 0.007)	1.37
10	-	5.90	30	1.28 ± 0.004	1.28
11	5.64 ± 0.006	5.64	31	(1.21 ± 0.019)	1.22
12	(4.92 ± 0.03)	-	32	-	1.07
13	4.53 ± 0.006	4.53	33	0.98 ± 0.007	0.98
14	(4.35 ± 0.03)	-	34	-	0.62
15	4.26 ± 0.005	4.25	35	0.52 ± 0.002	0.51
16	(3.96 ± 0.05)	-	36	0.46 ± 0.002	0.46
17	-	3.57	37	0.27 ± 0.002	0.28
18	(3.49 ± 0.04)	-	38	-	0.24
19	3.38 ± 0.004	3.37	39	0.19 ± 0.003	0.19
20	(3.07 ± 0.08)	-	40	(0.08 ± 0.013)	0.09

Table **5.1** Observed PAS resonances numbered from large detuning to small detuning. The second and fi fth column are the detunings from the 2^3S_1-2^3P_2 asymptote for which PAS resonances are observed in the ionization spectrum. The errors in the measurements are also given. The third and sixth column are the trap loss resonances measured at ENS in Paris. The errors in their data is in the range of 10 to 20 MHz. The resonances that are shown in parentheses have a very low intensity, but have been observed more than once on separate days.

not clearly resolved peaks. In figure 5.6 a Gaussian fit to a peak in the ionization spectrum is shown. Clearly, a Gaussian distribution fits very well to the data. In table 5.1 all the measured PAS resonances in the ionization signal are shown together with the resonances observed in the trap loss measurements performed

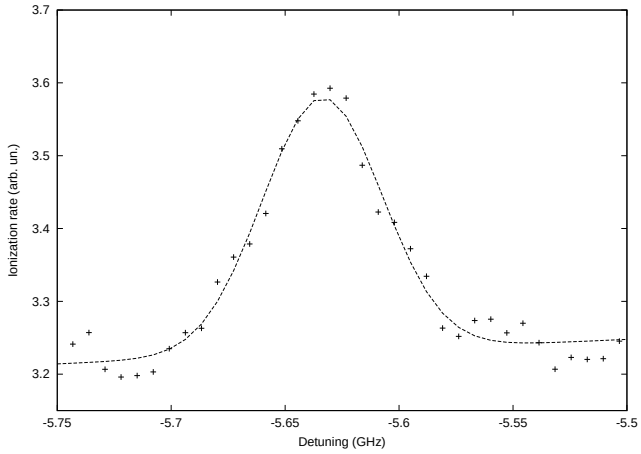

Figure 5.6 Gaussian fit to the PAS resonance at -5.64 GHz from the 2^3S_1- 2^3P_2 asymptote. In the fit the background ionization signal is allowed to be linearly dependent on the detuning.

at ENS in Paris [48]. The peak positions of resonances that are observed at ENS as well as in Utrecht coincide within 30 MHz. Some resonances are observed in Utrecht and not in Paris and vice versa. The trap loss spectra of ENS are not measured continuously over the whole frequency range, since for each data point the magnetic trap has to be reloaded. Measuring a continuous spectrum takes a very long time, so only small frequency ranges where PAS resonances are expected have been studied. For this reason resonances can be missing in the ENS data. Moreover, since the helium atoms are spin polarized in the magnetic trap, the total spin of the ground state is 2 and the corresponding ground state potential is the $^5\Sigma_g^+$ potential. Since dipole transitions can only be made between gerade and ungerade states (see section 4.6), resonances in gerade excited states can not be observed in their measurements. On the contrary, as mentioned in section 5.2 radiative escape can only be observed in trap loss measurements, which can be an explanation for the PAS resonances in the trap loss measurements that are not observed in our ionization data.

5.4 Accumulated phase analysis

There are several techniques to assign a potential to a vibrational series. One of them is the Leroy-Bernstein analysis [45], which assumes a pure R^{-n} potential at large internuclear distances, where n is an integer. In our experiments only high lying vibrational states are probed, which have classical outer turning points at long range. The quasi-molecule spends most of the time at large internuclear distances and therefore the vibrational wave function is almost entirely determined by the long range potential.

If the long range potential is given by

$$V(R) = D - C_3/R^3 \,, \tag{5.4}$$

where D is the dissociation energy, then it is shown in reference [45] that the vibrational levels in this potential have energies E_v given by

$$E_v - D = \frac{1}{C_3^2}\left(\frac{\hbar}{2}\sqrt{\frac{2\pi}{\mu}}\frac{\Gamma(4/3)}{\Gamma(5/6)}(v - v_d)\right)^6 \,, \tag{5.5}$$

where Γ is the Gamma function, v is the vibrational quantum number and v_d is the effective vibrational quantum number at the dissociation limit. The most difficult part of the Leroy-Bernstein analysis in our case is finding the resonances that constitute a vibrational series. Fitting equation 5.5 to the vibrational series should yield a realistic value for C_3. A disadvantage of the Leroy-Bernstein analysis is the assumption that the potential behaves as R^{-n}. This is not the case, since the potentials deviate from this behavior due to fine structure interaction.

Another technique is called the accumulated phase analysis [46], which we will adopt here. This technique is only applicable to higher lying vibrational states, like the Leroy-Bernstein analysis. The Schrödinger equation for a particle with mass μ in a potential $V(R)$ can be written as

$$\left[-\frac{\hbar^2}{2\mu}\frac{d^2}{dR^2} + V(R) + \frac{\hbar^2 l(l+1)}{2\mu R^2}\right] u_l(R) = E u_l(R) \,, \tag{5.6}$$

with R the internuclear distance and $u_l(R) = RF_l(R)$, where $F_l(R)$ is the radial wave function of the lth partial wave. The last term on the left hand side of equation 5.6 is called the centrifugal barrier.

The Schrödinger equation can be numerically integrated inwards from large internuclear distances to a certain internuclear distance $R = R_0$ and outwards

from an internuclear distance smaller than the classical inner turning point to $R = R_0$. For $E < 0$ a bound state can only occur if the phase of the wave function for both integration paths are the same, because for a bound state the phase of the wave function has one value for each internuclear distance. The short range potential is difficult to determine and potentials obtained by quantum chemistry calculations are not accurate enough. The wave function oscillates rapidly in the inner region and the potential has to be known to high precision to determine the correct phase at $R = R_0$. Therefore, the integration outwards is impossible to perform. However, from the experimental data we can choose a PAS resonance and inwards integration from asymptotic internuclear distances yields the phase of the wave function at R_0, if we choose R_0 so that the potential is accurately known for $R > R_0$. In ref. [47] it is shown that for higher lying vibrational states in a potential the phase of the wave function is nearly identical (modulo π) for each state at the same internuclear distance. This means that the other states in the vibrational series can be found by integrating the wave function inwards at all the other measured energies and selecting all the states with approximately the same phase at R_0. This can be done for all the potentials connected to the 2^3S_1-2^3P_2 asymptote that are attractive.

There are 14 attractive potentials connected to the 2^3S_1-2^3P_2 asymptote. There are also three attractive potentials connected to the 2^3S_1-2^3P_1 asymptote, which reach below the 2^3S_1-2^3P_2 asymptote and therefore, the ground state complex can be excited to these potentials in photoassociation experiments below the 2^3S_1-2^3P_2 asymptote. The potentials have been calculated for Hund's case (c) in section 4.5.2 and in table 5.2 the symmetry, the asymptote and the lowest J for each of these 17 attractive potentials are shown. From section 4.5.3 we recall that $J \geq \Omega$ and for $\Omega = 0$ Hund's case (c) states $\sigma + s + J$ has to be even, which means that only even J values contribute to $0_g^+/0_u^-$ states and only odd J values contribute to $0_g^-/0_u^+$ states.

5.4.1 Trap loss analysis

In the analysis of the experiments performed at ENS a great simplification stems from the fact that the atoms are trapped in a purely magnetic trap. In a purely magnetic trap the atoms are spin polarized, which means that the spins are aligned and hence the atoms can only approach each other on the quintet potential $^5\Sigma_g^+$. As mentioned in section 4.6 molecular dipole transitions can only be made from gerade states to ungerade states and vice versa. Therefore, photoassociation can only occur to ungerade excited state potentials in a magnetic trap. This reduces

potential no.	term symbol	asymptote	J_{min}
1	0_g^+	2^3S_1-2^3P_2	0
2	$0_g^-(1)$	2^3S_1-2^3P_2	1
3	$0_g^-(2)$	2^3S_1-2^3P_1	1
4*	$0_u^+(1)$	2^3S_1-2^3P_2	1
5*	$0_u^+(2)$	2^3S_1-2^3P_2	1
6*	$0_u^+(3)$	2^3S_1-2^3P_1	1
7*	0_u^-	2^3S_1-2^3P_2	0
8	$1_g(1)$	2^3S_1-2^3P_2	1
9	$1_g(2)$	2^3S_1-2^3P_2	1
10	$1_g(3)$	2^3S_1-2^3P_2	1
11	$1_g(4)$	2^3S_1-2^3P_1	1
12*	$1_u(1)$	2^3S_1-2^3P_2	1
13*	$1_u(2)$	2^3S_1-2^3P_2	1
14	2_g	2^3S_1-2^3P_2	2
15*	$2_u(1)$	2^3S_1-2^3P_2	2
16*	$2_u(2)$	2^3S_1-2^3P_2	2
17	3_g	2^3S_1-2^3P_2	3

Table **5.2** Potentials that can be reached from the ground state potential in photoassociation experiments below the 2^3S_1-2^3P_2 asymptote. The table shows the Hund's case (c) term symbol, the asymptote and the minimum total angular momentum quantum number. Potentials with identical term symbols have an additional index in parentheses. The potentials marked with a star are the only relevant potentials in the magnetic trap measurements.

the number of potentials that should be included in the analysis to the 8 potentials, indicated by a star in table 5.2.

Furthermore, since the temperature of the atoms in the magnetic trap is of the order of 5 μK, only the $l = 0$ partial wave can contribute for the detunings at which the PAS resonances are found (see table 5.1). Assuming that the ground state potential is flat at long range, the condition for two atoms to reflect from the centrifugal barrier at the Condon point R_C is given by

$$E_k = \frac{\hbar^2 l(l+1)}{2\mu R_C^2} \ , \tag{5.7}$$

where E_k is the kinetic energy of the collision system corresponding to a temperature of 5 μK. For $l = 1$ the excited state is only a few MHz below the dissociation limit at the Condon point. For higher partial waves photoassociation occurs even closer to the dissociation limit. At ENS photoassociation has not been studied this close to the dissociation limit, so only the $l = 0$ partial wave contributes at these temperatures and detuning ranges.

In the magnetic trap experiments the atoms approach each other on the $^5\Sigma_g^+$ potential, which means $j = 2$. The atoms only have spin angular momentum, which means that **j** is in the direction of the magnetic field. Since $l = 0$, the total angular momentum J is also 2. A photon carries one unit of angular momentum, and the photoassociation laser contains all polarization components with respect to the direction of **J** [43], so the ground state complex can be excited to states with $J = 1, 2, 3$. Therefore, the low temperature in the magnetic trap limits the number of rotational states of the excited state.

In Hund's case (c) j is not a good quantum number, which means that states with different j values can be populated in the excited state. In order to find out which rotational states are probed in the experiments, we want to calculate j as a function of the internuclear distance R for each molecular state. The Hamiltonian without rotation is described in the two-atom basis $|j_a m_a^j; j_b m_b^j\rangle$ (see equation 4.32). The molecular eigenstates can be written as

$$|\psi_{mol}\rangle = \sum_i c_i(R)|j_a m_a^j; j_b m_b^j\rangle_i \ , \tag{5.8}$$

where the expansion coefficients $c_i(R)$ depend on R, because the states $|\psi_{mol}\rangle$ are found by diagonalizing the matrix in 4.32, which is also position-dependent. The states $|jM^j\rangle$ are simultaneous eigenstates of the operators $\mathbf{j}^2$ and j_z and can also be expanded in the basis set $|j_a m_a^j; j_b m_b^j\rangle$:

$$|jM^j\rangle = \sum_j d_j|j_a m_a^j; j_b m_b^j\rangle_j \ . \tag{5.9}$$

The expansion coefficients d_j do not depend on position, because the operator $\mathbf{j}^2$ is not position-dependent. The population with a certain j value is found by calculating $|\langle\psi_{mol}|jM^j\rangle|^2$. In figure 5.7 the populations of the j values are shown as a function of internuclear distance for the $0_g^-(1)$ and the $2_u(1)$ potential. Knowing the occupied j values, we can determine whether a molecular eigenstate can be accessed from the ground state by photoassociation. If j is 1 for instance, J is also 1, since $l = 0$. This rotational state is accessible from the $^5\Sigma_g^+$ ground state as shown earlier.

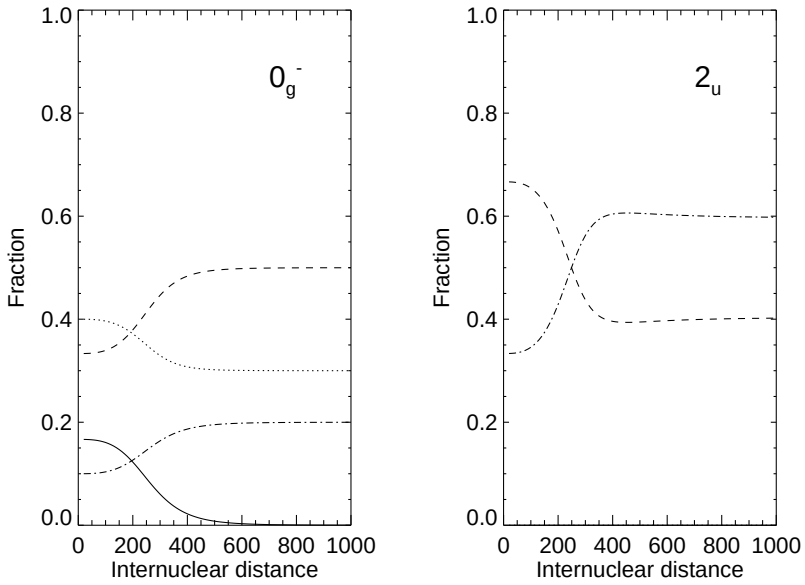

Figure 5.7 Populations of j values as a function of the internuclear distance for the $0_g^-(1)$ potential in the left fi gure and the $2_u(1)$ potential in the right fi gure. The solid line stands for $j = 0$, the dotted line for $j = 1$, the dashed line for $j = 2$ and the dash-dotted line for $j = 3$.

5.4.2 Ionization analysis

In the MOT experiments the atomic spins are randomly oriented and photoassociation can take place from either the $^1\Sigma_g^+$, $^3\Sigma_u^+$ or $^5\Sigma_g^+$ ground state potential. Furthermore, since the temperature in the MOT is 1.9 mK (see section 3.4.2), more partial waves can contribute in the detuning range, where PAS resonances have been observed. For instance, for a $-2C_3/3R^3$ potential (C_3 is defined in section 4.5.1) the $l = 1$ partial wave can contribute for a detuning smaller than 15.7 GHz, the $l = 2$ partial wave for a detuning smaller than 3.0 GHz. Therefore, the total angular momentum for the excited state is not restricted to the values 1,2 and 3.

In the accumulated phase analysis we choose R_0 to be 20 a_0, because the

potentials are accurately calculated from this internuclear distance to asymptotic internuclear distances. As a first step only the strong resonances in the spectra are included in the analysis (the resonances between parentheses in table 5.1 are weak resonances). The phases of the wave functions at R_0 are calculated for each resonance and for each of the potentials in table 5.2. All the resonance energies that yield approximately the same phases are considered to be a vibrational series belonging to one potential. An insightful picture is given by plotting the phase at R_0 for each PAS resonance against the energy. This is done for all the potentials of table 5.2. There are series of resonances for which the phases are nearly constant as a function of energy. This behavior is present only for some of the potentials of table 5.2: potentials 2, 4, 5, 8, 12 and 15. The short range Hund's case (a) projections of these states are all attractive Σ states. According to equations 4.23 and 4.24 these potentials have the same $-2C_3/3R^3$ behavior at intermediate range (internuclear distance between approximately 20 a_0 and a few 100 a_0). This means that no photoassociation to attractive Π states has been observed.

The fact that the attractive Σ potentials are similar at intermediate range complicates the analysis. For each of these potentials the same group of resonances form straight lines, which makes it difficult to attribute one group of resonances to one potential.

If we include the resonances in parentheses from table 5.1 and repeat the analysis, 6 series of resonances can be distinguished and 10 resonances do not fit into any of the series. In figure 5.8 the phases at R_0 are shown as a function of the energy for potential 15. In table 5.3 the series are displayed. In this table v_m is a fictitious vibrational quantum number for the lowest measured vibrational level in each series, because the absolute vibrational quantum number can not be determined unless the short range potential is accurately known. The PAS resonance 30 fits in both series 2 and series 5.

As can be seen from figure 5.8 the phases in each series are slowly varying with energy. This dependence becomes clear if we use the expression for the phase at R_0 in the WKB approximation:

$$\phi = \int_{R_{it}}^{R_0} k(R) dR \,, \tag{5.10}$$

with

$$k(R) = \sqrt{2\mu(E - V(R))/\hbar^2} \,, \tag{5.11}$$

and R_{it} is the classical inner turning point. In the approximation $E \ll |V(R)|$, which is valid sufficiently far away from the classical turning points, the phase

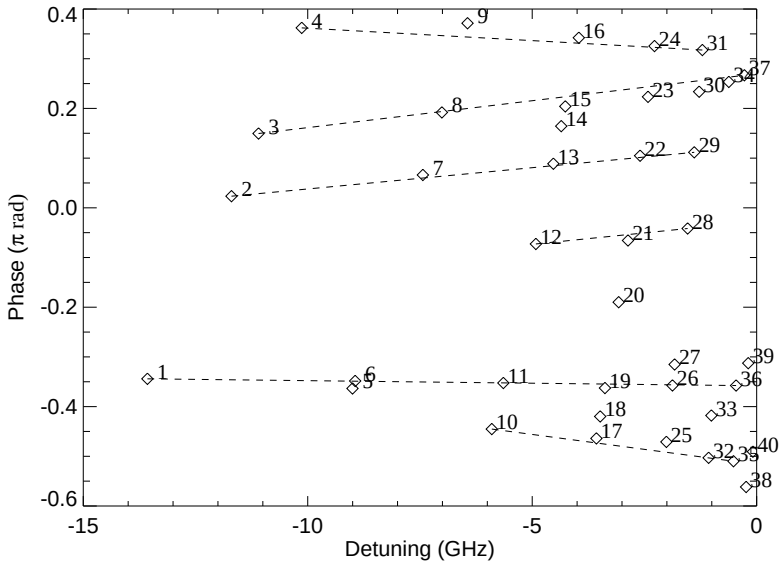

Figure 5.8 Phases at R_0 for each PAS resonance as a function of the energy for potential 15. The dashed lines are a guide line for the eyes and indicate the 6 vibrational series.

approximately becomes

$$\phi = \phi_0 + (d\phi/dE)E \,, \tag{5.12}$$

where

$$\phi_0 = \int_{R_{min}}^{R_0} \sqrt{-2\mu V(R)/\hbar^2} dR \,, \tag{5.13}$$

and

$$\frac{d\phi}{dE} = -\int_{R_{min}}^{R_0} \sqrt{-\mu/2\hbar^2 V(R)} dR \,. \tag{5.14}$$

In these equations R_{min} is the integration limit sufficiently far away from R_{it}. In the same way it can be shown that the phase is linearly dependent on $l(l+1)$.

In order to find the order of magnitude of the slope of the phase with respect to the energy, $d\phi/dE$, we have used the theoretical potential for the $^3\Sigma_g^+$ state calculated by Müller *et al.* [20], which is the only short range 2^3S+2^3P potential

series 1		series 2		series 3	
no.	$-\Delta$ (GHz)	no.	$-\Delta$ (GHz)	no.	$-\Delta$ (GHz)
1	13.57 v_m	2	11.70 v_m	3	11.10 v_m
6	8.94 v_m +1	7	7.44 v_m +1	8	7.01 v_m +1
11	5.64 v_m +2	13	4.53 v_m +2	15	4.26 v_m +2
19	3.38 v_m +3	22	2.60 v_m +3	23	2.42 v_m +3
26	1.88 v_m +4	30	1.28 v_m +4	31	1.21 v_m +4
33	0.98 v_m +5	35	0.52 v_m +5		
36	0.46 v_m +6				
39	0.19 v_m +7				
series 4		series 5		series 6	
no.	$-\Delta$ (GHz)	no.	$-\Delta$ (GHz)	no.	$-\Delta$ (GHz)
12	4.92 v_m	4	10.13 v_m	10	5.90 v_m
21	2.87 v_m +1	9	6.44 v_m +1	17	3.57 v_m +1
28	1.54 v_m +2	16	3.96 v_m +2	25	2.01 v_m +2
		24	2.28 v_m +3	32	1.07 v_m +3
		30	1.28 v_m +4		

Table **5.3** The six series of PAS resonances for which the accumulated phase is slowly varying with energy. The peak numbers correspond to the peak numbers in table 5.1. In parentheses a fictitious vibrational quantum number is shown, where the minimum quantum number v_m is assigned to the resonance with the largest binding energy in each series.

calculated. If the Schrödinger equation 5.6 is numerically solved from the inner turning point to R_0, the slope is found to be $d\phi/dE = -0.0005$ (π rad/GHz).

If equation 5.12 is fitted to the vibrational series in table 5.3, we decide that a series belongs to a certain potential if the reduced chi-square χ^2_{red} is of the order of 1 and the slope $d\phi/dE$ is of the same order of magnitude as the estimated slope in the previous paragraph. In table 5.4 the possible potentials with the corresponding slopes $d\phi/dE$ and the reduced chi-square of the fit for the series 1 to 5 are shown.

For the first vibrational series we find that the χ^2_{red} of the fit is best for potential 15 with $J = 3$ and the slope $d\phi/dE$ is of the right order of magnitude. Moreover, the slope needs to be negative as can be seen from equation 5.14. The other

vibrational series yield slopes that are too large and even positive for potential 15. Therefore, we conclude that the first vibrational series belongs to the 2_u potential with $J = 3$.

The best fit to the data for the second vibrational series is obtained with potential 5, so we assign a $0_u^+(2)$ state to series 2. There are two potentials possible for series 3: potentials 2 and 12, but potential 2 is a gerade potential, so the resonances can not be observed at ENS. As can be seen from table 5.1 the involved resonances have been observed at ENS, so we conclude that vibrational series 3 belongs to potential 12, which is the $1_u(1)$ state. Potential 12 also gives good fit results for vibrational series 4, but, since it is assigned to series 3 and the resonances for series 4 have not been observed at ENS, we assign potential 2 to series 4. This is a 0_g^- state. Series 5 fits well to potentials 4 and 8. The resonances have been observed in Utrecht and at ENS, so potential 8 is not possible. The slope for both potentials is positive, but the error in the slope for potential 4 is comparable to the slope itself and it is possible that it is negative. Therefore, we conclude that series 5 belongs to the $0_u^+(1)$ state. Finally, series 6 gives good results for potential 15 with $J = 2$. This means that series 1 and 6 are different rotational progressions belonging to the $2_u(1)$ potential.

Summarizing, we have identified all series of table 5.3. The involved potentials all have the same $-2C_3/3R^3$ behavior at intermediate range corresponding to attractive Σ states. Moreover, series 1 and 6 are two rotational progressions belonging to the same potential.

Another interesting feature that becomes visible at lower probe laser intensities is an increase of the ionization rate at positive probe laser detunings. A clear example of this is shown in figure 5.9. It is not possible to attribute a shape resonance to this structure as was done in reference [22] to explain the increased ionization at positive detunings from the 2^3S_1-2^3P_1 asymptote. A shape resonance is a quasi-bound state above the dissociation limit, which is bound between the repulsive part of the potential at short internuclear distances and the rotational barrier. The molecular state can dissociate by tunneling through the rotational barrier to large internuclear distances. The existence of a shape resonance was first demonstrated by Boesten *et al.* [51] for the ground state of Rb. In our case the effective potential (including the rotational barrier) in the excited state has a maximum, which is lower than the asymptotic kinetic energy for partial waves up to $l = 11$. For a shape resonance to exist in the excited state l must be equal to or larger 12, but the atoms are reflected from the rotational barrier in the ground state before they reach the internuclear distance from where they can be excited

	potential no.	term symbol	χ^2_{red}	$d\phi/dE$ (π rad/GHz)
series 1	15	$2_u(1)$	3.1	-0.0063 ± 0.0007
series 2	5	$0^+_u(2)$	10.1	-0.0094 ± 0.0008
series 3	2	$0^-_g(1)$	1.6	$+0.0026 \pm 0.0012$
	12	$1_u(1)$	1.8	-0.0097 ± 0.0012
series 4	2	$0^-_g(1)$	0.4	-0.005 ± 0.004
	12	$1_u(1)$	0.3	-0.017 ± 0.004
series 5	4	$0^+_u(1)$	1.1	$+0.0016 \pm 0.003$
	8	$1_g(1)$	1.4	$+0.003 \pm 0.003$
series 6	15	$2_u(1)$	4.6	-0.0058 ± 0.0007

Table **5.4** The reduced chi-square χ^2_{red} and the slope $d\phi/dE$ of a fit of equation 5.12 to the phases in each vibrational series. The results for different potentials are shown. The potential no. corresponds to the potential no. in table 5.2.

to the inner wall of the rotational barrier in the excited state. We conclude that the ionization at positive detunings remains unexplained.

5.4.3 Rotational progressions

In the trap loss measurements two rotational progressions have been observed for the $2_u(1)$ potential. As can be seen from figure 5.7 the $2_u(1)$ state consists of a $j = 2$ state for approximately 40% and a $j = 3$ state for approximately 60% at long range. In the ENS experiment this gives a $J = 2$ and a $J = 3$ state, because $l = 0$. The ground state complex can be excited to both these rotational states as shown before. The rotational energy is included in the potentials by using the approximation given by equation 4.38. The energy separation between two successive rotational states, but with the same vibrational quantum number v is given by

$$E(v, J+1) - E(v, J) = 2B_v(J+1)\,, \tag{5.15}$$

where B_v is the rotational constant. The vibrational quantum number is only known relative to the vibrational quantum number at R_0. The rotational constant is not constant for the vibrational quantum numbers, since the potential is anharmonic. As can be seen from table 5.3 the energy difference between the measured rotational states ranges from 260 MHz to 90 MHz for the vibrational quantum

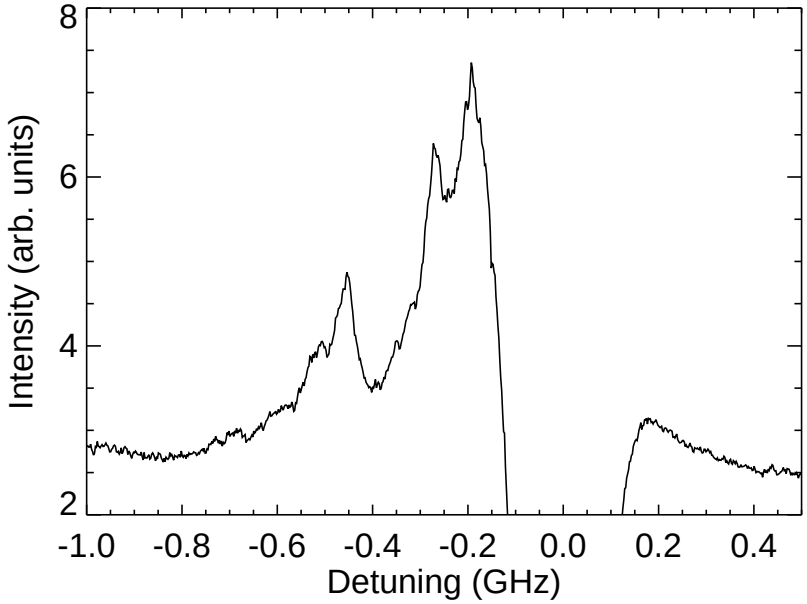

Figure 5.9 Ion spectrum as a function of the probe laser detuning from the 2^3S_1 -2^3P_2 atomic resonance. At positive detunings a clear enhancement of the ionization is visible. At larger positive detunings the ionization slowly decays to the background ionization level.

numbers $v_m + 2$ to $v_m + 5$, where the vibrational numbers for series 1 have been used. The $J = 2$ rotational states for v_m, $v_m + 1$, $v_m + 6$ and $v_m + 7$ have not been observed. The rotational states can be resolved in the spectra, because the width of most peaks is about 30 MHz, which is smaller than the energy separation of the rotational states. As mentioned in section 5.4.1 the photoassociation laser has all polarization components with respect to the direction of **J** in the ground state, which means that excitations to $J = 1, 2$ and 3 can be made. For the 2_u state $\Omega = 2$, so only the $J = 2, 3$ states should be observed, since $J \geq \Omega$.

In the MOT experiments even more rotational states should be present, since over the whole detuning range where data is taken, the $l = 1$ partial wave contributes. From the $^5\Sigma_g^+$ ground state the $J = 0, 1, 2, 3$ and 4 rotational states

can be reached in the excited state for the $l = 1$ partial wave. For the 2_u only $J = 2, 3, 4$ states should be observed. In the MOT the atoms are not spin polarized, which means that **J** in the ground state has no preferred direction. Hence, the photoassociation laser has all polarization components with respect to **J** and excitations to all J are possible. However, in the MOT experiments the $J = 3$ rotational progression and only one PAS resonance of the $J = 2$ progression have been observed. It is not clear why only one of the $J = 2$ PAS resonances is observed in the MOT experiments.

5.5 Line profiles of the PAS resonances

In figure 5.6 a typical PAS resonance is shown. The line profile looks symmetric and we have fitted a Gaussian function to determine the width and the position of the peak. The Gaussian function fitted to the data is also shown in figure 5.6. We have repeated this for all the PAS resonances we have observed and the widths are displayed in table 5.5. As can be seen from this table the peak widths are in general smaller for PAS resonances closer to atomic resonance (increasing peak no.), although the PAS resonance with peak no. 33 is a clear exception to this.

The line profiles can be determined by calculating the rate coefficient for the production of an ion. The rate coefficient is determined with a full quantum close coupling calculation in reference [49] and is derived in a semi-classical way in reference [50]. The rate coefficient is proportional to

$$|S_p(E, l, \omega)|^2 = \frac{\gamma_p \gamma_s(E, l)}{(E - E_b + \hbar\omega)^2 + (\gamma/2)^2} , \tag{5.16}$$

where $S_p(E, l, \omega)$ is the S-matrix element with E the relative kinetic energy of two atoms approaching each other in the ground state, l the partial wave and ω the laser frequency. In equation 5.16 E_b is the position of the bound state. The rate coefficient has a Lorentzian shape with a total width $\gamma = \gamma_p + \gamma_s + \gamma_{mol}$ where γ_p is the ionization rate, γ_s is the stimulated emission rate back into the ground state and γ_{mol} is the molecular linewidth. In the Wigner threshold regime the stimulated emission rate is $\gamma_s = A_l E^{l+1/2}$, with A_l a proportionality constant. According to equation 4.25 the atomic linewidth Γ is proportional to the square of the radial dipole transition matrix element. Using equation 4.46 gives that the molecular linewidth γ_{mol} is in the range $0 \leq \gamma_{mol} \leq 2\Gamma$, where Γ is the atomic natural linewidth. As can be seen from equation 4.46 this depends on the symmetry of the molecular state. This means that the molecular linewidth is smaller than or equal to 3.25 MHz.

peak no.	width (MHz)	peak no.	width (MHz)
1	24 ± 2	21	36 ± 4
2	51 ± 7	22	20 ± 2
3	28 ± 8	23	32 ± 2
4	30 ± 6	24	12 ± 2
5	17 ± 6	25	24 ± 3
6	31 ± 2	26	23 ± 7
7	40 ± 5	27	26 ± 3
8	73 ± 4	28	23 ± 1
9	33 ± 5	29	11 ± 5
10	-	30	21 ± 4
11	30 ± 2	31	14 ± 2
12	32 ± 3	32	-
13	29 ± 3	33	53 ± 2
14	25 ± 5	34	-
15	45 ± 1	35	23 ± 3
16	37 ± 7	36	16 ± 1
17	-	37	18 ± 2
18	20 ± 4	38	-
19	31 ± 4	39	20 ± 3
20	50 ± 24	40	15 ± 2

Table **5.5** Measured widths of the PAS resonances and the corresponding errors. The peak numbers coincide with the peak numbers of table 5.1. The widths of the peaks measured at ENS are not known to us as is indicated with a dash.

In a MOT two atoms approach each other with a distribution of relative kinetic energies and several partial waves can contribute to a collision. The rate coefficient must be averaged over this energy distribution and the contributions for all partial waves must be summed. Napolitano *et al.* [49] have shown that the thermally averaged rate coefficient is given by

$$K_p(T,\omega) = \frac{\Lambda^3}{h}\sum_{l=0}^{\infty}(2l+1)\int_0^{\infty}|S_p(E,l,\omega)|^2 e^{-E/k_BT}dE\,, \qquad (5.17)$$

where $\Lambda = h/\sqrt{2\pi\mu k_B T}$ is the de Broglie wavelength. As a function of the laser

frequency ω the rate coefficient has an asymmetric line profile, since the relative kinetic energy distribution is asymmetric. This causes the line profiles to have a steep edge at the small detuning side and a long "tail" at the large detuning side. This behavior has been demonstrated by Napolitano *et al.* [49] for sodium. Apart from line broadening, the relative kinetic energy distribution causes a shift in the peak positions, because the average of the relative kinetic energy is non-zero. This average is equal to $3k_BT/2$, which is about 58 MHz. This is appreciable and it should be noted that the peak positions used in section 5.4.2 have not been corrected for this. As can be seen from figure 5.6 the line profiles in our measurements do not show the asymmetric shape. Furthermore, the width of the relative kinetic energy distribution corresponding to a temperature $T = 1.9$ mK (see section 3.4.2) is about 50 MHz. This should be a lower limit for the widths of all the PAS peaks, which is not the case as can be seen from table 5.5. From this we must conclude that the width of the relative kinetic energy distribution is smaller than we infer from the calculated width corresponding to a temperature of 1.9 mK.

The line profile becomes more symmetric when ionization plays a more important role. If ionization is the major broadening mechanism in our PAS resonances line profiles, we can determine the number of vibrations in a vibrational state, before it decays through ionization. The lifetime in the vibrational state is $\tau = 1/2\pi\gamma_p$. It should be noted that γ_p corresponds to the full width half maximum of a Lorentzian curve. Therefore, in order to determine γ_p the widths in table 5.5 must be multiplied by a factor $2\sqrt{2\ln 2}$. The oscillation frequency can be calculated by realizing that the phase of the wave function increases with π when the energy changes with $h\nu_{osc}$. Then the oscillation frequency is $\nu_{osc} = h^{-1}\pi/(d\phi/dE)$ and $d\phi/dE$ is calculated numerically. The number of oscillations is $N_{osc} = \tau\nu_{osc}$.

For two of the vibrational series, series 2 (0_u^+) and series 3 (1_u), the lifetime, the oscillation frequency and the number of oscillations are shown for each vibrational level in table 5.6. It can be seen that the number of oscillations in both potentials is nearly constant, except for the vibrational levels close to the dissociation limit and for the vibrational level v_m of the 1_u state. After a time τ the population in a vibrational state has decayed to $1/e$ of its original population. On the other hand, after N_{osc} oscillations the remainder of the population is $(1 - P_{ion})^{N_{osc}}$, where P_{ion} is the ionization probability in the potential. From this the ionization probability in both potentials can be estimated and we find $P_{ion} = 0.154$ for the 0_u^+ potential and $P_{ion} = 0.267$ for the 1_u potential. We can calculate the ionization probability theoretically by assuming that molecules with spin $S = 0$ and

$S = 1$ ionize with almost unity probability and molecules with $S = 2$ can not ionize due to spin conservation rules. Since the Hund's case (c) states can be expanded in a Hund's case (a) basis, we can calculate the populations of the three spin states. From this we find that the ionization probability for the 0_u^+ state is 0.08 and for the 1_u state 0.275 at long range. We assume here that the molecular wave function diabatically keeps the same Hund's case (a) projections until short range. The agreement between theory and experiment is excellent for the 1_u state, but the measured ionization probability for the 0_u^+ state is almost a factor 2 higher than the theoretical value.

The ionization probability in a potential must be constant for each vibrational level, which means that the number of oscillations must be constant. Since the oscillation frequency decreases with increasing vibrational quantum number, the widths of the vibrational peaks must decrease with increasing vibrational quantum number. The lower limit for the width is set by other broadening mechanisms, which might explain that the higher lying vibrational states for both potentials are broader than expected from ionization considerations. We can not explain the too narrow width of the v_m peak in the 1_u potential. For the other vibrational series we measured the analysis of the ionization widths does not yield a constant number of oscillations for each vibrational level.

Now we will discuss the other broadening mechanisms. As was shown in the previous section there is no rotational broadening of the PAS resonances in helium, because the energy separation between rotational states is large and the rotational states can be resolved. The Doppler broadening is estimated from the center-of-mass momentum of the ground state complex. The Doppler shift is introduced in the first term of the numerator of $|S_p(E, l, \omega)|^2$ in equation 5.16. We expect that the Doppler broadening is small and estimate the width by multiplying the width of the center-of-mass momentum distribution with $\hbar k/2M$, where k is the wave vector and M is the mass of the helium atom. This yields a broadening of about 1 MHz, which is much smaller than the width corresponding to the temperature of the atoms.

The recoil of the photon absorbed in the PAS process only introduces a shift of the resonance position and no broadening. This shift is 21 kHz, which is negligible compared to the error in the measured peak positions. Frequency shifts due to density effects are negligible, since the density in our MOT is in the order of 10^9 cm^{-3}, which is very low. The broadening due to the Zeeman effect can be estimated by calculating the standard deviation of the Zeeman shift in the MOT. The magnetic field is zero in the center of the MOT and increases linearly with the

potential	v	γ_p (MHz)	τ (ns)	ν_{osc} (GHz)	N_{osc}
$0_u^+(2)$	v_m	120.1	1.33	5.19	6.90
	v_m +1	94.2	1.69	3.60	6.08
	v_m +2	68.3	2.33	2.45	5.48
	v_m +3	47.1	3.38	1.62	5.44
	v_m +4	49.5	3.22	1.00	3.22
	v_m +5	58.9	2.70	0.52	1.40
$1_u(1)$	v_m	65.9	2.41	4.86	11.71
	v_m +1	171.9	0.93	3.39	3.15
	v_m +2	106.0	1.50	2.28	3.42
	v_m +3	75.4	2.11	1.47	3.10
	v_m +4	33.0	4.83	0.88	4.25

Table **5.6** The vibrational quantum number relative to the lowest measured vibrational state v_m, the lifetime, the oscillation frequency and the number of oscillations for the 0_u^+ and the 1_u potential.

distance from the center. Therefore, the average of the Zeeman shift is zero. In the direction of the probe laser beam the magnetic field gradient is $\alpha = 7.5$ Gauss/cm and the width of the MOT is $r_x = 0.26$ mm (see section 3.4.2). We find that the standard deviation of the Zeeman shift is equal to $\alpha\ r_x$, which corresponds to a frequency width of about 0.27 MHz. This is also small compared to the dominant broadening mechanisms.

5.6 Conclusions

We have performed photoassociation measurements around the 2^3S_1-2^3P_2 asymptote in a He* MOT at a temperature of 1.9 mK. We observed PAS resonances in the ionization signal, which we can identify as vibrational levels in the excited state potentials. Including the photoassociation results of ENS six vibrational series can be distinguished and we attributed potentials to each of them by using the accumulated phase method. A remarkable result is that all these potentials are attractive Σ states, which have a $-2C_3/3R^3$ character at intermediate range. Two rotational progressions ($J = 2$ and $J = 3$) for the $2_u(1)$ potential are present in the trap loss data of ENS. In the ionization measurements the vibrational series

with $J = 3$ and one PAS resonance of the $J = 2$ series are observed. In two of the potentials ($0_u^+(2)$ and $1_u(1)$) the widths of the PAS resonances are predominantly determined by ionization.

Chapter 6

Photoassociation spectroscopy of He(2^3S_1)+He($2^3P_{0,1}$)

6.1 Introduction

In this chapter PAS spectroscopy is studied at the 2^3S_1-2^3P_1 and the 2^3S_1-2^3P_0 asymptotes. In reference [22] peaks and dips have been observed in the ionization rate at the 2^3S_1-2^3P_1 asymptote. Nothing has been reported about ionization measurements around the 2^3S_1-2^3P_0 asymptote. Recently, trap loss measurements in a magnetic trap revealed PAS resonances near the 2^3S_1-2^3P_0 asymptote [43]. We will discuss the ionization measurements around these asymptotes and interpret the results in a qualitative way.

In section 6.2 the experimental conditions are discussed. The measurements around both asymptotes are performed under the same conditions, so this is only described once. In section 6.3 the ionization measurements around the 2^3S_1-2^3P_1 asymptote are described and the accumulated phase analysis is applied to the PAS resonances that have been observed. In section 6.4 the ionization measurements around the 2^3S_1-2^3P_0 are discussed and only a qualitative analysis can be done.

6.2 Experiments

The MOT is loaded with about 10^5 atoms from a liquid helium cooled DC discharge source. The MOT magnetic field is used to slow the atoms down from a mean velocity of 300 m/s to the trapping velocity of the MOT. Both the slowing laser and the MOT laser are locked using saturated absorption spectroscopy at

a detuning of -54 MHz and -14 MHZ from the 2^3S_1-2^3P_2 atomic resonance, respectively. The temperature of the atoms in the MOT is 1.9 mK.

The probe laser setup is shown in figure 3.6. The probe laser is scanned a few GHz around the 2^3S_1-2^3P_1 and 2^3S_1-2^3P_0 atomic resonances with a period of typically 100 s. Since the 2^3S_1-2^3P_2 atomic resonance is just 2.29 GHz below the 2^3S_1-2^3P_1 atomic resonance, it is not relevant to scan the probe laser over detuning ranges much larger than 2.29 GHz. For the photoassociation measurements around the 2^3S_1-2^3P_0 asymptote, the probe laser is scanned over a few GHz, since the deepest attractive potential, the 0_u^+ state, is only about 2 GHz deep. The relative frequency of the probe laser is determined with an FPI and the Lamb dip in the saturated absorption signal is used as an absolute frequency marker.

The MOT laser frequency is periodically switched from the trapping frequency to a detuning of -350 MHz from the 2^3S_1-2^3P_2 atomic resonance with a repetition rate of 25 kHz. The ions produced in the MOT are detected with a micro-channel plates detector. The ion signal is gated and only the ions in the trap-off period are counted. This period is defined as the period when the MOT laser is detuned far from resonance. In this period the MOT does not significantly expand, but all the He(2^3P) atoms have decayed to the He(2^3S) state.

6.3 Measurements around the 2^3S_1-2^3P_1 asymptote

In this section photoassociation experiments near the 2^3S_1-2^3P_1 asymptote are discussed. In section 6.2 the experimental procedure is discussed, in section 6.3.1 the results are presented and in section 6.3.2 the analysis is performed.

6.3.1 Results

The photoassociation process is schematically depicted in figure 5.1. In this case the excited state potentials are connected to the 2^3S_1-2^3P_1 asymptote. When the probe laser is scanned, peaks appear in the ionization signal. A spectrum is shown in figure 6.1. For this spectrum 20 scans are averaged. The peaks in the ionization spectrum are attributed to vibrational states. The dips in the spectrum coincide with the 2^3S_1-2^3P_2 and the 2^3S_1-2^3P_1 atomic resonances. Around these frequencies light pressure on the atoms in the MOT by the probe laser causes trap loss and the trap is emptied at both resonances. The range over which the light pressure induced trap loss is considerable depends on the probe laser intensity.

Six PAS resonances have been observed below the 2^3S_1-2^3P_1 atomic resonance. The detunings from atomic resonance at which these peaks appear to-

peak no.	$-\Delta$ (GHz)	width (MHz)
1	0.452 ± 0.006	16 ± 3
2	0.343 ± 0.009	14 ± 6
3	0.238 ± 0.002	17 ± 1
4	0.159 ± 0.002	13 ± 3
5	0.089 ± 0.017	10 ± 6
6	0.043 ± 0.005	5 ± 3

Table **6.1** Peak positions and the corresponding widths measured below the 2^3S_1 -2^3P_1 asymptote.

gether with the corresponding widths are displayed in table 6.1. It is remarkable that most of the peak widths are smaller than the peak widths measured below the 2^3S_1-2^3P_2 asymptote. Especially the last resonance has a width, which is smaller than the expected width considering the broadening mechanisms present in photoassociation.

We have repeated the experiments discussed above for several probe laser intensities. At high laser intensities ($s_0 = 2 \cdot 10^5$) the MOT is blown away over the whole range where the PAS resonances from table 6.1 have been observed and no additional resonances are found. At low laser intensities ($s_0 = 70$) we have used the first order Bragg reflection of an AOM as a probe laser beam. The probe laser can be switched on in the trap-off period and switched off in the trap-on period in order to disturb the MOT as little as possible. In this way photoassociation can be studied as closely as possible to the dissociation limit. We have not been able to reproduce the effects described in chapter 5 of reference [22]. In this reference dips below atomic resonance and peaks above atomic resonance were observed. The dips were attributed to excitation to so-called purely long range states and the peaks were attributed to a possible shape resonance.

6.3.2 Analysis

There are only 6 attractive states connected to the 2^3S_1 -2^3P_1 asymptote. These states are shown in table 6.2 and figure 6.2. The 0_u^-, $1_g(2)$ and 2_u potentials are purely long range states, which arise due to avoided crossings with repulsive states from the 2^3S_1 -2^3P_2 asymptote. These purely long range states have very large

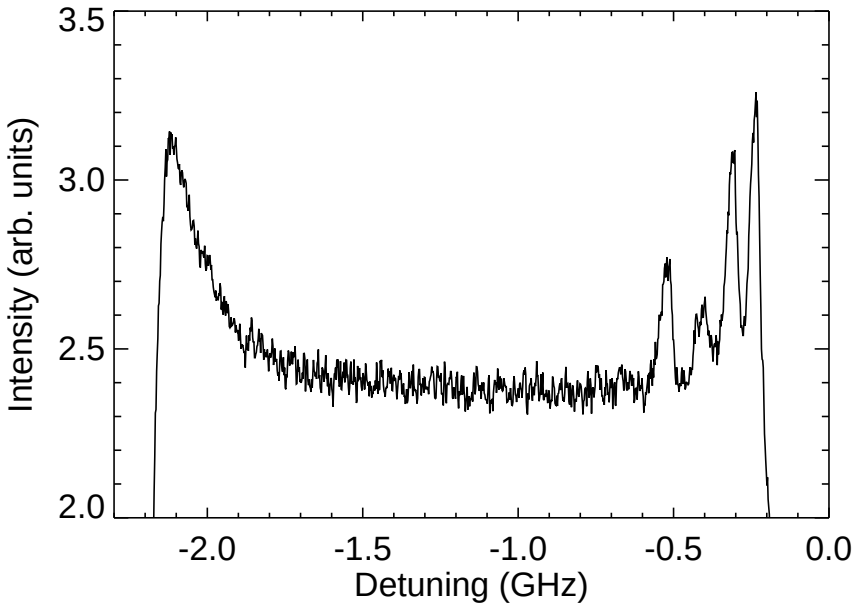

Figure 6.1 Ion spectrum as a function of the probe laser detuning from the 2^3S_1 -2^3P_1 atomic transition. The saturation parameter is a few times 10^4. Clear peaks are observed below resonance, which can be identified as vibrational states in the excited state potentials. The two dips in the ionization signal correspond to the frequency ranges where the probe laser is resonant with the 2^3S_1 -2^3P_2 and the 2^3S_1 -2^3P_1 atomic transitions. The broad structure in the ionization signal above the 2^3S_1 -2^3P_2 atomic transition can not be explained.

classical inner turning points of a few 100 a_0. Since these potentials have large inner turning points, their shapes are completely determined by atomic parameters. Furthermore, these states are very shallow, which means that the vibrational levels are close to the dissociation limit and they have large classical outer turning points. Photoassociation to these states can yield accurate information on the excited state lifetime and retardation effects [7].

The $1_g(1)$ state in table 6.2 has a peculiar shape. Due to two avoided crossings it has a double well structure. In reference [22] this potential was used to

potential no.	term symbol	J_{min}
1	0_g^-	1
2	0_u^+	1
3	0_u^-	0
4	$1_g(1)$	1
5	$1_g(2)$	1
6	2_u	2

Table **6.2** The attractive potentials connected to the 2^3S_1 -2^3P_1 asymptote and the corresponding lowest total angular momentum. The 0_u^-, $1_g(2)$ and the 2_u potentials are purely long range states, which have inner turning points in the order of a few 100 a_0.

explain the ionization peaks at positive detunings from the 2^3S_1 -2^3P_1 asymptote. For the lowest total angular momentum this potential has a maximum above the dissociation limit around 200 a_0. This allows bound states above the dissociation limit, which are called shape resonances. The $l = 0$ partial wave in the ground state can be excited to this shape resonance. However, neither the dips associated to the purely long range states nor the peaks at positive detunings associated to the shape resonances have been observed in our spectra.

For the six vibrational peaks that appear in the ionization spectra, we have performed the same analysis as is discussed in section 5.4.2. The accumulated phase at $R_0 = 20$ a_0 for each PAS resonance has been calculated. This is done for the six potentials mentioned in table 6.2 including rotation and the phases are plotted against the corresponding binding energies. If the six PAS resonances belong to one potential, the phases must be on a straight line and the slope of the line has to be small. This is not the case. Only for the 0_u^+ potential the PAS resonances 2 and 4 are on a nearly vertical line with a slope $d\phi/dE = -0.025 \pm 0.0018$ (π rad/GHz). This is shown in figure 6.3. The two resonances are successive vibrational levels, which can be deduced from the number of nodes the wave function has between infinite internuclear distance and $R_0 = 20$ a_0. The other resonances do not yield phases on a line slowly varying with energy. Therefore, we conclude that the PAS resonances 2 and 4 belong to the 0_u^+ potential, although it is possible that they coincidentally have almost identical phases and belong to different potentials.

The vibrational energies in the purely long range states connected to the 2^3S_1-

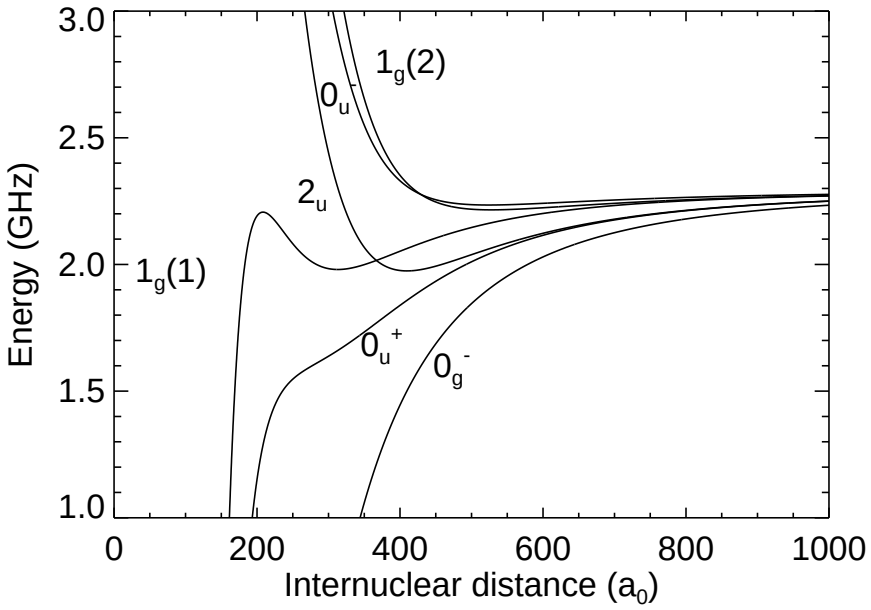

Figure 6.2 The attractive potentials connecting to 2^3S_1 -2^3P_1 asymptote. The 0_u^-, $1_g(2)$ and 2_u potentials are purely long range potentials.

2^3P_1 and the 2^3S_1-2^3P_0 asymptotes have been calculated in a multi-channel calculation by Venturi *et al.* [52]. In table 6.3 their calculated binding energies are shown for the ro-vibrational levels in the purely long range states. The purely long range potential $1_g(1)$ can not support bound states. Excitation to the vibrational states in purely long range states can not lead to ionization, because the atoms in the bound state do not approach each other closely enough for PI to occur. However, the $v = 1$, $J = 2$ ro-vibrational state of the 2_u state connected to the 2^3S_1-2^3P_1 asymptote coincides with the 5th PAS resonance in 6.1 within the error. This might indicate that the purely long state, which is caused by an avoided crossing with a repulsive state from the 2^3S_1-2^3P_2 asymptote, is coupled to the resulting adiabatic potential connected to the 2^3S_1-2^3P_2 asymptote.

term symbol	v	$J=0$	$J=1$	$J=2$	$J=3$
0_u^-	0	-18.27		-7.77	
2_u	0			-191	-167
	1			-72	-57
	2			-21.5	-14.4
	3			-4.7	-2.2

Table **6.3** Binding energies for the ro-vibrational levels with $J \leq 3$ in the purely long range potentials 0_u^- and 2_u connected to the 2^3S_1-2^3P_1 asymptote calculated by Venturi *et al.* [52]. Only certain values of J are allowed due to boson statistics for the nuclei.

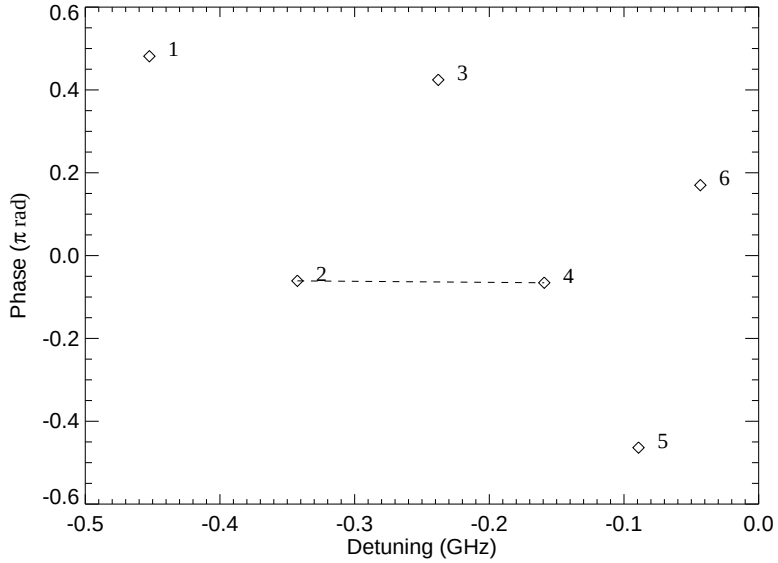

Figure 6.3 Phases at R_0 for each PAS resonance as a function of the energy for potential 2. The dashed line is a guide line for the eyes and indicates that resonances 2 and 4 can belong to the same vibrational series.

6.4 Measurements around the 2^3S_1-2^3P_0 asymptote

In this section PAS around the 2^3S_1-2^3P_0 asymptote is studied. The experiments are described in section 6.2, the results are discussed in section 6.4.1 and a qualitative analysis is given in section 6.3.2.

6.4.1 Results

An ion spectrum is shown in figure 6.4. For this figure about 30 spectra are averaged. The on resonance saturation parameter used is about 10^3. A clear enhancement of the ionization is observed just below the atomic resonance. No PAS resonances can be observed in the spectrum. Furthermore, a clear enhancement of the ionization can be observed at positive detunings. The maximum of the ionization rate at positive detunings is higher than the maximum of the ionization rate at negative detunings. In between the two maxima the MOT is emptied by the light pressure from the probe laser and the ionization signal drops to zero. We used the AOM to turn off the probe laser beam in the trap-on period in order to get closer to resonance without disturbing the MOT cloud. Without the AOM the dip in the ionization becomes wider, because the probe laser is on continuously and the intensity is a factor of 1.5 higher. This means that the MOT is disturbed over a larger frequency range. The ionization increase at positive detunings disappears, but it is present at negative detunings for higher probe laser intensities.

6.4.2 Analysis

The PAS process is schematically shown in figure 6.5. The two other asymptotes of the excited state are also shown, but the energy splitting is not on the right scale. There are two purely long range potentials and two repulsive potentials at the 2^3S_1-2^3P_0 asymptote. The purely long range states, the 0_u^+ and the 1_g state, have large classical inner turning points, which means that PI is negligible. Therefore, it is not expected to observe vibrational states or optical collisions in ionization measurements.

However, the ionization signal below atomic resonance is similar to the ionization enhancement due to optical collisions below the 2^3S_1 -2^3P_2 asymptote. The enhancement of the ionization signal becomes considerable at larger negative detunings for higher probe laser intensities. This is an indication of optical collisions, because power broadening in the photoabsorption process makes it possible to excite ground state atoms further away from the Condon radius. It is possible

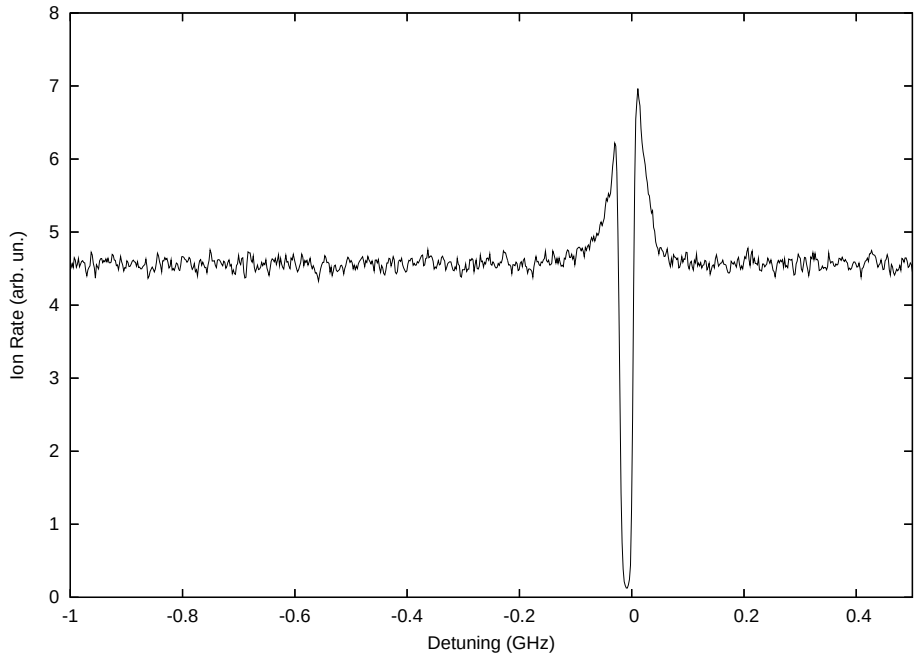

Figure 6.4 Ion spectrum as a function of the probe laser detuning from the $2^3\mathrm{S}_1$ -$2^3\mathrm{P}_0$ atomic transition. The saturation parameter is about 10^3. Just below atomic resonance the ionization signal increases and at resonance it decreases to zero, because the atoms in the are ejected from the MOT by light pressure. Above atomic resonance there is also an increase of the ionization signal.

that ground state atoms, which are excited to the purely long range states, make diabatic crossings to attractive states connected to the other asymptotes and subsequently, the system can ionize at short range. It is a tedious task to calculate these transition rates, because the subspaces of the 0_u^+ and the 1_g potentials have dimensions four and six, respectively, which means that multichannel calculations are required.

If we assume that the ionization signal at negative detunings is caused by optical collisions, it is not clear why PAS resonances have not been observed. The system should ionize via the same path when vibrational states are excited. Nevertheless, photoassociation to the vibrational states can be observed in trap loss

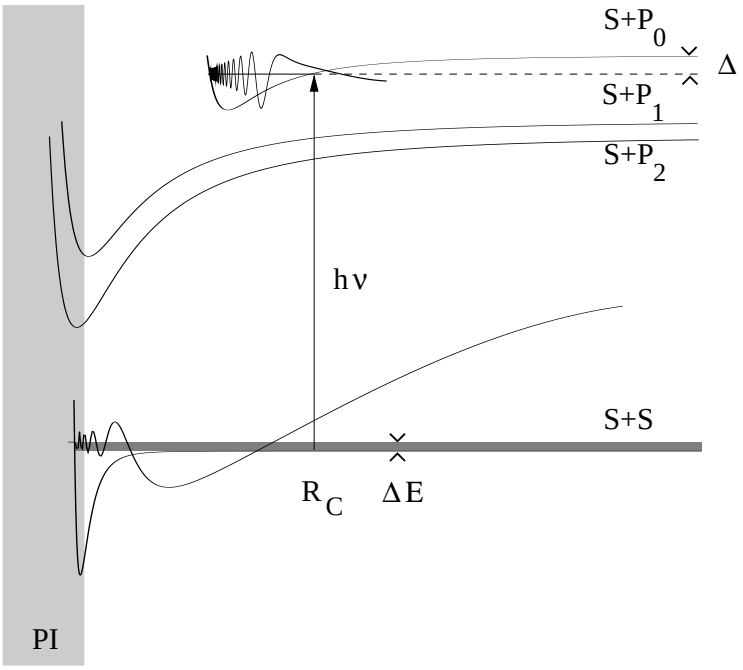

Figure 6.5 Schematic picture of the PAS process. The ground state potential is denoted with S+S and the excited state potentials with S+P_j. Three potentials connected to the three asymptotes are shown. The asymptotes are separated by the fine structure splitting and it must be noted that the figure is not drawn on the right scale. The potential connected to the 2^3S_1-2^3P_0 asymptote is a purely long range potential. The initial kinetic energy spread ΔE is represented by the dark shaded area. The light shaded area indicates the internuclear distances at which Penning ionization (PI) may occur. The detuning Δ from atomic resonance dictates the Condon radius R_C at which the system can be excited to the S+P_0 potential by absorption of a photon energy $h\nu$. A typical ground state wave function and an excited state wave function are shown.

measurements as was shown in reference [43]. Since these measurements are performed in a magnetic trap, the atoms in the ground state approach each other on the $^5\Sigma_g^+$ potential. This means that photoassociation can only take place to the 0_u^+ excited state. Five PAS resonances can be distinguished in the trap loss data and there is excellent agreement between the measured binding energies and the cal-

culated binding energies reported in reference [43] and [52]. The resonances are extremely narrow with widths of about 3 MHz. The temperature in the magnetic trap is about 5 μK, so thermal broadening is negligible. The probe laser is cavity-stabilized and has a narrow width of 0.3 MHz. The molecular linewidth is smaller than or equal to 3.25 MHz. The measured linewidths satisfy this condition, which shows that the widths of the line profiles are almost entirely determined by the probe laser linewidth and the molecular linewidth. This means that broadening due to ionization and hence the ionization probability from these states must be negligible. Therefore, it remains a mystery why we are able to observe ionization in optical collisions.

Finally, the ionization increase at positive detunings is similar to the ionization signal at positive detunings from the 2^3S_1 -2^3P_2 asymptote. It is visible at lower probe laser intensities, because the frequency range around atomic resonance for which the MOT cloud is disturbed becomes larger for higher probe laser intensities. Since we are not able to explain the effects at the 2^3S_1 -2^3P_2 asymptote, we can give no explanation for the 2^3S_1 -2^3P_0 asymptote either.

6.5 Conclusions

We have studied photoassociation near the 2^3S_1 -2^3P_1 and 2^3S_1 -2^3P_0 asymptotes in a He* MOT at a temperature of 1.9 mK. Six PAS resonances are observed below the 2^3S_1 -2^3P_1 asymptote from which two resonances belong to the 0_u^+ potential. Below the 2^3S_1 -2^3P_0 asymptote no PAS resonances have been observed in ionization measurements. The PAS resonances in the trap loss measurements of ENS show negligible broadening due to ionization, which can be explained by the fact that the potentials connecting to the 2^3S_1 -2^3P_0 asymptote are purely long range states. It is remarkable that a clear ionization enhancement below atomic resonance, which resembles optical collisions, is present in the ionization measurements. If ionization is completely absent, neither PAS resonances nor optical collisions should be observed. It is possible that the systems in the purely long range states make diabatic crossings to attractive states connecting to other asymptotes. However, it is difficult to estimate the transition rates, because multichannel calculations are required. Finally, an ionization enhancement is observed above atomic resonance, which can not be explained yet.

Bibliography

[1] H. Scheingraber and C.R. Vidal, J. Chem. Phys. **66**, 3694 (1977)

[2] H.J. Metcalf and P. van der Straten, *Laser Cooling and Trapping*, Springer-Verlag, New York, (1999)

[3] E. Raab, M. Prentiss, A. Cable, S. Chu and D. Pritchard, Phys. Rev. Lett. **59**, 2631 (1987)

[4] H. R. Thorsheim, J. Weiner and P. S. Julienne, Phys. Rev. Lett. **58**, 2420 (1987)

[5] P. D. Lett, K. Helmerson, W. D. Philips, L. P. Ratliff, S. L. Rolston, and M. E. Wagshul, Phys. Rev. Lett. **71**, 2200 (1993)

[6] W. I. McAlexander, E. R. I. Abraham, and R. G. Hulet, Phys. Rev. A **54**, R5 (1996)

[7] K. M. Jones, P. S. Julienne, P. D. Lett, W. D. Phillips, E.Tiesinga, and C. J. Williams, Europhys. Lett. **35**, 85 (1996)

[8] E. R. I. Abraham, W. I. McAlexander, J. M. Gerton, R. G. Hulet, R. Côté, and A. Dalgarno, Phys. Rev. A **53**, R3713 (1996)

[9] G. V. Shlyapnikov, J. T. M. Walraven, U. M. Rahmanov, and M. W. Reynolds, Phys. Rev. Lett. **73**, 3247 (1994)

[10] A. Robert, O. Sirjean, A. Browaeys, J. Poupard, S. Nowak, D. Boiron, C. I. Westbrook, and A. Aspect, Science **292**, 461 (2001)

[11] F. Pereira Dos Santos, J. Léonard, Junmin Wang, C. J. Barrelet, F. Perales, E. Rasel, C. S. Unnikrishnan, M. Leduc, and C. Cohen-Tannoudji, Phys. Rev. Lett. **86**, 3459 (2001)

[12] D.W. Fahey, W.F. Parks and L.D. Shearer, J. Phys. E: Sci. Instrum. **13**, 38 (1980)

[13] K. Ohno, T. Takami, K. Mitsuke and T. Ishidsa, J. Chem. Phys. **94**, 2675 (1991)

[14] G. Nienhuis, P. van der Straten and S-Q. Shang, Phys. Rev. A **44**, 462 (1991)

[15] P. van der Straten, S-Q. Shang, B. Sheehy, H. Metcalf and G. Nienhuis, Phys. Rev. A **47**, 4161 (1993)

[16] A. Koolen, *Dissipative Atom Optics with Cold Metastable Helium Atoms*, Ph.D. Thesis, Eindhoven University of Technology, (2000)

[17] M. Hoogerland, *Laser Manipulation of Metastable Neon Atoms*, Ph.D. Thesis, Eindhoven University of Technology, (1993)

[18] J. Kawanaka, M. Hagiuda, K. Shimizu, F. Shimizu and H. Takuma, Appl. Phys. B **56**, 21 (1993)

[19] M. T. Cashen, *Optical Forces on Atoms in Polychromatic Light Fields*, Ph.D. Thesis, S.U.N.Y at Stony Brook, (2002)

[20] M. W. Müller, A. Merz, M. W. Ruf, H. Hotop, W. Meyer, and M. Movre, Z. Phys. D **21**, 89 (1991)

[21] G.R. Woestenenk, J.W. Thomsen, M. van Rijnbach, P. van der Straten, Rev. Sci. Instrum. **72**, 3842 (2001)

[22] G. Woestenenk, *Photoassociation of Cold Metastable Helium Atoms*, Ph.D. Thesis, University of Utrecht, (2001)

[23] F. Reif, *Fundamentals of Statistical and Thermal Physics*, McGraw-Hill, Singapore, (1985)

[24] F. Bardou, O. Emile, J.M. Courty, C.I. Westbrook, A. Aspect, Europhys. Lett. **20**, 681 (1992)

[25] M. Kumakura and N. Morita, Jpn. J. App. Phys. **31**, 276 (1992)

[26] V. G. Minogin and V. S. Letokhov, *"Laser Light Pressure on Atoms"*, Institute of Spectroscopy, USSR Academy of Science, Moscow, USSR, (1987)

[27] F. Pereira Dos Santos, *Condensation de Bose-Einstein de l'helium metastable*, Ph.D. Thesis, ENS in Paris, (2001)

[28] R. Zare, *"Angular momentum: Understanding Spatial Aspects in Chemistry and Physics"*, Wiley, New York, (1988)

[29] J. T. Hougen, *"The Calculation of Rotational Energy Levels and Rotational Line Intensities in Diatomic Molecules"*, Nat. Bur. Stand. (U.S.), Monogr. 115, Washington D.C., (1970)

[30] I. Roeggen, Theor. Chim. Acta **21**, 398 (1971)

[31] B. Linder and J. O. Hirschfelder, J. Chem. Phys. **28**, 197 (1958)

[32] B. H. Bransden and C. J. Joachain, *"Physics of atoms and molecules"*, Longman, Essex, (1991)

[33] R. W. Heather and P. S. Julienne, Phys. Rev. A **47**, 1887 (1993)

[34] J. Castillega, D. Livingston, A. Sanders, and D. Shiner, Phys. Rev. Lett. **84**, 4321 (2000)

[35] M. C. George, L. D. Lombardi, and E. A. Hessels, Phys. Rev. Lett. **47**, 173002 (2001)

[36] Bo Gao, Phys. Rev. A **54**, 2022 (1996)

[37] G. Herzberg, *"Spectra of diatomic molecules"*, Van Nostrand, New York, (1950)

[38] P. A. Molenaar, P. van der Straten, and H. G. M. Heideman, Phys. Rev. Lett. **77**, 1460 (1996)

[39] R. A. Cline, J. D. Miller, and D. J. Heinzen, Phys. Rev. Lett. **73**, 632 (1994)

[40] H. Wang, P. L. Gould, and W. C. Stwalley, Phys. Rev. A **53**, 1216 (1996)

[41] N. Herschbach, P. J. J. Tol, W. Vassen, W. Hogervorst, G. Woestenenk, J. W. Thomsen, P. van der Straten, and A. Niehaus, Phys. Rev. Lett. **84**, 1874 (2000)

[42] Kalle-Antti Suominen, J. Phys. B: At. Mol. Opt. Phys. **29**, 5981 (1996)

[43] J. Léonard, M. Walhout, A. P. Mosk, T. Müller, M. Leduc, and C. Cohen-Tannoudji, Phys. Rev. Lett. **91**, 073203-1 (2003)

[44] W. Demtröder, *"Laser Spectroscopy"*, Springer-Verlag, Berlin, (1996)

[45] R. J. Leroy and R. B. Bernstein, J. Chem. Phys. **52**, 3869 (1970)

[46] A. J. Moerdijk, W. C. Stwalley, R. G. Hulet, and B. J. Verhaar, Phys. Rev. Lett. **72**, 40 (1994)

[47] A. Crubellier, O. Dulieu, F. Masnou-Seeuws, M. Elbs, H. Knöckel, and E. Tiemann, Eur. Phys. J. D **6**, 211 (1999)

[48] J. Léonard, private communication.

[49] R. Napolitano, J. Weiner, C. J. Williams, and P. S. Julienne, Phys. Rev. Lett. **73**, 10 (1994)

[50] J. L. Bohn and P. S. Julienne, Phys. Rev. A **60**, 414 (1999)

[51] H. M. J. M. Boesten, C. C. Tsai, B. J. Verhaar, and D. J. Heinzen, Phys. Rev. Lett. **77**, 5194 (1996)

[52] V. Venturi, P. J. Leo, E. Tiesinga, C. J. Williams, and I. B. Whittingham, Phys. Rev. A **68**, 022706-1 (2003)

Samenvatting

Aan het einde van de zeventig jaren werden de eerste experimenten uitgevoerd, waarin atomen door middel van laserlicht werden afgekoeld. Tegenwoordig worden in laboratoria over de hele wereld atomen afgekoeld tot enkele duizendsten van graden, of nog veel minder, boven het absolute nulpunt: $-273,15$ °C. Bij het absolute nulpunt staan atomen stil, terwijl bij kamertemperatuur ze met enkele duizenden km/u bewegen.

Laserlicht bestaat uit fotonen: deeltjes, die geen massa hebben, maar wel impuls. Als een foton de juiste golflengte heeft, kan het een atoom, dat zich in een bepaalde energietoestand bevindt, aanslaan naar een hoger gelegen energietoestand. Het atoom krijgt daarbij een duwtje in de richting van het foton. Aangezien het hoger gelegen energietoestand niet een stabiele toestand is voor het atoom, valt het na een tijdje weer terug naar het lager gelegen energietoestand onder uitzending van een foton. Van dit foton ondervindt het atoom een duwtje in de richting tegenovergesteld aan de richting waarin dit foton wordt uitgezonden. Het foton kan echter in een willekeurige richting worden uitgezonden. Na vele malen fotonen geabsorbeerd en uitgezonden te hebben, middelen de duwtjes van de uitgezonden fotonen uit en houdt het atoom slechts de duwtjes van de geabsorbeerde fotonen over. Deze zijn allemaal in de richting van de laserbundel, waarin het atoom zich bevindt. Meerdere atomen met verschillende snelheden zullen allemaal worden afgeremd naar bijna dezelfde lage snelheid. Als de spreiding in snelheden afneemt, betekent dit dat de groep atomen gekoeld wordt. De bewegingsenergie, die de atomen verloren hebben, zit in de uitgezonden fotonen, die een iets andere golflengte hebben gekregen dan de fotonen, die geabsorbeerd zijn.

In dit proefschrift worden helium atomen in de metastabiele toestand bestudeerd. Deze toestand wordt aangeduid met He*. Het is een metastabiele toestand, omdat het meer dan twee uur duurt, voordat het atoom terugvalt naar de laagst gelegen energietoestand van helium. Op de tijdschaal van de experimenten is dit erg lang. In hoofdstuk 2 wordt beschreven hoe een bundel van He* atomen, die

uit een met vloeibaar stikstof gekoelde bron komt, parallel gemaakt kan worden door met laserlicht loodrecht op de atoombundel te schijnen. Hoewel de bron met vloeibaar stikstof gekoeld wordt, komen de atomen nog met een snelheid van 3600 km/u uit de bron. Een atoombundel is meestal divergent, dat wil zeggen, dat de atomen als een kegel uit een diafragma komen. Om een hogere bundelintensiteit te creëren, kan men zo'n atoombundel parallel maken. Hiervoor gebruiken we een zogenaamde collimator, die bestaat uit twee paren spiegels waartussen vier laserbundels reflecteren, die de snelheidscomponenten van de atomen loodrecht op de atoombundel kleiner maken. Om over zo'n lang mogelijke afstand interactie met de atomen te hebben, worden de laserbundels meerdere malen gereflecteerd. Als de snelheidscomponenten in de richting van de atoombundel niet veranderen, wordt de atoombundel paralleller. In hoofdstuk 2 worden onder meer de toename van de atoombundelintensiteit en het snelheidsgedrag van de atomen in de collimator bestudeerd.

In hoofdstuk 3 wordt beschreven hoe atomen, die uit een met vloeibaar helium gekoelde bron komen, afgeremd worden van ongeveer 1000 km/u naar enkele tientallen kilometers per uur door een laserbundel, die tegen de richting van de atoombundel inloopt. Daarna worden de atomen door drie tegen elkaar inlopende paren van laserbundels in drie dimensies afgekoeld. Echter, de atomen kunnen, ondanks hun lage snelheden, nog alle kanten op bewegen. Als bovendien een magneetveld wordt aangebracht, dat nul is in het snijpunt van de zes laserbundels en toeneemt met de afstand tot dit snijpunt, kunnen de atomen gevangen worden. Dit samenspel van laserlicht en het magneetveld wordt een magneto-optische val genoemd. We kunnen ongeveer 100.000 He* atomen invangen en afkoelen tot ongeveer twee duizendste graad boven het absolute nulpunt. In de magneto-optische val bewegen de atomen op een afstand van enkele tientallen micrometers van elkaar. Metastabiele helium atomen hebben een grote interne energie en als twee atomen bij elkaar in de buurt komen, kan er spontaan een geladen deeltje onstaan: een helium ion. Deze geladen deeltjes kunnen makkelijk worden gedetecteerd met detectors. Met een extra laserbundel kunnen vrije atoomparen aangeslagen worden naar een gebonden toestand in een molekuul. De atoomparen worden aan elkaar gebonden (geassociëerd) door het absorberen van een foton uit de laserbundel en dit proces wordt ook wel foto-associatie genoemd.

Hoofdstuk 4 geeft een theoretische beschrijving van alle toestanden, waarin deze helium molekulen zich kunnen bevinden. De gevormde molekulen bezitten allerlei symmetriëen, zoals spiegeling in een vlak, dat de verbindingslijn tussen de atomen bevat, of spiegeling van de elektronen in het punt, dat precies tussen

de twee atomen in ligt. Deze symmetriëen staan een unieke naamgeving toe aan alle toestanden, waarin de molekulen zich kunnen bevinden. De energiëen van deze toestanden zijn afhankelijk van de afstand tussen de twee atomen. Tenslotte wordt er afgeleid welke veranderingen in symmetrie er plaatsvinden als een vrij atoompaar wordt aangeslagen naar een gebonden toestand door de absorptie van een foton.

In hoofdstuk 5 worden de resultaten van de experimenten, die met de in hoofdstuk 3 beschreven opstelling zijn gedaan, en de analyse van deze resultaten beschreven. De extra laserbundel creëert molekulen met discrete vibratiemodes en de atomen in deze molekulen worden naar elkaar toe versneld. De waarschijnlijkheid, dat een helium ion ontstaat, neemt dan toe en een vibratiemode van het molekuul kan worden waargenomen als een piek in het detectorsignaal. Als de golflengte van het laserlicht wordt gevariëerd, verschijnen meerdere pieken. Met behulp van berekeningen kunnen hierin zes verschillende series pieken herkend worden, die bij zes verschillende toestanden van het molekuul horen. De beschreven experimentele methode wordt foto-associatie spectroscopie genoemd. Voor twee van de gemeten series kunnen de breedtes van de pieken verklaard worden door de waarschijnlijkheid, dat er een ion ontstaat in de bijbehorende toestand.

In hoofdstuk 6 worden de metingen, die zijn beschreven in hoofdstuk 5, herhaald voor andere energietoestanden van de molekulen. Voor grote afstanden tussen de atomen van het molekuul gaan de energiëen van al deze toestanden naar twee specifieke waarden. Deze twee waarden liggen beide hoger dan de energie waar alle toestanden, behorende bij de metingen van hoofdstuk 5, naar toe gaan voor grote afstanden tussen de twee atomen. Voor de laagste van de twee energiewaarden worden vijf pieken gemeten en met behulp van de analyse, die we ook in hoofdstuk 5 gebruikt hebben, kunnen twee van deze pieken worden toegekend aan één toestand van het molekuul. Voor de hoogste van de twee energiewaarden worden geen pieken gemeten, maar dit kan verklaard worden, doordat in dit geval molekulen worden gemaakt, waarin de atomen nooit dicht bij elkaar kunnen komen. Er worden dan ook geen ionen gevormd. In het detectorsignaal zijn wel twee andere effecten zichtbaar, waarvoor we geen verklaring hebben kunnen vinden.

Curriculum Vitae

Naam	Michiel van Rijnbach.
Geboren	5 augustus 1973 te Veenendaal.
Onderwijs	1985-1991 VWO, Ichthus College, Veenendaal.
Studie	1991-1997 Experimentele Natuurkunde, Universiteit Utrecht. Experimenteel Afstudeeronderzoek: ”Cold collision studies using a metastable helium mangeto-optical trap” o.l.v. Drs. H. Mastwijk, Dr. J. W. Thomsen en Dr. P. van der Straten.
Promotieonderzoek	1998-2003 Atom Optics and Ultrafast Dynamics, Debye Instituut, Universiteit Utrecht. Proefschrift: ”Dynamical spectroscopy of Transient He_2 Molecules” o.l.v. Prof. Dr. P. van der Straten.
Conferenties	Euroconference on Slow Collisions between Laser Manipulated Systems (ESCOLAR) ’98, Rust, Oostenrijk, 1-5 April 1998. Euroconference on Slow Collisions between Laser Manipulated Systems (ESCOLAR) ’99, Elounda Bay, Kreta, Griekenland, 1-4 mei 1999. Cold Molecules 2001: ”Coherent Control and Cold Molecules”,

	Gif-sur-Yvette, France, 21-25 oktober 2001.
Cursussen	Cursus ’Planmatig Werken’, 27-28 april 1998.
	Cursus ’Persoonlijke Vaardigheden, 10-11 februari en 13 maart 2000.
Werkbezoek	State University of New York, Stony Brook, NY, USA, oktober-december 1998.

Publications

- *Photo induced collisions with laser cooled He* stoms*
  H. C. Mastwijk, M. van Rijnbach, J. W. Thomsen, P. van der Straten,
  and A. Niehaus,
  Eur. J. Phys. D **4**, 131, (1998)

- *Collisions between ultracold metastable He atoms*
  G. Woestenenk, H.C. Mastwijk, J.W. Thomsen, P. van der Straten,
  M. Pieksma, M. van Rijnbach, and A. Niehaus,
  Nucl. Instr. and Meth. in Phys. B **154** 194, (1999)

- *Construction of an Intense Low Velocity Metastable Helium Atomic Beam*
  G. R. Woestenenk, J.W. Thomsen, M. van Rijnbach,
  P. van der Straten, and A. Niehaus,
  Rev. Sci. Instrum. **72**, 3842, (2001)

Dankwoord

Zoals iedereen weet, heeft deze promotie veel langer geduurd dan de bedoeling was. Maar alles is tot een goed einde gekomen en ligt er nu een proefschrift voor u. Ondanks veel tegenslagen in de experimenten, heb ik wetenschap toch leren kennen als een spannend proces. Het is interessant om te zien hoe denkbeelden over fysische processen van de éne op de andere dag kunnen veranderen. Ik heb dan ook erg veel geleerd in de afgelopen jaren. Niet alleen op het gebied van de fysica, maar ook in het omgaan met tegenslagen. Ik sta bekend als een paniekvogel, maar ik hoop toch, dat vooral het laatste jaar me geleerd heeft rustig te blijven onder bepaalde omstandigheden. Dit lijkt me de belangrijkste eigenschap bij het experimenteren in de fysica.

Aangezien ik zo'n lange tijd bij de vakgroep Atoomfysica, die later ondergebracht is in de onderzoeksgroep Atom Optics and Ultrafast Dynamics, ben verbleven, heb ik ook een heleboel mensen te bedanken. Als eerste begin ik met mijn promotor, die voor het einde van mijn promotie met emiritaat is gegaan: Arend Niehaus. Het is jammer, dat we niet meer samen hebben kunnen werken, maar voordat de resultaten binnenkwamen, bent u naar Duitsland verhuisd. Ik wil Peter van der Straten, eerst mijn co-promoter en vervolgens mijn promotor, heel erg bedanken voor alle inspanningen, die hij voor mijn promotie heeft gedaan. Alhoewel we het vaak oneens waren over de fysica en ik je vaak tot waanzin heb gedreven, denk ik, dat we toch beiden op onze eigen manier hebben genoten van de berekeningen, die we hebben gedaan. Ik heb bewondering voor de manier waarop je met je promovendi omgaat. Je maakt het ons soms te makkelijk om bij je de kamer in te stappen om iets te vragen. Maar dit geeft toch maar aan, dat je ons als gelijke beschouwt en vertrouwt, dat we af en toe ook iets zinnigs kunnen zeggen.

I also would like to thank Harold Metcalf for having me work in his lab. Although the helium source did not work right away, it is probably one of the few Shimizu type helium sources working in the world at the moment. It is easy

to get along with you and it was an honour to work with the man who did the first Zeeman slowing experiments. Thank you, i had a great time in Stony Brook.

In het lab heb ik altijd prettig samen kunnen werken met de collega's. Jan Thomsen, thank you for the fun time we had in the lab. Marc Pieksma was immer het zonnetje in het lab en heeft mij goed geholpen met het uitlijnen van de collimator. Met je scherpe ogen kon je alles op sub-millimeters aflezen. Geraldine, bedankt voor je morele support in de e-mails, die we hebben geschreven, nadat je gepromoveerd was. Ook de technische informatie kwam van pas, want zodoende kon ik jouw opstelling weer draaiende krijgen. When the last measurements had to be performed, Driss Nehari became a postdoc on the helium setup. Thank you for the suggestions to improve things in the setup. I think it was good that i had to explain the setup to you, because it made me stay in the lab at times i wanted to run away. Good luck with the future experiments.

Ik heb ook nog een aantal studenten mogen begeleiden, maar bij de eerste student had ik meer het gevoel, dat ik begeleid werd. Dit was Dries, een uitzonderlijk energieke vent, die af en toe de oren van je kop kletste. Bedankt voor het locken van de lasers. Later ben je mijn collega geworden en heb ik nog veel van je kennis kunnen profiteren. Ik moet zeggen, dat ik toch erg blij ben, dat ik net voor je promoveer. Daarna kwam Vincent en heeft de collimator aan de gang weten te krijgen. Het was geen makkelijke klus. Radboud Pos wil ik bedanken voor zijn eindeloze geduld bij het uitlijnen van de bundel-lijn. Niels Hamaker had de pech zijn intrede te doen toen de helium-bron kapot was gegaan. Bedankt, jij kon er verder ook niets aan doen.

De onderdsteunende technici blijken altijd weer onmisbaar bij het experiment. Hans en Frits, bedankt voor jullie goede zorgen, ik heb jullie maar met vele karweitjes opgezadeld. Jitse, bedankt, dat je het wakende oog was over mijn opstelling. Vaak constateerde jij een vacuüm-probleem al voordat ik binnen was. Toen de vakgroep overging in Atom Optics and Ultrafast Dynamics heb ik ook nog even van Paul Jurrius' kwaliteiten gebruik mogen maken. Bedankt, je hebt ook de vrolijke noot in het werk gebracht. Natuurlijk wil ik ook de mensen van het IGF bedanken voor het vliegensvlug maken van allerlei onderdelen voor de opstelling en hierbij wil ik in het bijzonder Mari, Gerard en John noemen. Verder wil ik ook Nico, Jan en Johan van het cryogene lab bedanken voor de talloze vaatjes vloeibaar helium waar ze mij mee hebben voorzien. In de tijd, dat ik meer dan twaalf uur per dag aan het meten was, zorgde Nico er altijd weer voor, dat er twee vaatjes per dag voor me klaar stonden. Door mijn lange verblijf heb ik maar liefst drie secretaresses meegemaakt. Hanneke, Esther en Clarien, allen bedankt.

De andere promovendi hebben er voor gezorgd, dat er erg veel gelachen werd tijdens het werk. Een niet onbelangrijk punt. Hierbij wil ik alle (oud-)collega's bedanken voor de gezelligheid: Geraldine Woestenenk, Tycho Sonnemans, Bob van Someren, Wilko Planje, Arnaud Kok, Tonnis Nuver, Marijn van Veghel, Erik van Ooijen, Dries van Oosten, Jeroen Bakker, Dmitrii Mazurenko, Otto Muskens, Lennart Karssen, Richard van der Stam en Carolijn van Ditzhuijzen. Ik wil vooral Erik en Dries succes wensen met de komende drukke tijd. Ook wil ik Wim Westerveld, Pedro Zeijlmans van Emmichoven, Henrik Rudolph, Cees-Jan den Adel, Bert Crielaard, Cees Andriesse, Herman Beijerinck, Henk Heideman en Cees de Kok bedanken voor de leuke gesprekken in de wandelgangen of tijdens borrels. Henk, erg bedankt voor het nauwkeurig lezen van een aantal hoofdstukken van mijn proefschrift.

Mijn familie en vrienden wil ik bedanken voor de getoonde interesse. Familie heb ik erg veel, vrienden niet zoveel, maar toch allen bedankt. Piet, bedankt voor het helpen met de omslag. Ik wil vooral mijn ouders erg bedanken voor de kansen, die ze me hebben geboden en voor het financieel mogelijk maken, dat ik verder kon studeren.

Mollie, heel erg bedankt, dat je me zo gesteund hebt toen mijn promotie erg slecht liep. Ik heb het je niet makkelijk gemaakt. Gelukkig ben je een vrolijk en opgewekt mens, ik kan daar nog veel van leren. Nu kunnen we samen genieten van de tijden, die komen gaan.